

A MULTI-SCALE APPROACH TO CHARACTERIZATION OF VOLCANIC
NATURAL POZZOLANS

A THESIS SUBMITTED TO
THE GRADUATE SCHOOL OF NATURAL AND APPLIED SCIENCES
OF
MIDDLE EAST TECHNICAL UNIVERSITY

BY

ALIREZA SASSANI

IN PARTIAL FULFILLMENT OF THE REQUIREMENTS
FOR
THE DEGREE OF MASTER OF SCIENCE
IN
CIVIL ENGINEERING

AUGUST 2014

Approval of the thesis:

**A MULTI-SCALE APPROACH TO CHARACTERIZATION OF
VOLCANIC NATURAL POZZOLANS**

submitted by **ALIREZA SASSANI** in partial fulfillment of the requirements for the degree of **Master of science in Civil Engineering Department, Middle East Technical University** by,

Prof. Dr. Canan Özgen _____
Dean, Graduate School of **Natural and Applied Sciences**

Prof. Dr. Ahmet Cevdet Yalçın _____
Head of Department, **Civil Engineering**

Assoc. Prof. Dr. Lutfullah Turanlı _____
Supervisor, **Civil Engineering Dept., METU**

Assist. Prof. Dr. Çağla Meral _____
Co-Supervisor, **Civil Engineering Dept., METU**

Examining Committee Members:

Prof. Dr. Hayrettin Yücel _____
Chemical Engineering Dept., METU

Assoc. Prof. Dr. Lutfullah Turanlı _____
Civil Engineering Dept., METU

Assoc. Prof. Dr. Sinan T. Erdoğan _____
Civil Engineering Dept., METU

Assit. Prof. Dr. Çağla Meral _____
Civil Engineering Dept., METU

Dr. Ayşegül Petek Gürsel _____
Civil and environmental Engineering Dept., UC Berkeley

Date: 06.08.2014

I hereby declare that all information in this document has been obtained and presented in accordance with academic rules and ethical conduct. I also declare that, as required by these rules and conduct, I have fully cited and referenced all material and results that are not original to this work.

Name, Last name: Alireza Sassani

Signature :

ABSTRACT

A MULTI-SCALE APPROACH TO CHARACTERIZATION OF VOLCANIC NATURAL POZZOLANS

Sassani, Alireza

MS., Department of Civil Engineering

Supervisor : Assoc. Prof. Dr. Lutfullah Turanli

Co-Supervisor: Assist. Prof. Dr. Cagla Meral

August 2014, 151 pages

Three types of volcanic rocks, namely perlite, a zeolite-rich volcanic tuff and a feldspar-rich volcanic tuff were selected to represent the general group of Volcanic Natural Pozzolans (VNPs). The target group was those volcanic natural pozzolans which intrinsically possess pozzolanic properties, i.e. do not require heat-treatment to obtain pozzolanic reactivity. X-ray Fluorescence (XRF), Powder X-Ray Diffraction (XRD), Blaine air permeability test, Laser diffraction, thermogravimetry (TGA), solid-state ^{29}Si nuclear magnetic resonance spectroscopy (NMR) and solid-state ^{27}Al NMR techniques were utilized to characterize the unhydrated powder of the selected pozzolans. For each of the three selected VNPs the engineering performance of the respective 50 (wt%) VNP-50 (wt%) PC based system were evaluated. Mortar samples were studied for strength development and expansion due to Alkali-Silica reaction (ASR); while paste samples were studied by Isothermal Calorimetry method in order to monitor the heat evolution during the hydration. Pastes were then studied by the use of XRD, ^{29}Si NMR, and ^{27}Al NMR techniques

so as to investigate the micro- and nano-structure of the hydration products of 50 (wt%)NP-50 (wt%)PC systems. The performance of the selected pozzolans with respect to pozzolanic activity and ASR expansion were almost similar; they all exhibited acceptable pozzolanic performance and ability to suppress ASR expansion. However, the pozzolans had different sources of pozzolanic reactivity, i.e. their pozzolanic property originate from different phases and/or is associated with different mechanisms. The C-S-H phases in the NP-blended pastes possessed longer silicate chains than the control samples. Aluminum incorporation into C-S-H structure was investigated and various Aluminum species were detected.

Keywords: Natural Pozzolan, Perlite, Zeolite, Feldspar, Volcanic Tuff.

ÖZ

VOLKANİK DOĞAL PUZOLANLARIN KARAKTERİZASYONU İÇİN ÇOK ÖLÇEKLİ BİR YAKLAŞIM

Sassani, Alireza

Yüksek Lisans, İnşaat Mühendisliği Bölümü

Tez Yöneticisi : Doç. Dr. Lutfullah Turanlı

Ortak Tez Yöneticisi: Yrd. Doç Dr. Çağla Meral

Ağustos 2014, 151 sayfa

Bu araştırmada, volkanik doğal puzolanları (VDP) temsil etmek için üç tip volkanik tuf seçilmiştir, bunlar perlit, zeolitçe zengin volkanik tuf ve feldispatça zengin volkanik tuf. Hedef grubta yer alan puzolanlar özünde puzolanik aktiviteye sahiptirler, bunların puzolanik aktivite göstermeleri için ısı işlem gerekmemektedir. X-ışını floresans (XRF), toz X-ışını difraksiyonu (XRD), seçilen puzolanların hidrate edilmemiş tozunu karakterize etmek için kullanılmıştır. Seçilen her üç puzolanın mühendislik performansları % 50(ağırlıkça) VDP- % 50 (ağırlıkça) PC tabanlı bir sistemle değerlendirildi. Dayanım gelişmeleri ve Alkali silika reaksiyon genleşmeleri için harç numuneler kullanılırken hamur numuneler izotermal kalorimetre ile hidrasyon sırasında ısı gelişimini izlemek için kullanılmıştır. Hamurların % 50 (ağırlıkça) VDP- % 50 (ağırlıkça) PC hidrasyon ürünlerinin üzerinde mikro ve nano-yapısı XRD, katı-hal ²⁹Si Magic Nükleer Manyetik Rezonans Spektroskopisi (²⁹Si MAS NMR), ve katı-hal ²⁷Al MAS NMR tekniklerini kullanarak incelenmiştir. Seçilen puzolanların puzolanik aktivitesi ve ASR genleşme

performansları hemen hemen benzerdir; hepsi kabul edilebilir puzolanik performans ve ASR genleşmesini azaltması için etkili bulunmuştur. Ancak, puzolanlar puzolanik reaktivitesi farklı kaynaklardan dolayıdır. NP-harmanlanmış hamurlarda CSH fazlar kontrol örneklerinden daha uzun silikat zincirlerine sahiptir. CSH yapı içine alüminyum ilişkisi incelenmiş ve çeşitli Alüminyum türler tespit edilmiştir.

Anahtar Kelimeler: Doğal Puzolan, Perlit, Zeolit, Feldispat, Volkanik tüf.

To my family...

To my Shadi...

ACKNOWLEDGMENTS

First, I would like to thank my adviser, Assoc. Prof. Dr. Lutfullah Turanli, for his support during my master studies and for his patience. I express my sincere gratitude to my co-adviser, Assist. Prof. Dr. Cagla Meral, for her motivation, enthusiasm, and immense knowledge as well as her extraordinary thoughtfulness and courtesy. This research would be a “*bootless inquisition*” without her guidance.

I sincerely thank Dr. Abdel Hamid Emwas for his significant contribution to this study and very kindly sharing his vast fund of physical chemistry knowledge with me. The NMR data were obtained by Dr. Emwas in King Abdullah University of Science and Technology (KAUST).

I would like to express my immense gratitude to Prof. Dr. Ismail Ozgur Yam, Assoc. Prof. Dr. Sinan T Erdogan and Prof. Dr. Mustafa Tokyay for their invaluable support, indispensable advises and exemplary humanity. They taught me the way of being a successful scholar, a good human and a happy person at the same time.

I thank my fellow lab mates, Burhan, Hasan, Meltem and Murat for all the support, friendship and assistance they gave me. I thank my dear friends Amir, Haani, Hatef, Mehran, Ali, Mohsen, Mohammad and Mahdi. They helped me make it through hard times.

This study was supported by The Scientific and Technological Research Council of Turkey (TUBITAK) Project No:113M911.

I would like to thank J.R.R. Tolkien, Isaac Asimov, Arthur C. Clarke, Mikhail Bulgakov, Eric Kripke, C.S. Lewis, J.K. Rowling and J.R.R. Martin for creating a world of fantasy to which I took refuge from time to time.

Last but most importantly I thank my family, my parents, my sister, my brothers and my lovely wife, with whom everyday life is my share of heaven.

TABLE OF CONTENTS

ABSTRACT.....	v
ÖZ.....	vii
AKNOWLEDGMENTS.....	x
TABLE OF CONTENTS.....	xi
LIST OF TABLES.....	xiv
LIST OF FIGURES.....	xv
LIST OF ABBREVIATIONS.....	xix

CHAPTERS

1 INTRODUCTION	1
1.1 General introduction.....	1
1.1.1 Significance.....	1
1.2 Thesis outline	3
1.2.1 Objective	3
1.2.2 Scope	4
1.3 Literature review	5
1.3.1 Natural pozzolans: definition, history and classification.....	5
1.4 Characterization of hydration products	9
1.4.1 Cement chemistry nomenclature.....	9
1.4.2 Paste structure	10
2 MATERIALS AND METHODS.....	13
2.1 Natural pozzolans and Portland cement	13
2.1.1 The origin and chemical composition of the materials	13
2.2 Physical properties of materials	17

2.3	Powder X-ray diffraction (XRD) analysis	19
2.3.1	Powder XRD analysis of anhydrous tuff-1	20
2.3.2	Powder XRD analysis of anhydrous perlite	32
2.3.3	Powder XRD analysis of tuff-2	38
2.3.4	Powder XRD analysis of white Portland cement (WPC)	42
2.4	Thermal analysis (TGA) of anhydrous materials	44
2.4.1	TGA analysis of tuff-1	44
2.4.2	TGA analysis of perlite	45
2.4.3	TGA analysis of tuff-2	47
2.4.4	TGA analysis of WPC	48
2.5	Nuclear magnetic resonance (NMR) spectroscopy	50
2.5.1	Considerations about solid-state NMR spectroscopy	50
2.5.2	²⁹ Si NMR spectroscopy of anhydrous tuff-1	57
2.5.3	²⁷ Al NMR spectroscopy of anhydrous tuff-1	59
2.5.4	²⁹ Si NMR spectroscopy of anhydrous perlite	62
2.5.5	²⁷ Al NMR spectroscopy of anhydrous perlite	65
2.5.6	²⁹ Si NMR spectroscopy of anhydrous tuff-2	68
2.5.7	²⁷ Al NMR spectroscopy of anhydrous tuff-2	71
2.5.8	²⁹ Si NMR spectroscopy of anhydrous WPC	74
2.5.9	²⁷ Al NMR spectroscopy of anhydrous WPC	78
2.6	Compressive strength performance tests	81
2.7	Effect of NPs on the expansion of mortar samples due to Alkali-Silica reaction (ASR).....	82
2.8	Heat evolution and setting time	83
2.8.1	Isothermal calorimetry	83
2.8.2	Setting time	85
3	RESULTS AND DISCUSSION	87

3.1	Strength performance	87
3.1.1	Strength activity index (SAI)	87
3.1.2	Compressive strengths of HVNP-PC mortars.....	88
3.2	Heat evolution and setting time	89
3.2.1	Normal consistency pastes.....	89
3.2.2	Pastes with water-to-binder ratio of 0.5.....	90
3.3	Alkali-silica reactivity	94
3.4	XRD analysis of hydrated WPC and hydrated pastes	95
3.4.1	HWPC.....	96
3.4.2	Htuff-1	98
3.4.3	Hperlite	100
3.4.4	Htuff-2	101
3.5	NMR spectroscopy of pastes	103
3.5.1	²⁹ Si NMR study of HWPC.....	103
3.5.2	²⁷ Al NMR study of HWPC	106
3.5.3	²⁹ Si NMR study of Htuff-1	109
3.5.4	²⁷ Al NMR study of Htuff-1.....	113
3.5.5	²⁹ Si NMR study of Hperlite	117
3.5.6	²⁷ Al NMR study of Hperlite.....	120
3.5.7	²⁹ Si NMR study of Htuff-2	123
3.5.8	²⁷ Al NMR study of Htuff-2.....	127
3.6	Quantitative analysis of NMR data.....	130
4	CONCLUSION.....	137
4.1	Concluding remarks	137
4.2	Recommendations for future work.....	140
	REFERENCES.....	147

LIST OF TABLES

TABLES

Table1.1. Activity types and their corresponding active substances in Mielenz & Greene (1951) classification.	7
Table1.2. Activity types of some common NPs in US according to Mielenz & Greene (1951)	8
Table1.3. Abbreviations of clinker oxide components in cement chemistry.	10
Table2.1. Oxide composition of WPC (C), perlite (P), tuff-1 (Z) and tuff-2 (F) presented as mass-percent and mol-percent.....	16
Table2.2. Blaine fineness and residue on 45 μ m sieve of the studied VNPs and WPC	18
Table2.3. The main features of particle size distribution obtained by means of laser diffraction technique.....	19
Table2.4. Principal characteristic peaks of Heulandite and Clinoptilolite compared with their correspondent peaks in the XRD pattern of tuff-1.	24
Table2.5. ²⁹ Si Chemical shift ranges for various silicate species (Young & Sun 1999b).....	53
Table 3.1. Strength activity indices of the NPs.	87
Table3.2. Initial and final setting times of normal consistency paste samples.....	90
Table3.3. Setting times and their equivalent heat of hydration values of pastes having water-to-binder ratio of 0.5.....	91
Table 3.4. Quantitative analysis results of ²⁹ Si NMR data.....	130
Table 3.5. Quantitative analysis results of ²⁷ Al NMR data.	131
Table 3.6. The percentage of various (alumino)silicate species in anhydrous and hydrated WPC-NP blends.	134
Table 3.7. The percentage of various Aluminum species in anhydrous and hydrated WPC-NP blends.	135

LIST OF FIGURES

FIGURES

Figure 2.1. The locations of Erzincan perlite, Isparta tuff and Balıkesir –Bigadiç tuff quarries.	14
Figure 2.2. Schematic presentation of the lithologic units in Balıkesir-Bigadic region.	15
Figure 2.3. Particle size distributions of VNPs and WPC obtained by laser diffraction technique.	18
Figure 2.4. Powder XRD pattern of tuff-1.	21
Figure 2.5. Simulated XRD patterns of Clinoptilolite-Na and Heulandite-Ca (“JCPDS PDF-2 Database,” 2004).	22
Figure 2.6. The XRD patterns of several Heulandite and Clinoptilolite minerals (“JCPDS PDF-2 Database,” 2004) compared with the obtained XRD pattern of tuff-1.	25
Figure 2.7. The XRD patterns of tuff-1 before and after heat treatment at 450°C. ...	27
Figure 2.8. Illustration of peak intensity reduction in the XRD patterns of tuff-1 before and after heat treatment.	30
Figure 2.9. SEM image of tuff-1 (Uzal, 2007).	30
Figure 2.10. Peaks assigned to quartz (Q) and Clay mineral (H) in the XRD pattern of the non-heat-treated tuff-1 sample.	31
Figure 2.11. Simulated XRD patterns of quartz and hydrated Halloysite compared with the XRD pattern of non-heat-treated tuff-1.	32
Figure 2.12. XRD pattern of Perlite powder.	33
Figure 2.13. Illustration of the peaks corresponding to Quartz (Q), Feldspar (F) and Mica (M) in the XRD pattern of perlite.	34
Figure 2.14. The XRD patterns of the perlite sample and candidate micas.	35

Figure2.15. Feldspar series classified on the basis of chemical composition.	
Ternary presentation of composition (Wenk H.-R., 2005).....	36
Figure2.16. The XRD patterns of perlite and candidate feldspars.....	37
Figure2.17.XRD pattern of tuff-2 sample.	40
Figure2.18.XRD pattern of tuff-2 and simulated XRD patterns of Anorthoclase, Quartz, Muscovite and the Calcium silicate mineral.	41
Figure2.19.Main peaks of the identified phases in the XRD pattern of tuff-2.....	42
Figure2.20. XRD pattern of WPC.....	43
Figure2.21. The TGA curve of tuff-1.....	45
Figure2.22. TGA curve of perlite.	47
Figure2.23. TGA curve of tuff-2.....	48
Figure2.24. TGA curve of WPC.....	50
Figure2.25.Chemical shift ranges of ²⁹ Si nucleus in various Q ⁴ silicate species (Lippmaa & Mägi 1981).....	52
Figure2.26. ²⁹ Si NMR spectra of tuff-1.....	57
Figure2.27. Deconvolution of peaks in ²⁹ Si NMR spectrogram of tuff-1 and the respective chemical shift (ppm) of the peaks.....	58
Figure2.28. ²⁷ Al NMR spectra of tuff-1.....	60
Figure2.29. Deconvolution of peaks in ²⁷ Al NMR spectrogram of tuff-1.	61
Figure2.30. Experimental vs. simulated ²⁷ Al NMR spectrogram of tuff-1.....	62
Figure2.31. ²⁹ Si NMR spectra of perlite.....	63
Figure2.32. Deconvolution of peaks in ²⁹ Si NMR spectrogram of perlite.....	64
Figure2.33. Experimental vs. simulated ²⁹ Si NMR spectrogram of perlite.....	65
Figure2.34. ²⁷ Al NMR spectra of perlite.....	66
Figure2.35. Deconvolution of peaks in ²⁷ Al NMR spectrogram of perlite.	67
Figure2.36. Experimental vs. simulated ²⁷ Al NMR spectrogram of perlite.	68
Figure 2.37. ²⁹ Si NMR spectra of tuff-2.....	69
Figure 2.38. Deconvolution of peaks in ²⁹ Si NMR spectrogram of tuff-2.....	70
Figure 2.39. Experimental vs. simulated ²⁹ Si NMR spectrogram of tuff-2.....	71
Figure 2.40. ²⁷ Al NMR spectra of tuff-2.	72
Figure 2.41. . Deconvolution of peaks in ²⁷ Al NMR spectrogram of tuff-2.	73
Figure 2.42. Experimental vs. simulated ²⁷ Al NMR spectrogram of tuff-2.....	74
Figure2.43. ²⁹ Si NMR spectra of anhydrous WPC.....	75

Figure2.44. Deconvolution of peaks in ^{29}Si NMR spectrogram of anhydrous WPC in range-1.....	76
Figure2.45. ^{29}Si NMR spectra of synthetic Belite (a) and Alite (b) (Brunet et al. 2010).....	77
Figure2.46. ^{27}Al NMR spectra of anhydrous WPC.	79
Figure2.47. The principal peaks in ^{27}Al NMR spectra of WPC.....	80
Figure2.48. Experimental vs. simulated ^{27}Al NMR spectrogram of anhydrous WPC	81
Figure2.49. a typical isothermal calorimetry diagram of ordinary Portland cement (Girao 2007).....	84
Figure3.1. The graphic presentation of the results of compressive strength tests. .	89
Figure3.2. Normalized heat flow-time curves of neat and blended pastes with water-to-binder ratio of 0.5 over a 3-day course.....	93
Figure3.3. The curves of normalized cumulative heat of hydration of the neat and blended pastes with water-to-binder ratio of 0.5 over a 10-day course.	94
Figure3.4. The graphic presentation of the results of ASR tests.	95
Figure3.5. The XRD patterns of HWPC and identified phases.....	97
Figure3.6. Main peaks of the identified phases in the XRD pattern of HWPC.	98
Figure3.7. Main peaks of the identified phases in the XRD pattern of Htuff-1...	100
Figure 3.8. Main peaks of the identified phases in the XRD pattern of Hperlite.	101
Figure 3.9. Main peaks of the identified phases in the XRD pattern of Htuff-2..	102
Figure3.10. ^{29}Si NMR spectra of hydrated WPC.	103
Figure3.11. The principal peaks in ^{29}Si NMR spectra of HWPC.....	105
Figure3.12.Experimental vs. simulated ^{29}Si NMR spectrogram of HWPC.....	105
Figure 3.13. Comparative presentation of ^{29}Si NMR spectra of HWPC, and anhydrous WPC	106
Figure3.14. ^{27}Al NMR spectra of hydrated WPC.....	107
Figure3.15. The principal peaks in ^{27}Al NMR spectra of HWPC.	108
Figure3.16. Experimental vs. simulated ^{27}Al NMR spectrogram of HWPC.	109
Figure3.17. ^{29}Si NMR spectra of Htuff-1.....	110
Figure3.18. The principal peaks in ^{29}Si NMR spectra of Htuff-1.	111
Figure3.19. Experimental vs. simulated ^{29}Si NMR spectrogram of Htuff-1.....	112
Figure 3.20. Comparative presentation of ^{29}Si NMR spectra of Htuff-1, anhydrous tuff-1 and anhydrous WPC.	113

Figure3.21. ^{27}Al NMR spectra of Htuff-1.	114
Figure3.22. The principal peaks in ^{27}Al NMR spectra of Htuff-1.	115
Figure3.23. Collective presentation of principal peaks in ^{27}Al NMR spectra of Htuff-1.	116
Figure3.24. Experimental vs. simulated ^{27}Al NMR spectrogram of Htuff-1.	116
Figure3.25. ^{29}Si NMR spectra of Hperlite.	117
Figure3.26. The principal peaks in ^{29}Si NMR spectra of Hperlite.	118
Figure3.27. Experimental vs. simulated ^{29}Si NMR spectrogram of Hperlite.	119
Figure3.28. Comparative presentation of ^{29}Si NMR spectra of Hperlite, anhydrous perlite and anhydrous WPC.	120
Figure 3.29. ^{27}Al NMR spectra of Hperlite.	121
Figure 3.30. The principal peaks in ^{27}Al NMR spectra of Hperlite.	122
Figure 3.31. Experimental vs. simulated ^{27}Al NMR spectrogram of Hperlite.	123
Figure 3.32. ^{29}Si NMR spectra of Htuff-2.	124
Figure 3.33. The principal peaks in ^{29}Si NMR spectra of Htuff-2.	125
Figure 3.34. Experimental vs. simulated ^{29}Si NMR spectrogram of Htuff-2.	126
Figure 3.35. Comparative presentation of ^{29}Si NMR spectra of Htuff-2, anhydrous tuff-2 and anhydrous WPC.	127
Figure 3.36. ^{27}Al NMR spectra of Htuff-2.	128
Figure 3.37. The principal peaks in ^{27}Al NMR spectra of Htuff-2.	129
Figure 3.38. Experimental vs. simulated ^{27}Al NMR spectrogram of Htuff-2.	129

LIST OF ABBREVIATIONS

ASR.....	alkali-silica reaction
Hperlite.....	hydrated perlite-WPC paste
Htuff-1.....	hydrated tuff-1-WPC paste
Htuff-2.....	hydrated tuff-2-WPC paste
HWPC.....	hydrated neat WPC paste
MCL.....	mean silicate chain length
NMR.....	nuclear magnetic resonance
NP.....	natural pozzolan
PC.....	portland cement
PSD.....	particle size distribution
SAI.....	strength activity index
SCM.....	supplementary cementing material
VNP.....	volcanic natural pozzolan
WPC.....	white portland cement
XRD.....	X-ray diffraction

CHAPTER 1

INTRODUCTION

1.1 General introduction

1.1.1 Significance

In May 2013, the daily mean concentration of CO₂ in the atmosphere surpassed 400 ppm. The CO₂ concentration in the atmosphere, having fluctuated between about 180 ppm and 280 ppm for the past 800,000 years, is now experiencing an increase rate about 100 times faster than the last dramatic increase period at the end of the last ice age (“ESRL, NOAA. ‘Earth System Research Laboratory.’ Trends in Atmospheric Carbon Dioxide [online]”). Therefore, industries are increasingly urged to shift to low-carbon technologies and processes in order to suppress the unprecedentedly high rate of CO₂ emission in the atmosphere.

Even though a typical concrete mix is composed of Portland cement (PC), water, aggregates, chemical admixtures and possibly supplementary cementitious materials (SCMs), the majority of PC concrete production-related CO₂ emissions is ascribed to production of PC. In addition, the production of Portland cement is currently responsible for about 7 % of the total anthropogenic CO₂ emission in the atmosphere. Although several energy efficiency policies have been adopted by manufacturers, or enforced by the authorities to reduce the environmental impacts of cement production; still for production of 1 ton of PC clinker, approximately 0.86 tons of CO₂ is emitted (World Business Council for Sustainable Development 2009). Approximately 60% of these emissions come from the calcination of limestone ($CaCO_3 \rightarrow CaO + CO_2$) (Gursel et al. 2013). The remaining 40% is mainly due to pyro-processing and grinding. The pyro-processing and grinding techniques have been improved considerably over the years; and more environmentally friendly alternatives have been adopted. However, calcination of limestone (the main raw

material of PC) is the most critical chemical reaction of the PC production; and produces a fixed amount of CO_2 . Therefore, adopting energy efficiency policies is not solely enough to convert the PC concrete industry into a sustainable industry.

Partial or complete replacement of PC by low-carbon alternative materials such as fly ash, slag or natural pozzolans contributes significantly to the reduction of the rate of global CO_2 emission induced by PC concrete production (K. Celik et al. 2014; Kemal Celik, Meral, and Mancio 2013; Erdem, Meral, Tokyay, and Erdoğan 2007). Replacement of a portion of cement in concrete with supplementary cementing materials (also called supplementary cementitious materials, both referred to as SCMs) is a reportedly feasible means to produce greener concrete and consequently reduce the CO_2 emission by concrete and construction industry (K. Celik et al. 2014). The effectiveness of this policy is assured by high-volume replacement of PC (PC replacement ≥ 50 wt%) by SCMs.

Natural pozzolans (NPs) provide a ubiquitous source of materials which can partially, or if properly activated, entirely replace PC. The ability of SCMs, including NPs, to replace PC roots in the so-called pozzolanic activity, that is the ability to react with Calcium hydroxide in presence of moisture and produce components which are stable in water and have binding properties (P. Mehta and Monteiro 2006). However, effective use of NPs, like any other SCMs, requires a comprehensive knowledge on the pozzolans' physical, chemical and mineralogical characteristics; while for any candidate NP the engineering performance of the respective NP-PC based systems should be evaluated.

SCMs comprise a wide variety of natural and artificial (or By-product) materials which can be used to partially or, in limited cases, entirely replace Portland cement in cement-based systems (Massazza F. 1993). The application of natural pozzolans as a supplementary cementing material dates back thousands of years to the age of Roman Empire or even earlier (Davidovits, Joseph 2005; ŠKVÁRA, Svoboda, and DOLEŽAL 2008). Nowadays, however, natural pozzolans do not appear to be as widely used as by-product SCMs such as fly ash, silica fume and blast furnace slag. This can be partly attributed to the less desirable properties of natural pozzolanic materials when compared to artificial pozzolans, particularly with respect to workability and pozzolanic reactivity. Nevertheless, it should be noted

that a considerable portion of problems associated with the application of natural pozzolans is related to the lack of knowledge about the nature of the cementitious systems containing natural pozzolans. This can potentially lead to incorrect use, inappropriate preparation procedures and dearth of efficient/effective application techniques (Bondar et al. 2011). The major problems are related to significant divergence of the properties of different NPs of different types and/or from different quarries such that the same type of NP from two different regions or quarries can possess considerably different characteristics and exhibit very different performances when used as SCMs. Hence, the applicability of natural pozzolans in practice, calls for comprehensive characterization of cementitious systems produced by the application of various natural pozzolans as well as the investigation of the behavior of natural pozzolan-containing cementitious systems.

1.2 Thesis outline

1.2.1 Objective

In this research the general objective was the characterization of three different volcanic NPs obtained from three different regions in Turkey. The target group in this study were the volcanic natural pozzolans which intrinsically possess pozzolanic properties, i.e. do not require heat treatment to gain pozzolanic reactivity. Considering the fact that Turkey is very rich in deposits of volcanic materials which can be used in cement and concrete industries, many researchers intend to study the applicability of these NPs as construction materials. Therefore, a need has arisen for comprehensive approaches to characterization of pozzolanic materials. A principal objective of the present research was to establish a multi-technique approach to characterization of SCMs that covers the properties of both the raw (anhydrous) materials and their respective NP-PC hydrated systems from macro-scale down to nano-scale. The methods, results and discussions of the presented research can be used by future scholars as a scientific basis for characterization of SCMs. It can be seen in this study that the application of each technique, particularly in nano-scale studies, can be facilitated if results of previous research on similar materials are available. Unfortunately in case of NPs which are found in Turkey, the number of comprehensive studies is very limited.

1.2.2 Scope

This study can be divided into three stages:

1. Processing and characterization of the anhydrous materials.

In this stage the NPs were received and processed so that they can be used as SCMs. The processing included crushing, drying and grinding. The prepared NPs as well as the PC were studied for determination of their physical and chemical properties. Then the mineralogy and molecular structure of the materials were investigated.

2. Preparation of mortar and paste samples. Investigation of strength and durability performance of mortars. Study of setting time and heat of hydration of paste samples.

This step of work was conducted in order to present the indexes showing the applicability and/or benefit of the selected NPs as SCMs. Although previous studies have proved the applicability of the selected materials, it was needed to obtain our own data to have a reliable understanding of the performance of materials. However, the principal aim of this stage was to obtain information about the practical performance of the materials that could be related to the structural information obtained in the first and third stages.

Once the anhydrous materials were characterized with respect to texture, chemical composition, mineralogy and molecular structure (stage one), they were used in cement-based mortar samples so that their effects could be investigated in terms of strength and durability. Neat PC mortars were made as control samples. Compressive strength and expansion due to Alkali-Silica reaction were used as indicators of strength and durability performances respectively.

Paste samples were made with blends of the selected NPs and PC, also neat PC pastes were made as controls samples. The setting times of paste samples were determined and the heat of hydration of pastes were monitored over a 10-day period.

3. Determination of the phases present in the paste samples with respect to crystallinity and/or molecular species.

All the techniques in this stage were performed on paste samples, both NP-PC and neat PC samples were studied and the results were thoroughly discussed and compared with the literature.

1.3 Literature review

1.3.1 Natural pozzolans: definition, history and classification

The word Pozzolan was originally used for pyroclastic glassy or zeolitized rocks found in the neighborhoods of Pozzuoli or Rome (both located in Italy) (Massazza F. 1993). This name was gradually generalized and used, in modern times, for a variety of materials with similar functionality in construction practices. In ACI 116R (*Cement and Concrete Terminology, ACI 116R-00* 1985) the definition for pozzolan is provided as:

A siliceous or siliceous and aluminous material, which in itself possesses little or no cementitious value but will, in finely divided form and in the presence of moisture, chemically react with calcium hydroxide at ordinary temperatures to form compounds possessing cementitious properties.

Natural pozzolan is defined to be “*either a raw or calcined natural material that has pozzolanic properties (for example, volcanic ash or pumicite, opaline chert and shales, tuffs, and some diatomaceous earths)*”. Other definitions are also provided for Pozzolan and Natural pozzolan, however, they all use the same concept of hardening through mixing with water in the presence of Calcium hydroxide. As in (Massazza F. 1993) pozzolan is defined, in a broad sense, as natural or artificial inorganic materials which show the ability of hardening in water upon being mixed with Calcium hydroxide (lime) or with materials that can release Calcium Hydroxide (such as Portland cement clinker).

The current archeological knowledge indicates that the application of pozzolans in construction dates back to at least 5000-4000 BC when a mixture of lime with diatomaceous earth from Persian gulf was used to produce cementitious binders (Malinowski, R., Garfinkel 1991). Lime, Limestone and gypsum are among the first construction materials used by humans. Mixtures of raw or heat-treated lime with locally available materials as fillers and/or aggregates were used as masonry binders in ancient civilizations (Mielenz, R. C., Greene K. T. 1951; *Use of Raw or Processed Natural Pozzolans in Concrete, ACI 232.1R-00* 2000). In ancient Egypt

calcined gypsum was used as cement. However in the Greek, Roman, and Persian empires raw or calcined Limestone was used either alone with water or mixed with aggregates (Barjasteh 2010; Mielenz, R. C., Greene K. T. 1951). Application of lime with various types of aggregates led the ancient masons to the discovery of pozzolans. As the masons observed that by the use of some materials such as ashes and volcanic tuffs as aggregates, the resulting concrete could harden under water, i.e. the binder was hydraulic, and a more durable and strong concrete was produced (Mielenz, R. C., Greene K. T. 1951). These experiences were the unmet need for the application of NPs. For example Sarooj, a binder used in ancient Iran, Yemen and Bahrain, consisted of lime (35%), sand (40%), ash (20%) and clay (5%) (Barjasteh 2010).

The classification of natural pozzolans is a complicated task because they often contain more than one reactive constituent (P. K. Mehta and Monteiro 2006). (Mielenz, R. C., Greene K. T. 1951) classified NPs on the basis of their active ingredients. In this approach the pozzolanic activity of NPs was attributed to the presence of one or more of five substances, namely 1) volcanic glass, 2) opal, 3) clay minerals, 4) zeolites and 5) hydrated oxides of Aluminum. Then six groups were defined as activity types (Table1.1). They classified the NPs commonly used in United States (at the time when the aforementioned paper was published) according to this approach (Table1.2).

Table 1.1. Activity types and their corresponding active substances in Mielenz & Greene (1951) classification.

Activity type	Active ingredient
1	Volcanic glass
2	Opal
3a	Kaolinite-type clays
3b	Montmorillonite-type clays
3c	Illite-type clays
3d	Mixed clays with altered Vermiculite
3e	Palygorskite
4	Zeolites
5	Hydrous Aluminum oxides
6	Nonpozzolans

Another classification was made in the published report by (P. K. Mehta and Monteiro 2006) on the basis of major reactive constituents which categorized natural pozzolans into four groups namely “volcanic glasses”, “volcanic tuffs”, “calcined clays and shales” and “diatomaceous earths”. This grouping was used in the present research as the reference classification.

All the above mentioned groups, except diatomaceous earths, originate from volcanic rocks (P. K. Mehta and Monteiro 2006). However, clays and shales do not possess pozzolanic properties without being calcined (i.e. heat treated). In this research the focus was on the volcanic pozzolans which intrinsically possess pozzolanic properties, i.e. do not need calcination to exhibit pozzolanic activity, this criterion excludes diatomaceous earths and the “calcined clays and shales” from the target group.

Table 1.2. Activity types of some common NPs in US according to Mielenz & Greene (1951)

Natural pozzolan	Activity type (refer to Table 1)
Rhyolite pumicites and tuffs	1
Cacite pumicites and tuffs	
Altered pumicites and tuffs	1, 3a*
	1, 3b
Diatomite and diatomaceous earth	2
Opaline chert	
Opaline shales	2, 3b
Kaolin clays	3a
Bentonitic clays and shales	3b
Fuller's earth	
Hydromica (illite), clays and shales	3c
Glacial clays and silts	3d
Attapulugus clay	3e
Zeolitic tuffs and ashes	4
Bauxite	5
* Mixed activity type	

The major constituents of natural pozzolans are silica minerals which include a wide variety of polymorphs with the overall composition of SiO_2 . Most Silica minerals contain Silicon in tetrahedral SiO_4^{4-} units in which a Silicon atom is surrounded by four Oxygen atoms forming the corners of the tetrahedron (Wenk H.-R. 2005). Volcanic glasses and volcanic tuffs also contain various silica minerals.

Volcanic glasses are generated by the quick cooling of magma which contained (alumino)silicates as their principal constituent. It is noteworthy to mention that in the word “*(alumino)silicate*” the placement of “alumino” in parentheses is because the incorporation of Aluminum into the silicate structure (framework) may occur in different degrees varying from no Aluminum incorporation to saturation of the silicate framework with Aluminum. Volcanic glasses, represented in this study by Perlite, present pozzolanic reactivity as a result of containing aluminosilicates in a disordered structure; furthermore, their reactivity is enhanced by the porous texture and high surface area (P. K. Mehta and Monteiro 2006). The structure of Perlite is made up of 3-D networks of silicate and aluminosilicate (consisting of Al-O-Si bonds) tetrahedra; this architecture is close to artificial glass (Keller, w.D., Pickett 1954). Volcanic tuffs, represented in this research by zeolite-rich and feldspar-rich tuffs (tuff-1 and tuff-2 respectively) are defined generally as consolidated volcanic ash.

Volcanic tuffs are usually rich in tectosilicate minerals, particularly zeolites and feldspars, which are generated as a result of alteration of volcanic glass under hydrothermal conditions (P. K. Mehta and Monteiro 2006). zeolite minerals, are hydrous tectosilicates (framework silicates) (Wenk H.-R. 2005) with general formula $(\text{Na}_2 \text{Ca})\text{O} \cdot \text{Al}_2\text{O}_3 \cdot 4\text{SiO}_2 \cdot x\text{H}_2\text{O}$ (P. K. Mehta and Monteiro 2006). Feldspars, being the most abundant mineral group in the earth's crust, are anhydrous tectosilicates with general formula $\text{XAl}(\text{Si}, \text{Al})\text{Si}_2\text{O}_8$ with $\text{X} = \text{K}, \text{Na}, \text{Ca}, \text{Ba}, \text{Sr}$; almost all metamorphic and igneous rocks contain feldspar minerals (Wenk H.-R. 2005).

1.4 Characterization of hydration products

1.4.1 Cement chemistry nomenclature

Prior to section 1.5.2 the notations used in cement chemistry for the oxide components present in cement clinker should be explained. The abbreviations commonly applied in the cement chemistry are given in Table 1.3. Examples of the application of these abbreviations are C_3S and C_2S and CH which refer to $3\text{CaO} \cdot \text{SiO}_2$ (or Ca_3SiO_5), $2\text{CaO} \cdot \text{SiO}_2$ (or Ca_2SiO_4) and $\text{Ca}(\text{OH})_2$ respectively. The impure forms of C_3S and C_2S are called Alite and Belite, respectively.

Table 1.3. Abbreviations of clinker oxide components in cement chemistry.

Oxide component	Abbreviation	Oxide component	Abbreviation
CaO	C	SO ₃	\bar{S}
SiO₂	S	Na ₂ O	N
Al₂O₃	A	TiO ₂	T
Fe₂O₃	F	P ₂ O ₅	P
MgO	M	H ₂ O	H
K	K	CO ₂	\bar{C}

1.4.2 Paste structure

The long term behavior of cement-based systems depends mainly on the paste microstructure and its internal chemistry which are, in turn, governed by the nanostructure of the hydration products (Beaudoin, Raki, and Alizadeh 2009; Brunet et al. 2010). In present, despite the ubiquitous application of cement-based materials, there is a lack of knowledge about the nature of the hydration products of these materials (Rejmak and Dolado 2012). Calcium Silicate Hydrates (C-S-H) are the main part of the hydration products of cement-based materials. The C-S-H is the main binding phase in Portland cement matrix and is responsible for the largest portion of its properties, it constitutes up to 70% in weight of hardened ordinary cement pastes. (Battocchio, Monteiro, and Wenk 2012; Beaudoin, Raki, and Alizadeh 2009; Hewlett 2004; P. K. Mehta and Monteiro 2006; I.G. Richardson 2004, 2008; I. Richardson 1999; H. F. W. Taylor 1997). The structure of C-S-H and other phases in the hydration products vary depending on many factors such as age

(Battocchio, Monteiro, and Wenk 2012), Curing Temperature(a. V. Girao et al. 2007; Girão et al. 2007, 2010), SCMs (Beaudoin, Raki, and Alizadeh 2009; Brough et al. 1994; Brunet et al. 2010; Girão et al. 2010; Justnes and Meland 1990; Lothenbach, Scrivener, and Hooton 2011; Love, Richardson, and Brough 2007; I.G. Richardson 2004; J. F. Young 1988), presence of additive materials and chemical environment of hydration (Andersen, Jakobsen, and Skibsted 2004; Beaudoin, Raki, and Alizadeh 2009; Brunet et al. 2010; Jennings 2000; Justnes and Meland 1990; Raki et al. 2010; R. Taylor, Richardson, and Brydson 2010). The C-S-H structure being nearly amorphous, extremely variable and poorly ordered (I.G. Richardson 2008), has been eluding exact determination even in the case of ordinary Portland cement.

It has been widely accepted, that the C-S-H phase possesses a disordered layered structure made of a “Drierkette” form-like arrangement of silicate chains. A structure made up of various arrangements and sequences of silicate chains is analogous to that of Tobermorite or Jennite (two naturally occurring crystalline calcium silicate hydrates), other silicate-containing crystalline forms such as Jaffeite, or a combination of the structure of crystalline silicates with other substances such as $\text{Ca}(\text{OH})_2$ solid solution (Beaudoin, Raki, and Alizadeh 2009; I.G. Richardson 2004; I. Richardson 1999; H. F. W. Taylor 1997; H. H. F. W. Taylor 1986; H. Taylor 1993).

However, the C-S-H formed by hydration of Portland cement-based materials is significantly different from these crystal structures, basically in Ca/Si ratio and the length of silicate chains (Battocchio, Monteiro, and Wenk 2012; Maeshima et al. 2003). The differences in Ca/Si ratio and silicate anion structure are generally justified in the models through the assumption of a variety of defect chain structures (finite short silicate chains) and various arrangements of Calcium in the interlayer. The neutrality of the structure is mainly achieved through assumption of incorporation of ions such as Al^{3+} and OH^- into the C-S-H structure (Andersen, Jakobsen, and Skibsted 2003; Chen et al. 2004; Nonat 2004). Consequently, various existing models differ in explaining silicate anion structure, chemical composition (e.g. Ca/Si ratio), morphology, structural order, incorporating ions and their location, etc. For instance, despite degrees of consensus between the proposed or assumed structures of C-S-H in (Andersen, Jakobsen, and Skibsted 2004; Jennings 2000;

Pellenq et al. 2009; I.G. Richardson 2004, 2008; H. Taylor 1986; J. F. Young 1988), a considerable difference still prevails.

The structure of C-S-H and other product phases generated through the hydration of artificial/byproduct SCMs have been the subject of numerous studies. Extensive research has been conducted on fly ash (Brunet et al. 2010; Girão et al. 2007, 2010; Lu and Young 1993; Mohan et al. 1985), blast furnace slag (Lu and Young 1993; Mohan et al. 1985; I. Richardson 1999; Ian G Richardson et al. 1993; Le Saoût et al. 2011; R. Taylor, Richardson, and Brydson 2010) and silica fume (Demir and Serhat Baspinar 2008; Grutzeck, Benesi, and Fanning 1989; Justnes and Meland 1990). Despite the abundance of Natural Pozzolans (Saglik and Erdogan 2010), and the long time they have been used (Massazza F. 1993), the micro- and nano-structure of natural pozzolan-containing cementitious systems have not received as attention as by-product SCMs, the exceptions being calcined clay minerals : Kaolinite, Illite and Montmorillonite (Fernandez, Martirena, and Scrivener 2011) and KOH-activated Metakaolin (Love, Richardson, and Brough 2007). Only limited microstructural studies by XRD and SEM have been performed (Demir and Serhat Baspinar 2008; Erdem, Meral, Tokyay, and Erdogan 2007; Liebig and Althaus 1998; B. Uzal et al. 2010).

In the foregoing sections a brief introduction to the subject was provided and the previous works were reviewed. However, it would be more useful if the results of the preceding researches were mentioned in the analysis of the test results, so that their contribution to this present work is demonstrated more clearly. Thus, throughout the text, the discussions will be provided by referring to the existing literature.

CHAPTER 2

MATERIALS AND METHODS

2.1 Natural pozzolans and Portland cement

2.1.1 The origin and chemical composition of the materials

In order to thoroughly represent volcanic natural pozzolans (VNPs) found in Turkey, three pozzolans were chosen from three different regions. Perlite rock from quarry in Erzincan province was chosen to represent volcanic-glass-based natural pozzolans. Perlite is found in gray, black, light green and brown colors; the Perlite used in this research was in light gray color. Zeolite-rich tuff was yellowish and the feldspar-rich tuff was greenish-gray in color. Volcanic tuff from quarry in Balıkesir-Bigadic region and volcanic tuff from quarry in Isparta region were chosen to represent tuff-based natural pozzolans; hereinafter we refer to these two tuffs as *tuff-1* and *tuff-2* respectively and Perlite rock from Erzincan province will be simply called *perlite*. Perlite and tuff-1 were received in the form of crushed stone and subsequently ground in the ball mill in order to conform to the specifications of ASTM C 618 standard for physical requirements; Measurements were done according to ASTM C 311 standard. Tuff-2 was received from Göлтаş Cement Production Company in the form of fine powder (77% passing 45 μm sieve) which conformed to physical requirements mentioned in ASTM C 618 standard.

Figure 2.1 shows the regions from which the three VNPs were taken. Information about the geological properties of the quarries from which perlite and tuff-2 were taken was not available. However, the deposits of Perlite rock in Erzincan region have been extensively used in Turkey for industrial purposes and numerous researchers such as (Erdem, Meral, Tokyay, and Erdoğan 2007; Eser

2014; Saglik and Erdogan 2010) have utilized Erzincan Perlite in their researches and the tuff deposits in Isparta region have been (and are being) used to produce pozzolans in industrial scale. Balıkesir-Bigadiç region is known for its Boron deposits, while the geological studies have indicated the presence of two tuff units in the lithostratigraphic framework of the region. The lithologic units in the Balıkesir-Bigadiç region (Figure 2.2.) can be presented in ascending order (from bottom to top) as the following: 1) basement rocks, 2) basement volcanics unit, 3) basement limestone unit, 4) lower tuff unit, 5) lower borate bearing unit, 6) upper tuff unit, 7) upper borate bearing unit, 8) basalt, 9) recent sediments and alluvium. The Thickness of the upper tuff unit is about 300-350 m (Helvacı and Alaca 1991).



Figure 2.1. The locations of Erzincan perlite, Isparta tuff and Balıkesir –Bigadiç tuff quarries.

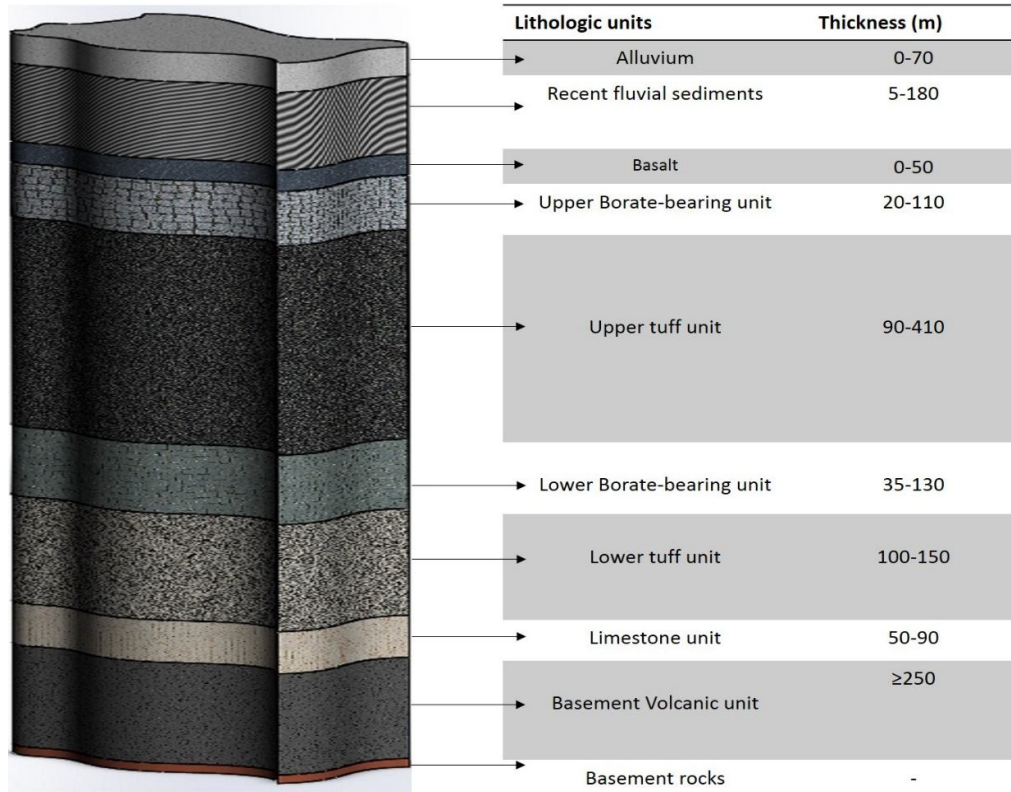


Figure 2.2. Schematic presentation of the lithologic units in Balıkesir-Bigadic region.

In all experiments, except in strength activity index test, white Portland cement (WPC) was used to be blended with the selected VNPs. Super white 52.5/85 Portland cement (TS 21 BPC 52.5 R) was received from *Çimsa cement group*. WPC was used to avoid the potential problems associated with the application of ordinary Portland cement in NMR and XRD techniques. High concentrations of Iron (including Ferrous and ferric compounds) in the cement pastes affect the magnetic field in NMR studies and can lead to inaccuracies in the results. In addition, Fe^{3+} ions cause intensity loss and line broadening (low resolution) of NMR spectra through $^{27}Al-Fe^{3+}$ unpaired electron dipolar coupling. OPC can cause difficulties also in XRD analyses. When Cu.K α radiation is used to obtain the XRD patterns,

the fluorescence radiation by Iron atoms interferes with the peaks from the crystal lattice and submerges low-intensity peaks by increasing the background; this is particularly the case with cement hydration products. Therefore the use of White Portland Cement which contains very small quantities of Iron (compared with OPC) is necessary to maintain the precision of the experiments.

Table 2.1. Oxide composition of WPC (C), perlite (P), tuff-1 (Z) and tuff-2 (F) presented as mass-percent and mol-percent.

	Oxide Composition							
	(Mass %)				(mol %)			
	C	P	Z	F	C	P	Z	F
SiO₂	16.20	71.2	68.40	45.50	15.45	77.85	71.80	48.48
Al₂O₃	03.89	14.00	13.30	14.30	2.18	9.02	8.23	8.98
CaO	60.80	01.22	02.48	14.70	62.12	1.42	2.80	16.78
Fe₂O₃	00.20	01.65	01.44	03.26	0.07	0.68	0.57	1.30
Na₂O	00.22	04.13	00.26	03.48	0.21	4.38	0.23	3.59
K₂O	00.31	04.99	04.19	04.87	0.19	3.48	2.80	3.31
MgO	00.75	00.30	00.85	01.24	1.07	0.49	1.34	1.97
SO₃	04.09	00.00 ¹	00.01	01.02	2.93	00.00 ³	0.01	0.81
CO₂	09.90	N.O. ²	06.89	08.19	12.89	N.O.	9.87	11.91
TiO₂	00.14	00.04	00.08	00.34	0.10	00.04	0.06	0.28
B₂O₃	03.24	01.99	01.72	02.15	2.67	1.88	1.56	1.98
MnO	N.O.	00.06	00.02	00.09	N.O.	0.06	0.02	0.09

¹ The actual value with four digits precision was 00.0074.

² Not observed in the spectra obtained in the XRF analysis of this material.

³ The actual value with three digits precision was 00.006.

Perlite, tuff-1, tuff-2 and WPC were analyzed by means of X-ray fluorescence (XRF) technique to determine the major oxide compounds present in the materials. The XRF results are presented in Table 2.1.

It should be mentioned that the XRF, XRD, Laser diffraction and TGA techniques were performed in the central laboratory of Middle East Technical University of Turkey and the NMR technique was conducted in King Abdullah University of the Saudi Arabia.

2.2 Physical properties of materials

As mentioned in section 2.1.1, perlite and tuff-1 were received in the form of crushed rock and then ground in a ball mill so that a fine powder was obtained; whereas, tuff-1 was received as fine powder of commercially available natural pozzolan. The properties which are related to the size and shape of the material's particles exert a significant effect on the cementing performance of any cementitious material. These properties are reflected in parameters such as specific surface area, particle size distribution and the percentage of the particles passing a particular size-sieve. The specific surface area of pozzolan powders and WPC were investigated by Blaine air permeability test according to ASTM C204-11 standard. Also the amount of a cementitious material, presented as mass percentage, retaining on the 45 μm sieve is considered as a measure of the fineness. The material residue on 45 μm sieve was measured according to ASTM C430 standard for WPC and each VNP. The residue on 45 μm sieve was used as an indication of the sufficiency of grinding. The specific gravity of the materials, the results of Blaine air permeability test and residue of materials on 45 μm sieve are presented in Table 2.2. The particle size distribution (PSD) of WPC and the selected VNPs were determined by laser diffraction method. A standard practice for laser diffraction analysis is not currently available, in this research 10 grams of powder were used in laser diffraction and the powder was dispersed in ethanol in an ultrasonic bath prior to the experiment. . The particle size distribution was measured in a MALVERN Nano ZS90 high performance two angle "*particle and molecular size analyzer*" instrument.

Table 2.2. Blaine fineness and residue on 45 μm sieve of the studied VNPs and WPC

Material	Specific gravity (g/cm ³)	Blaine fineness (specific surface area) (Cm ² /g)	Residue on 45 μm sieve (%mass)
WPC	3.06	4459	26.7
Perlite	2.38	4880	13.5
Tuff-1	2.19	10400	23.0
Tuff-2	2.53	4750	27.9

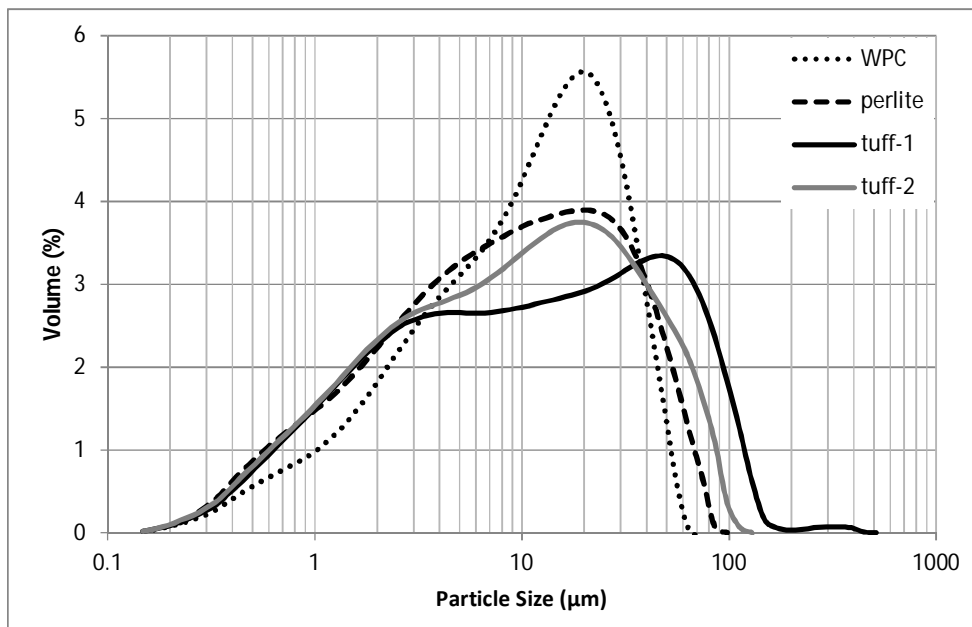


Figure 2.3. Particle size distributions of VNPs and WPC obtained by laser diffraction technique.

Figure 2.3 and Table 2.3 present the results of laser diffraction analysis for the studied materials. As seen in Table 2.3, tuff-1 exhibited significantly high specific surface area (i.e. Blaine fineness) while its residue on 45 μm sieve is comparable to other two VNPs and its average particle size is larger than the other three samples. The specific gravity of tuff-1, that is lower than the other three samples, and the results of the aforementioned techniques indicate the porous nature of tuff-1.

Table 2.3. The main features of particle size distribution obtained by means of laser diffraction technique.

Material	d(0.1)* (μm)	d(0.5)** (μm)	d(0.9)*** (μm)	Average particle size (μm)
WPC	1.608	10.883	31.960	14.148
Perlite	1.134	8.645	37.774	14.66
Tuff-1	1.178	11.063	67.283	24.549
Tuff-2	1.135	9.453	46.315	17.204

* 10% (volume %) of particles are smaller than d(0.1).

** 50% (volume %) of particles are smaller than d(0.5), this value is the median particle size.

*** 90% (volume %) of particles are smaller than d(0.9)

2.3 Powder X-ray diffraction (XRD) analysis

The XRD patterns were acquired on a Rigaku Ultima-IV X-ray powder diffractometer using Cu-K α radiation. XRD was performed in a slow pace (0.5 degrees/sec) in order to attain an acceptable XRD pattern resolution. Powder XRD analyses on anhydrous materials, i.e. VNPs and WPC in unhydrated (anhydrous) form, were performed on the powder materials explained in section 2.2.

Hydrated pastes studied in this research were made by mixing VNP, WPC and water. Also control pastes were prepared which contained only WPC and water. For each VNP, first 100g of a 1:1 blend of VNP and WPC with water-to-binder ratio of 0.5 was made in a glass beaker and thoroughly mixed so that a uniform blend was obtained. By a 1:1 blend we mean a mixture of two solid materials such that each of the two solids constitutes 50% of the weight of the mixture. Once the blend was made, it was added to 50 grams of distilled water in a separate glass beaker and hand-mixed for approximately three minutes by means of a one mm-diameter glass stick. The control pastes were made by the same procedure using 100g of WPC as the only binder material.

Once the pastes were prepared, they were cast in 15 ml plastic tubes. Then the lids of the tubes were closed, sealed by silicon sealant paste and kept in room temperature (~20-23°C) for seven months. The hardened pastes were then dimolded and ground in a desktop electric mortar grinder to obtain a fine powder with maximum particle size of approximately 50 µm. The obtained powders were used in XRD studies. The XRD analyses of the pastes will be discussed in chapter 3, where the neat WPC paste will be referred to as *HWPC* and the blended pastes will be referred to as *Htuff-1*, *Htuff-2* and *Hperlite*.

2.3.1 Powder XRD analysis of anhydrous tuff-1

Zeolites in alkaline igneous rocks, where they form euhedral crystals, can be easily identified. However, in order to identify zeolites in tuffs, which occur as fine-grained aggregates, methods such as x-ray based characterization techniques are required (Wenk H.-R., 2005). Therefore in order to identify the mineral components in tuff-1, powder X-ray diffraction technique (XRD) was utilized. Figure 2.4 shows the powder XRD pattern for tuff-1, i.e. the Intensity-2θ diffractogram of tuff-1 powder.

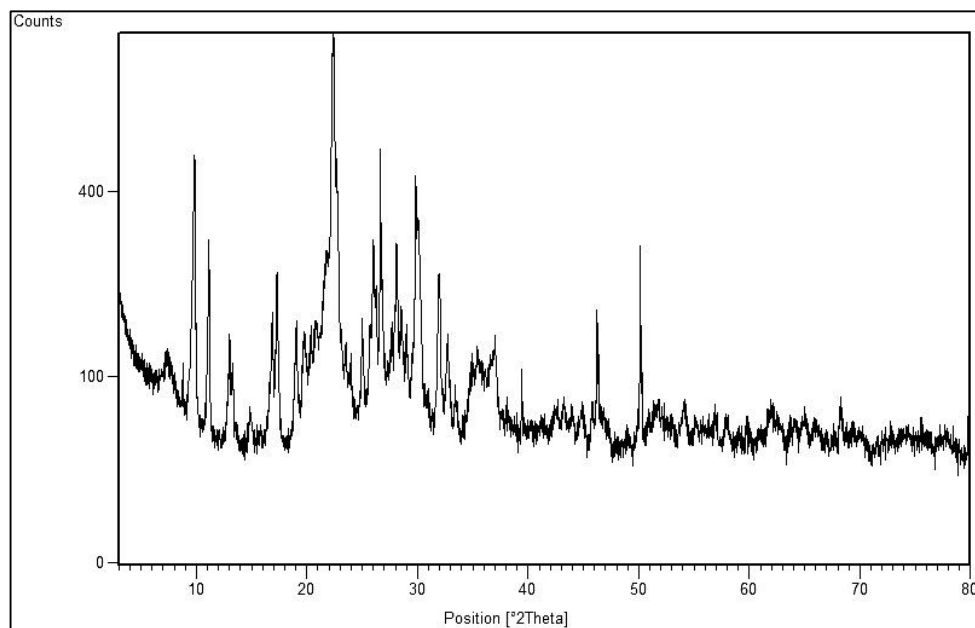


Figure 2.4. Powder XRD pattern of tuff-1.

The similarity of the crystal structures of two monoclinic zeolite minerals, Clinoptilolite and Heulandite, is a potential source of problem in XRD analysis of the substances which contain one or both of these minerals. Heulandite and Clinoptilolite are categorized together as Heulandite-type zeolites shown by HEU code (Martinezramirez et al. 2006; Treacy 2001), in fact these two minerals are considered as the end members which constitute the two opposite ends of the Heulandite group. Heulandites are the group of zeolites (framework aluminosilicates) that form a continuous solid solution with a Si/Al ratio between 3 and 5, having Heulandite (general formula $[(\text{Na}, \text{K}) \text{Ca}_4(\text{Al}_9\text{Si}_{27}\text{O}_{72}) \cdot 24\text{H}_2\text{O}]$) and Clinoptilolite (general formula $[(\text{Na}, \text{K})_6\text{Al}_6(\text{Si}_{30}\text{O}_{72}) \cdot 20\text{H}_2\text{O}]$) in two opposite ends (Martinezramirez et al. 2006). Clinoptilolite and Heulandite are isomorphous natural zeolites, thus their Aluminum-silicon framework structures are considered to be the same. However it is assumed that the idealized unit cells of Clinoptilolite and Heulandite have different chemical compositions, the major difference being in Si-substituting atoms in the central tetrahedral framework sites (Bish D.L. 2001; Ming and Dixon 1986). This similarity results in similar XRD patterns for both minerals, making it a complicated task to identify and/or differentiate Clinoptilolite and

Heulandite by means of XRD. The simulated XRD patterns for two Clinoptilolite and Heulandite minerals (Clinoptilolite-Na and Heulandite-Ca) are shown in Figure 2.5 (“JCPDS PDF-2 Database” 2004), the coincidence of peaks in the XRD patterns of Clinoptilolite and Heulandite is clearly seen in the figure.

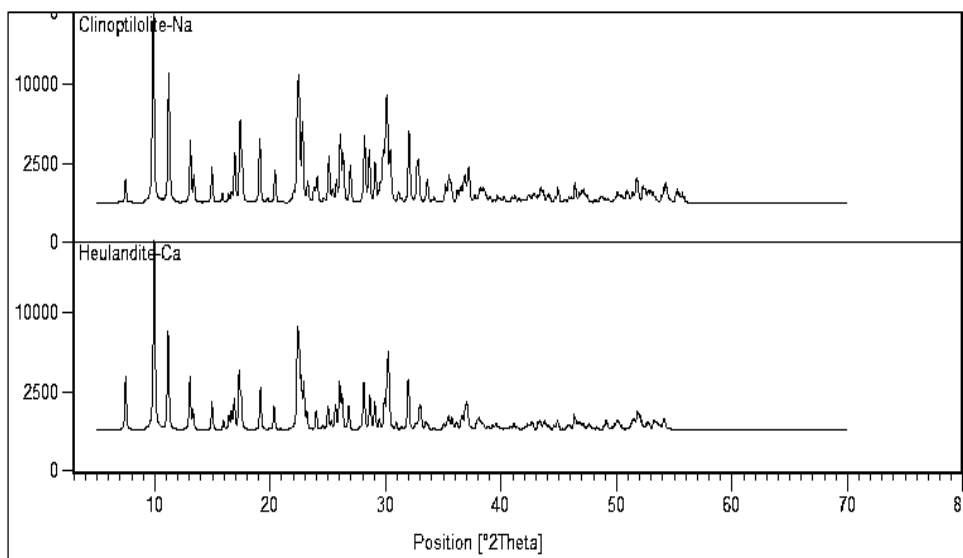


Figure 2.5. Simulated XRD patterns of Clinoptilolite-Na and Heulandite-Ca (“JCPDS PDF-2 Database,” 2004)

The difference between the unit cell parameters of the two minerals, Heulandite and Clinoptilolite, is not an effectively helping means to distinguish between the two minerals, because the unit cell parameters of Heulandite and Clinoptilolite are very sensitively dependent on the water content, and the extra-framework cation composition resulting in the variation of unit cell (Bish D.L. 2001;

Godelitsas and Armbruster 2003). As a result of the similarity between XRD patterns of Clinoptilolite and Heulandite, Clinoptilolite was not recognized as a distinct mineral until 1932, rather, it was assumed to be a silica-rich Heulandite (Bish D.L. 2001).

Some researchers such as (Perraki and Orfanoudaki 2004) have discussed the differences between the XRD patterns of end members of Heulandite group. (Perraki and Orfanoudaki 2004) attributed the highest peak in the XRD spectra of Heulandite to reflections from (020) planes with d-spacing equal to 8.99 Å ($d=8.99$). While the highest peak in Clinoptilolite XRD spectra, according to him, was assumed to correspond to the (004) reflection with $d=3.98\text{Å}$. On this basis, using the XRD pattern of a Heulandite-type zeolite in which the highest peak was observed at $2\theta=22.28$ degrees, (Perraki and Orfanoudaki 2004) concluded that the major phase in the studied material was Clinoptilolite. In contrast, numerous researches and the powder diffraction pattern databases, such as (“JCPDS PDF-2 Database” 2004; Noh 1998; Treacy 2001), have reported the observation of the highest peak at around $d=8.99$ for both Clinoptilolite and Heulandite. For example in (Treacy 2001) the highest peaks were observed at $2\theta=9.85$ for Heulandite and around $2\theta=9.88$ for Clinoptilolite which correspond to d-spacing of 8.98 Å and 8.95 Å respectively. In addition, there are numerous research cases in which the highest peak in the XRD pattern of Heulandite was observed to occur at or in the vicinity of 20-22.40 degrees (“JCPDS PDF-2 Database” 2004). Therefore, it is clearly seen that one cannot simply assign an XRD pattern to just one of Clinoptilolite and Heulandite minerals.

The principal peaks used for identification of Clinoptilolite and Heulandite are presented in Table 2.4 according to (Treacy 2001) and compared with the peaks observed in the XRD pattern of tuff-1. Figure 2.6 compares the XRD pattern of tuff-1 studied here in comparison with the simulated XRD patterns of a number of Heulandite-type minerals which most closely conformed to the obtained pattern. The patterns were simulated from the powder diffraction data provided in (“JCPDS PDF-2 Database” 2004). As it is seen in the Table 2.4 and Figure 2.6, the XRD pattern obtained for tuff-1 shows the characteristics of both Heulandite and Clinoptilolite. In the following, the principal peaks in the obtained XRD pattern (shown in Table 2.4) are discussed in detail.

Table 2.4. Principal characteristic peaks of Heulandite and Clinoptilolite compared with their correspondent peaks in the XRD pattern of tuff-1.

Peak features				
Mineral/material	2 θ	d-spacing	Relative intensity (%)	Reflecting plane
Heulandite	9.85	8.97	100	020
	11.07	7.98	64	200
	22.21	4	60.2	131
	22.34	3.97	53.8	330
Clinoptilolite	9.88	8.95	100	020
	11.19	7.91	40	200
	22.36	3.97	49.2	131
	22.49	3.95	37.2	330
Tuff-1	9.85	8.97	53.01	N.A.*
	11.14	7.94	29.53	N.A.
	22.4	3.97	100	N.A.
	22.71	3.91	53.2	N.A.

*Not Assigned

There is a small peak with relative intensity (I_{rel}) of 5.7 at $2\theta=7.41^\circ$, it corresponds to d-spacing of 11.93 Å. This peak most precisely conforms to Heulandite pattern with respect to 2θ position (as well as d-spacing), however, the intensity being higher than that normally observed in Heulandite XRD patterns indicates the possibility of a contribution to the intensity by reflections from Clinoptilolite lattices which may occur in the 2θ values close to 7.46° . The peak at $2\theta=9.85^\circ$ conforms to Heulandite pattern with respect to both position and intensity. Nevertheless, the occurrence of a peak at 9.88 in the XRD patterns of Clinoptilolite makes it difficult to certainly assign this peak to Heulandite. There is a peak with $I_{rel}=29.53$ at $2\theta=11.14^\circ$ (d-spacing=7.94Å) which lies in between the usually observed values for Heulandite and Clinoptilolite minerals (ref. table 2.4), while the intensity of the peak is less than both minerals. The highest peak in the XRD pattern

of tuff-1 ($I_{rel}=100$) is located at $2\theta=22.40^\circ$. Regarding the d-spacing (3.97\AA), this peak can be attributed to both Heulandite and Clinoptilolite; this becomes more critical considering the broadness of the peak which might be an indication of the presence of overlapping peaks. In case Heulandite and Clinoptilolite are both present in tuff-1 in stand-alone form, and considering that they both create peaks in the 22degrees to 23 degrees range, the overlapping peaks may belong to both Heulandite and Clinoptilolite. The same problem is also faced in assigning the peak located at $2\theta=22.71^\circ$.

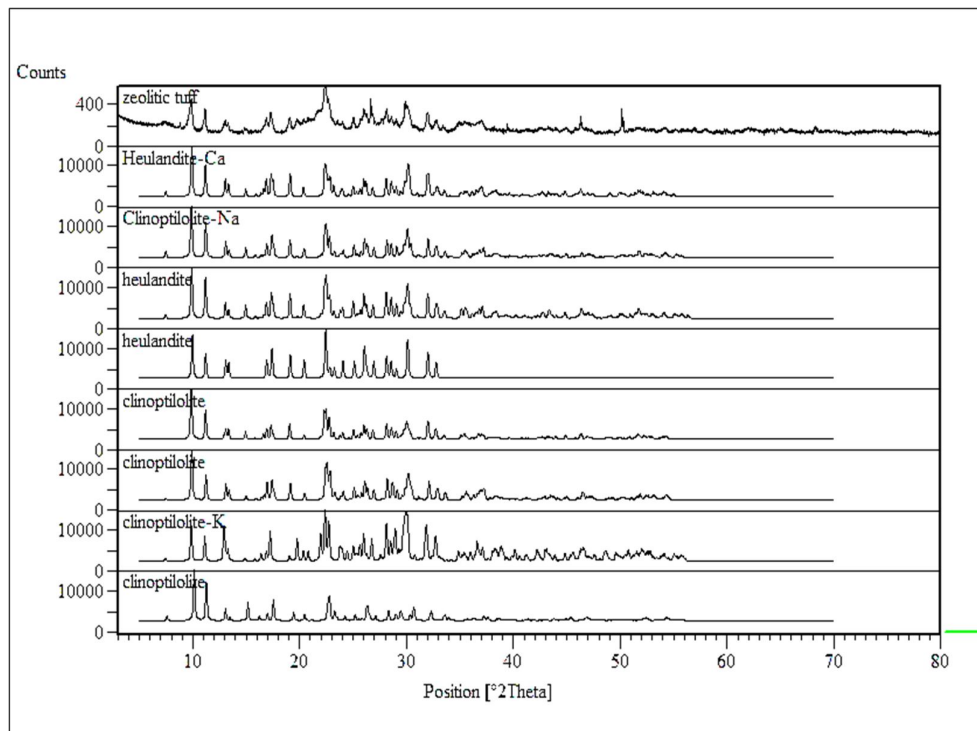


Figure 2.6. The XRD patterns of several Heulandite and Clinoptilolite minerals ("JCPDS PDF-2 Database," 2004) compared with the obtained XRD pattern of tuff-1.

Using thermal treatment in association with XRD was introduced by (Mumpton 1960) to distinguish between Clinoptilolite and Heulandite. Since then this method was applied in many researches to identify Heulandite-type zeolites (Alietti A, Passaglia E 1967; Martinezramirez et al. 2006; Ming and Dixon 1986; Noh 1998; Perraki and Orfanoudaki 2004). The method is based on the thermal stability of Clinoptilolite and Heulandite and relies on the heat-induced polymorphic transformation of Heulandite (Ming and Dixon 1986). The lattice structure in various Heulandite types (e.g. Heulandite-k, Heulandite-Ca+Na, Heulandite-Ca+k, Heulandite-Sr, Heulandite-Cd) face a breakdown when heated at temperatures higher (or equal to) 360 °C, while, the structures of Clinoptilolite type minerals are stable until heating to at least 900 °C (Cruciani, 2006). In the general group of Heulandite-type framework minerals, Heulandites refer to minerals with lower silicon content (Si/Al ratio under 4), whereas, those with a Si/Al ratio higher than 4 are called Clinoptilolites (Martinezramirez et al. 2006). since the Al-O bonds are weaker than Si-O bonds, containing higher amounts of Aluminum making Al-O bonds in AlO_4 tetrahedra leads to the weakening of aluminosilicate framework structure (Martinezramirez et al. 2006). As a result, Heulandites having lower Si/Al ratio are less stable when heated to high temperatures.

For this purpose tuff-1 sample was heated in an electric oven at 450 °C for 24 hours and then it was analyzed again by powder XRD. The sample was kept at room temperature until it was cooled prior to performing the XRD. Figure 2.7 shows the XRD pattern of tuff-1 before and after heat treatment. The sharp peaks in the XRD pattern of heat treated sample located at 2θ values of 27.39, 27.48, 27.67, 41.58 and 41.72 degrees were attributed to *Sanidine*, a “*potassium feldspar*” that was present as a minor impurity in the sample.

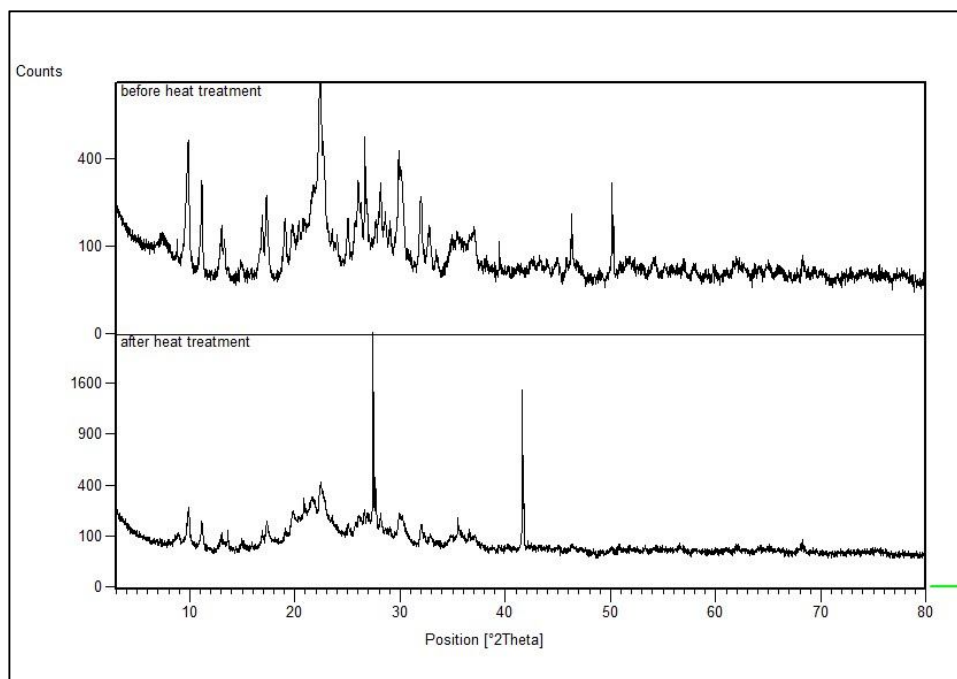


Figure 2.7. The XRD patterns of tuff-1 before and after heat treatment at 450 °C.

The main features in the XRD pattern of the heat treated sample are herein discussed. The small peak at $2\theta=7.41^\circ$ was disappeared as the result of heat treatment. The peak located at ≈ 8.89 stayed entirely unchanged after heating, however, its I_{rel} was increased caused by the reduction of the intensities of reflections from Heulandite-type zeolites. The peaks at $2\theta=9.85$ and $2\theta=11.14$, though reduced to half the intensity they had before heat treatment, were not entirely disappeared; their I_{rel} values were almost unchanged. The highest peak ($I_{rel}=100\%$) after heat treatment (excluding the Sanidine peaks) was observed at $2\theta\approx 22.4^\circ$ (d-spacing=3.97) which conforms to highest peak before heat treatment. This peak also lost half its intensity as a result of heat treatment. At $2\theta=22.62^\circ$ no peak was distinguishable in the XRD pattern before treatment, while, after heat treatment a peak in the form of a shoulder was observed in this location. This peak, corresponding to d-spacing of 3.93\AA conforms precisely to the XRD pattern of

Heulandite (Treacy 2001). There is another shoulder in the proximity of 22.71° (where a major peak was observed before heat treatment) which can be attributed to Clinoptilolite. However several overlapping peaks may be present in the 2θ range of 22 to 23 degrees. Although there are peaks in this range which share location (i.e. 2θ value) with peaks in the XRD patterns of either Heulandite or Clinoptilolite, the reduction of the heights (intensities) of all peaks implies that there may be an intermediate phase with characteristics between those of Heulandite and Clinoptilolite.

In Heulandite-type zeolites, which also include Clinoptilolite, three types of Heulandite have been identified in the literature (Bish D.L. 2001; Martinezramirez et al. 2006; Noh 1998). Heulandite type I is the least alkali-containing phase in the group of Heulandite-type zeolites with a Si/(Al+Fe) ratio between 3.5 and 3.8. Heulandite type I is mainly distinguished by the complete decomposition of its structure when heated to up to 450°C (Bish D.L. 2001). In temperatures higher than 360°C the aluminosilicate framework of Heulandite-I is transformed irreversibly to a the so-called B-phase (or type B Heulandite) and thus the peaks assigned to Heulandite-I in the XRD pattern are disappeared (Bish D.L. 2001; Martinezramirez et al. 2006; Noh 1998). By the Heulandite end of the Heulandite-type zeolites group we mean Heulandite-I. Heulandite type II, being less siliceous than Heulandite-I with a Si/(Al+Fe) ratio between 3.2 and 3.6, has higher concentrations of alkalis (Na, K and Ca) (Bish D.L. 2001). Heulandite-II exhibits an indefinite performance when heated to temperatures up to 450°C , as it may either completely or partially transform to a B-phase (Noh 1998). Partial transformation of a Heulandite-type zeolite to a B-phase results in the reduction of the peaks assigned to the respective mineral in the XRD pattern, instead of disappearing of the peaks (Perraki and Orfanoudaki 2004). This “peak intensity reduction” caused by heat treatment may also be encountered when Heulandite type and Clinoptilolite are both present separately in the material (Martinezramirez et al. 2006). Type III Heulandite is so different from the other two, with respect to chemical composition, that it is sometimes simply referred to as Clinoptilolite (Bish D.L. 2001), i.e. it is assumed to be the end-member Clinoptilolite. While, some other researchers consider Heulandite-III as a composite phase of Heulandite-Clinoptilolite with a Si/(Al+Fe) ratio between 3.6 and 4.1 (Noh 1998). By regarding the ability of Heulandite to exhibit a continuous solid solution

between Heulandite and Clinoptilolite (Cho, Maruyama, and Liou 1987), in this research the second approach is adopted, that is considering the end-member Clinoptilolite and the composite phase Heulandite-III to be two distinct phases. Heulandite-III does not break down (does not transform to a B-phase) at temperatures close to 450°C and its framework structure stays intact up to about 650°C (Bish D.L. 2001). Hence Heulandite-III, when being heated, is less stable than Clinoptilolite which is stable at temperatures even higher than 900°C.

In the XRD patterns of tuff-1 sample, the first peak at $2\theta=7.41^\circ$ was totally disappeared when it was heated at 450°C for 24 hours. In addition, the intensities of the peaks assigned to Heulandite-type zeolites were all reduced to an almost similar order of magnitude; this can be seen in Figure 2.8. This uniformity in the reduction of peak intensities is particularly important in the 2θ range between 22 and 23 degrees where several peaks of two end-members of the Heulandite-type zeolites (i.e. Heulandite-I and Clinoptilolite). Considering this fact, the possibility of both end-members being present in the sample as two separate phases is ruled out. This is also supported by scanning electron microscope (SEM) image of the sample which was previously presented by (Burak Uzal 2007) (Figure 2.9) in which the observed crystals cannot be surely attributed to a specific Heulandite type while they are more like Clinoptilolite crystals with respect to crystal size. Heulandite-I exhibits large (macroscopic) crystals in a size range of 0.2-2 cm, in contrast, Clinoptilolite has microscopic crystals between 2-20 μm in size (Bish D.L. 2001). Microscopic crystals of the Heulandite-type zeolite were observed in the SEM. The fact that Heulandite-III does not experience polymorphic transformation at 450°C leads us to conclude that the Heulandite-type zeolite in tuff-1 sample is *Heulandite type II*.

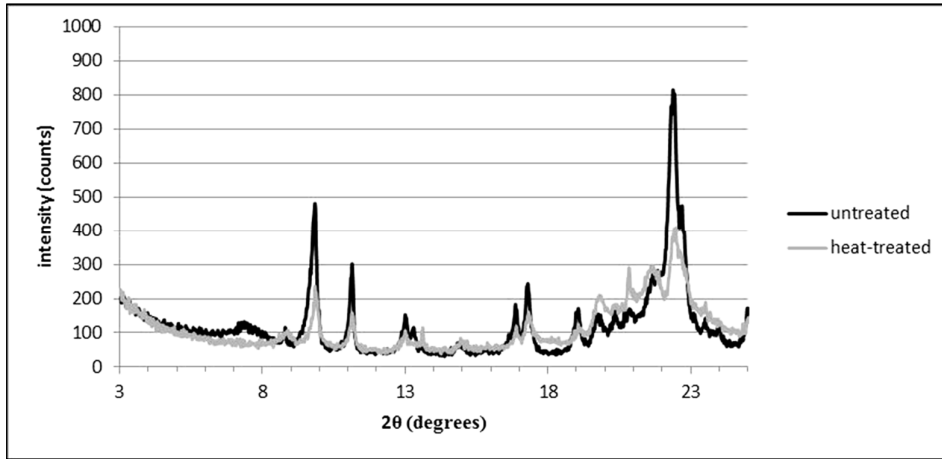


Figure 2.8. Illustration of peak intensity reduction in the XRD patterns of tuff-1 before and after heat treatment.

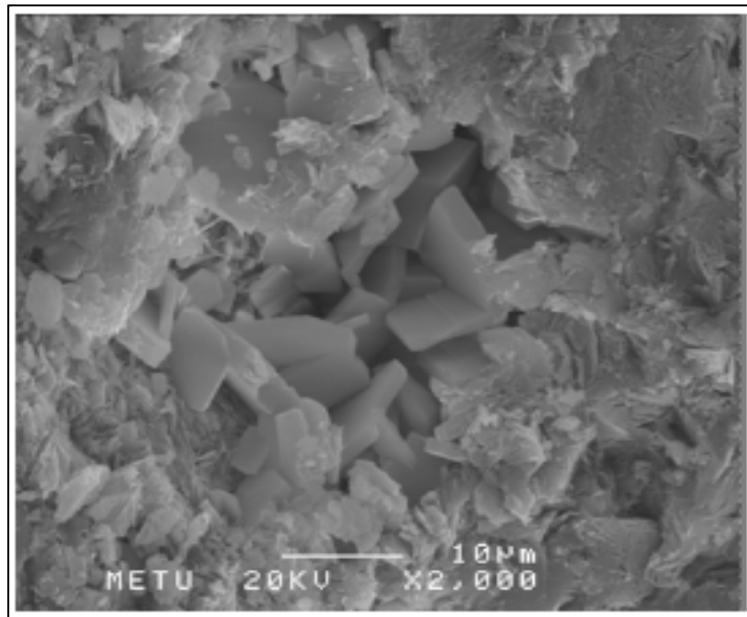


Figure 2.9. SEM image of tuff-1 (Uzal, 2007)

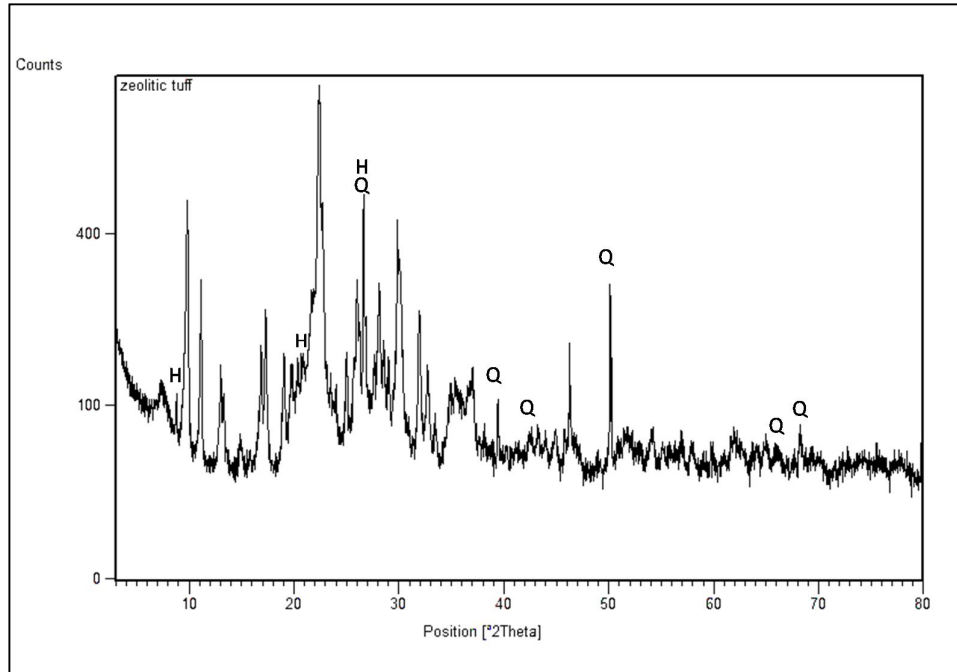


Figure 2.10. Peaks assigned to quartz (Q) and Clay mineral (H) in the XRD pattern of the non-heat-treated tuff-1 sample.

Other minerals identified through the XRD analysis of tuff-1 sample were **quartz** (SiO_2 , quartz alpha) and clay minerals. Among clay minerals **hydrated Halloysite** (chemical formula $\text{Al}_2\text{Si}_2\text{O}_5(\text{OH})_4 \cdot 2\text{H}_2\text{O}$) which is an aluminosilicate belonging to the clay minerals category (figures 2.10 and 2.11) was best conforming to the XRD pattern of tuff-1.

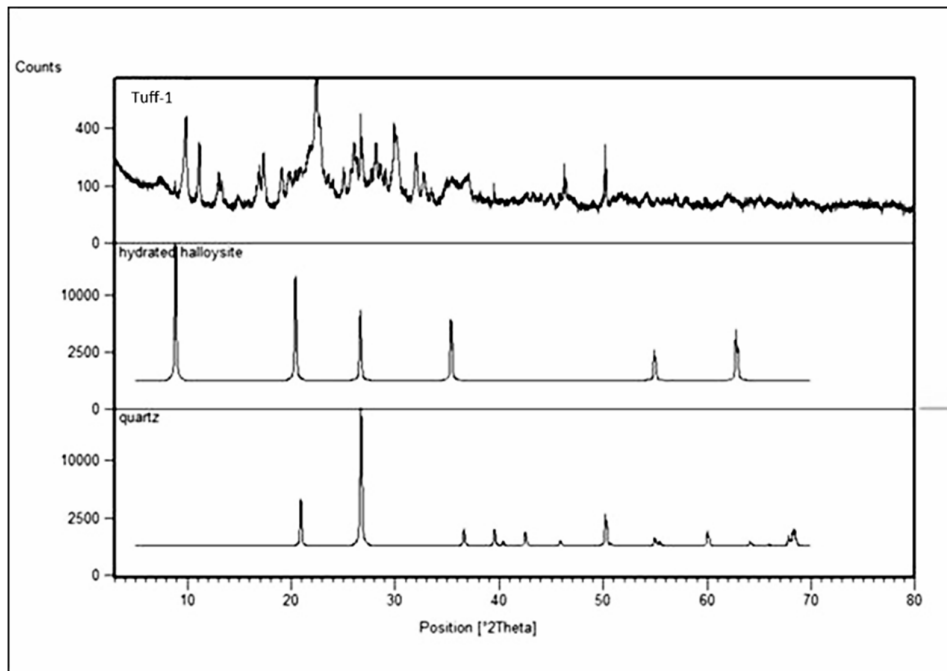


Figure 2.11. Simulated XRD patterns of quartz and hydrated Halloysite compared with the XRD pattern of non-heat-treated tuff-1.

2.3.2 Powder XRD analysis of anhydrous perlite

Figure 2.12 shows the XRD pattern of the perlite powder. The green line in Figure 2.12 shows the background. As seen in the figure, a big hump appeared in the XRD pattern which is an indication of the amorphous nature of the material. The hump-shaped zone in the XRD pattern covers a 2θ range in which the major peaks of Quartz included. The highest-intensity peak ($I_{rel}=100$) of quartz is located at $2\theta=26.59$ that, as seen in Figure 2.12, is located within the hump-shaped range. This implies that the amorphous phases in the perlite sample have silicic nature. Presence of amorphous siliceous phases is desirable with respect to pozzolanic activity. The amorphous siliceous phases and their effect on the XRD pattern was also reported in (Erdem, Meral, Tokyay, and Erdoğan 2007).

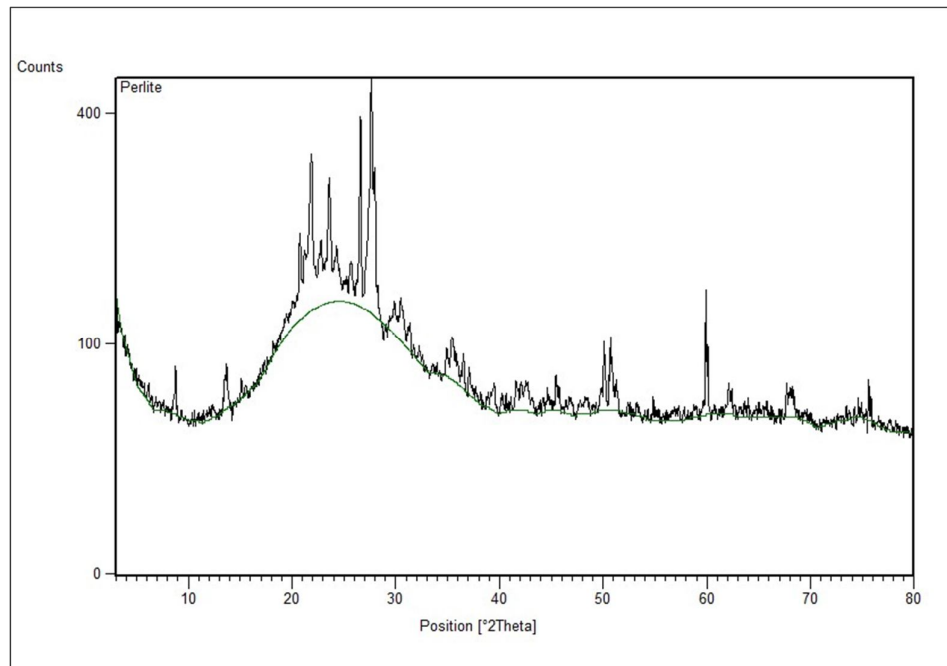


Figure 2.12. XRD pattern of Perlite powder.

The peaks assigned to quartz are very clearly observed in the XRD pattern that is the indication of the presence of *quartz* in the perlite sample. Based on the published XRD patterns of minerals (“JCPDS PDF-2 Database” 2004) and the environment of mineral generation being perlite rock, which is a volcanic glass, it is concluded that the peaks located in the proximity of $2\theta=8.76$ and $2\theta=13.54$ correspond to *mica minerals* and *feldspars* respectively. However, due to the similarity of crystal structures of minerals in a group (micas or feldspars) it is difficult to definitely assign the peaks to one mineral. Therefore, we conclude that the major crystalline phases constituting the studied perlite sample are Quartz, feldspar minerals and mica minerals (see Figure 2.13 for peak assignment). In the following we attempt to find distinct feldspar and mica minerals whose XRD patterns and chemical composition best fit to those obtained for the perlite sample.

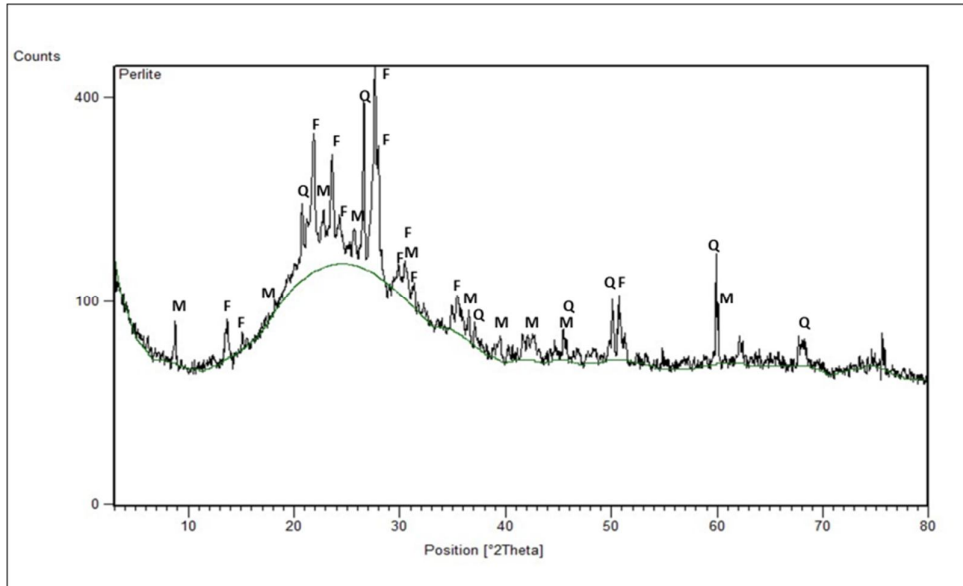


Figure 2.13. Illustration of the peaks corresponding to Quartz (Q), Feldspar (F) and Mica (M) in the XRD pattern of perlite.

Mica minerals are a group of sheet silicates (also called phyllosilicates). Among phyllosilicates, only some micas, namely muscovite, phlogopite, biotite, and lithium micas can occur in igneous rocks and the other phyllosilicates are low-temperature and low-pressure minerals (Wenk H.-R. 2005). Regarding the chemical composition of the perlite sample, the absence of Lithium rules out lithium micas, hence, we keep the remaining three minerals (muscovite, Biotite and Phlogopite) as candidate minerals. The presence of Fluorine makes Phlogopite and Biotite more likely to be present in the sample while the presence of Iron (Fe) augments the probability of the presence of Biotite. The chemical formulas of Phlogopite, Biotite and Muscovite are presented in the following (according to (Wenk H.-R. 2005)):

- Phlogopite: $\text{KMg}_3\text{AlSi}_3\text{O}_{10}(\text{OH}, \text{F})_2$
- Biotite: $\text{K}(\text{Mg}, \text{Fe})\text{Si}_3(\text{Al}, \text{Fe}^{3+})\text{O}_{10}(\text{OH})_2$
- Muscovite: $\text{KA}_2\text{Si}_3\text{AlO}_{10}(\text{OH})_2$

Figure 2.14 presents the simulated XRD patterns of the three candidate micas (“JCPDS PDF-2 Database” 2004) compared with the XRD pattern of the perlite sample. Taking the peak conformance and the chemical compositions into account, we assigned the mica-induced peaks in the XRD pattern of the perlite sample to *Biotite*.

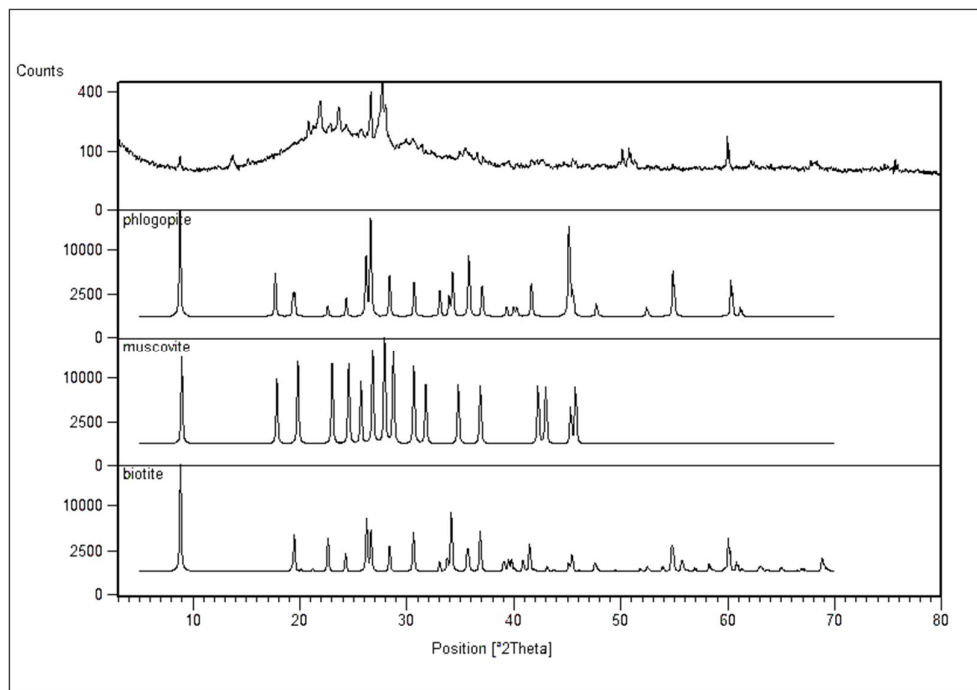


Figure 2.14. The XRD patterns of the perlite sample and candidate micas.

Feldspars are very important “framework silicate” minerals that occur in almost every metamorphic and igneous rock. Mica minerals are generally Potassium-rich and among most important mica minerals only Paragonite

($\text{NaAl}_2\text{Si}_3\text{AlO}_{10}(\text{OH})_2$) contains Sodium in its chemical formula. Thus, considering the chemical composition of the perlite sample, the candidate feldspar mineral is more likely to be a Sodium-rich “*Alkali feldspar*” phase containing a small amount of Potassium and Calcium (Wenk H.-R. 2005). In Figure 2.15 the classification of feldspars on the basis of chemical composition is presented.

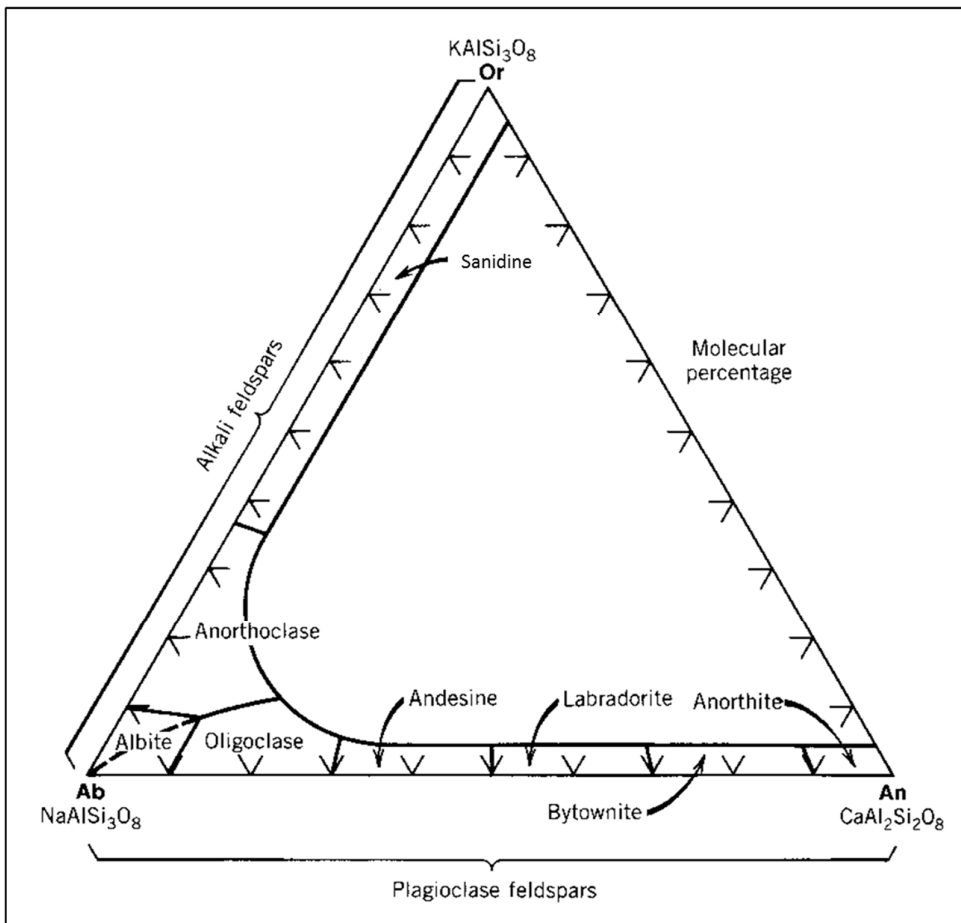


Figure 2.15. Feldspar series classified on the basis of chemical composition. Ternary presentation of composition (Wenk H.-R., 2005).

From the XRD pattern of the perlite sample four candidate feldspars were selected, namely Anorthoclase, Anorthite, Albite and Sanidine. All these feldspars are very abundant and can occur in volcanic rocks. Figure 2.16 presents the simulated XRD patterns of these four candidates (“JCPDS PDF-2 Database” 2004) along with the XRD pattern of the perlite sample.

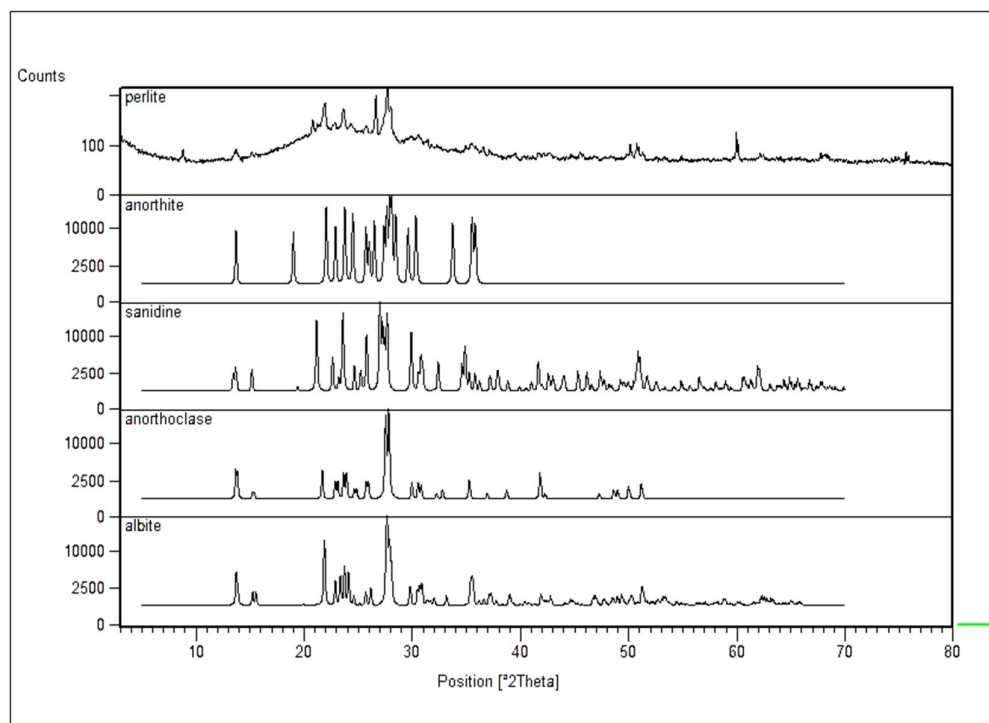


Figure 2.16. The XRD patterns of perlite and candidate feldspars.

The chemical formulas of these four candidates are as follows(Wenk H.-R. 2005):

- Anorthite: $\text{CaAl}_2\text{Si}_2\text{O}$
- Albite (Albite high): $\text{NaAlSi}_3\text{O}_8$
- Anorthoclase: $(\text{Na}, \text{K})\text{AlSi}_3\text{O}_8$
- Sanidine: KAlSi_3O_8

We should have in mind that the empirical chemical formulas may vary from the presented chemical formulas, for example Albite can contain Calcium whereas Calcium is not included in its chemical formula. However, it should be noted that in a solid solution environment, as is the case here, the phase compositions can vary significantly and intermediate phases can be present. Anorthite is plagioclase feldspar which does not contain Sodium or Potassium, thus it is not further considered as a candidate. Sanidine is Potassium-rich and contains no or negligible amount of sodium and none of Calcium. Albite, considering Figure 2.16 and the chemical formula, can contain both Potassium and Calcium and considerable amount of Sodium. Nevertheless we here discuss on the basis of known chemical formula of the minerals with emphasis on end-members. To make our assumptions more precise, the XRD patterns can be used by comparing the position (and relative intensities) of peaks in the XRD patterns of candidate minerals with the peaks observed in the XRD pattern of perlite sample. Albite also showed the best conformance to the XRD pattern obtained for the perlite sample. Therefore we, considering the above-presented discussions, assigned the feldspar-induced peaks to *Albite* phase.

2.3.3 Powder XRD analysis of tuff-2

Figure 2.17 shows the XRD pattern obtained for the tuff-2 sample. Four different phases were identified through XRD analysis, namely Quartz, alkali feldspar, mica and a calcium silicate mineral. As discussed in the previous section, feldspars are not easily differentiated from each other by XRD analysis and this difficulty also applies to the minerals belonging to mica group. Therefore from XRD pattern we can say for sure that there are *quartz*, an *alkali feldspar* mineral, a *mica mineral* and a *calcium silicate* mineral present in the tuff-2 sample. To determine

the exact minerals in the sample the end members of the groups were considered and their XRD patterns (from the available databases) and chemical compositions were compared with those obtained for the tuff-2 sample. The minerals which best justified the peaks in the XRD pattern and the chemical composition of tuff-2, were selected as existing phases.

The feldspar-induced peaks were assigned to *Anorthoclase* (chemical formula $(\text{Na}, \text{K})\text{AlSi}_3\text{O}_8$) and the mica-induced peaks were assigned to *Muscovite* (chemical formula $\text{KAl}_2\text{Si}_3\text{AlO}_{10}(\text{OH})_2$). The peaks in the XRD pattern of these two minerals conform to the peaks observed in the XRD pattern of tuff-2 with respect to peak positions (2θ) and intensities. Regarding the chemical compositions (explained in the previous section) and Figure 2.15, by the presence of Anorthoclase and Muscovite the Potassium and Sodium contents in the material are justified. The Calcium silicate mineral is responsible for the high Calcium content of tuff-2 sample. The peaks corresponding to Quartz phase exhibited low intensities which can be related to the low Silicon content in the tuff-2 sample; in fact the XRD showed that the quartz content in the sample was negligible.

The exact identity of the Calcium silicate mineral could not be determined through XRD. However there are natural minerals containing Calcium silicates as their main constituents, for example *Hartrurite* was found in Palestine with empirical chemical formula $\text{Ca}_{2.97} \text{Al}_{0.01} \text{Ti}_{0.01} \text{SiO}_5$ (John W. Anthony, Richard A. Bideaux, Kenneth W. Bladh, and Monte C. Nichols 2003), the industrial equivalent of Hartrurite is called Alite (impure C_3S) which is the primary source of strength in ordinary Portland cement. Carbonation of the Calcium silicate phase will be discussed in thermal analysis of tuff-2 sample (section 2.4.3.).

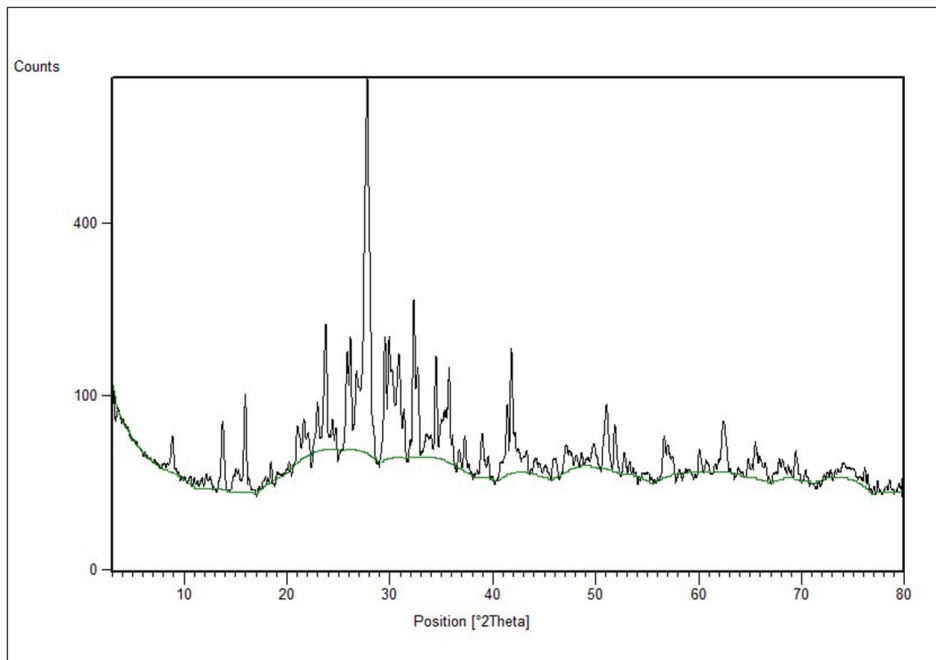


Figure 2.17. XRD pattern of tuff-2 sample.

Figure 2.18 shows the XRD patterns of the discussed candidate minerals (simulated from (“JCPDS PDF-2 Database” 2004)) compared with the XRD pattern of tuff-2. In Figure 2.19 the main peaks corresponding to each of the identified phases are labeled in the XRD pattern of tuff-2. The phase labels are Q: Quartz, M: Muscovite, F: Anorthoclase, C: Calcium silicate mineral.

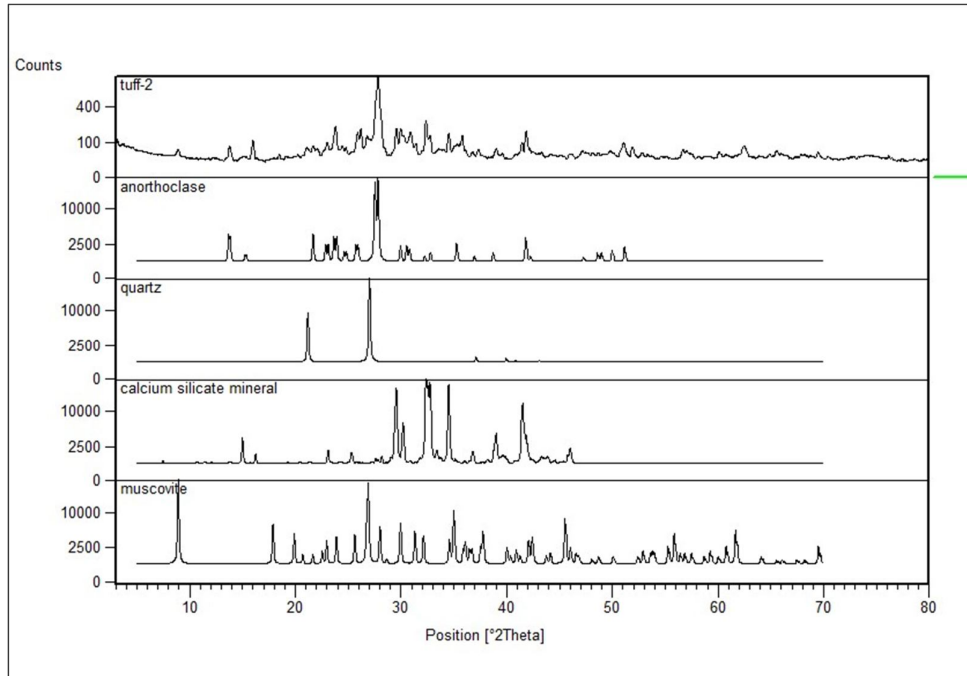


Figure 2.18. XRD pattern of tuff-2 and simulated XRD patterns of Anorthoclase, Quartz, Muscovite and the Calcium silicate mineral.

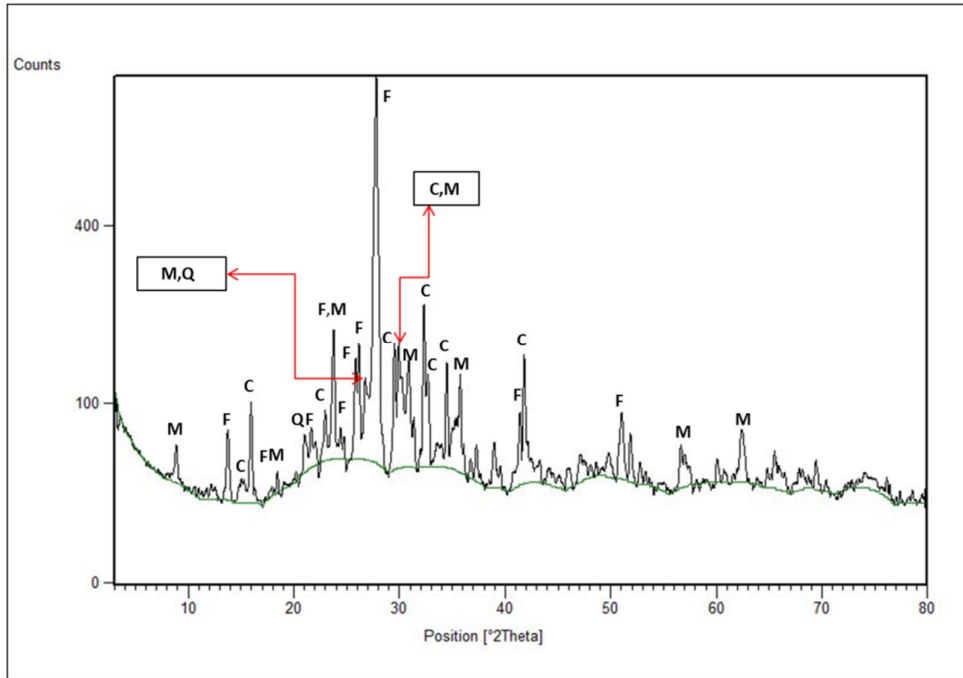


Figure 2.19. Main peaks of the identified phases in the XRD pattern of tuff-2.

2.3.4 Powder XRD analysis of white Portland cement (WPC)

The XRD pattern of white Portland cement is presented in Figure 2.20. The analysis of the peaks which appeared in the XRD pattern of WPC lead to identification of the following crystalline phases:

- Calcium silicate phases, namely tricalcium silicate or as it is called in cement nomenclature C_3S (Ca_3SiO_5) and dicalcium silicate or C_2S (Ca_2SiO_4)
- Tricalcium aluminate or C_3A ($Ca_3Al_2O_6$) which can also be called “*Calcium Aluminum Oxide*”
- Calcium sulfate ($CaSO_4$) which is also called “*Anhydrite*”.
- Calcium carbonate or Calcite ($Ca(CO_3)$). It is probably due to carbonation of the WPC.

- A carbonation product other than Calcite, this phase will be thoroughly discussed in XRD and NMR analyses of the hydrated WPC in chapter 3 (sections 3.4 and 3.5).

The peaks assigned to any of these identified phases are labeled and presented in Figure 2.20. The peaks corresponding to each identified phase are labeled as following: tricalcium silicate (A), dicalcium silicate (B), Calcium carbonate (C), Calcium sulfate (S), tricalcium aluminate (T). The main characteristic peak of the non-calcite carbonated phase is labeled by *.

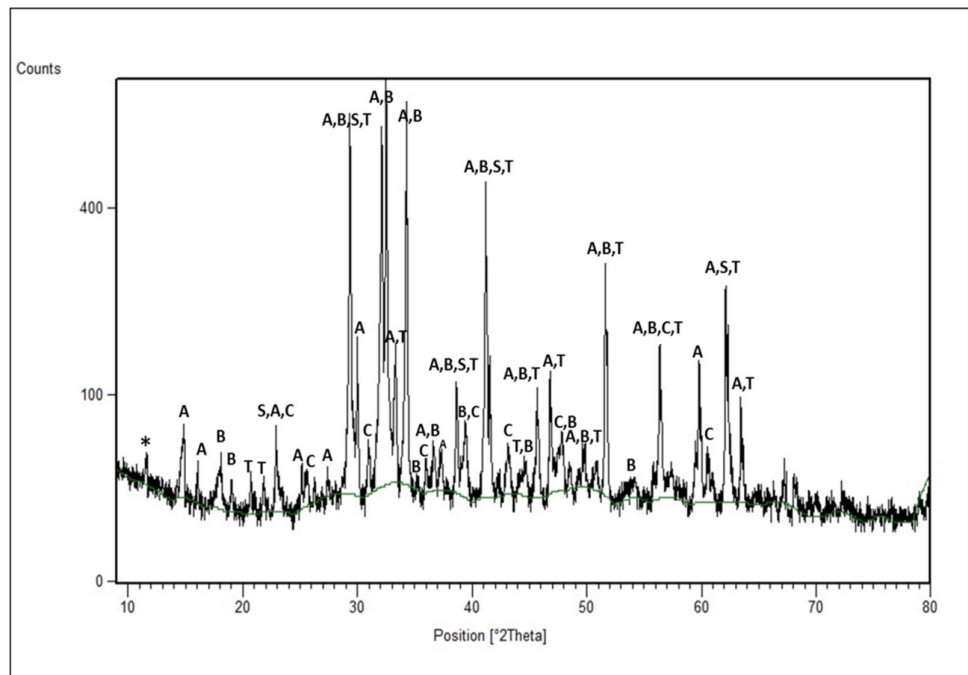


Figure 2.20. XRD pattern of WPC.

2.4 Thermal analysis (TGA) of anhydrous materials

Thermal analysis covers the techniques which monitor or investigate the physical and/or chemical changes caused in the material by temperature variation. A material may undergo physical or chemical changes such as phase transition, crystallization, phase decomposition, dehydration, decarbonation, etc. as a result of temperature changes; by thermal analysis these changes can be studied in a continuous manner as a function of temperature and/or time. In this study we utilized thermogravimetry analysis (TGA).

TGA continuously measures the mass of the material while the temperature varies over a certain temperature range. Hence, the mass loss or gains occurring in the material at different temperatures are monitored. In this study the mass loss by the increase in temperature was the factor of interest in order to detect primarily the water loss, and possibly phase decomposition, phase transformations occurring in the samples. Since in the XRF analysis Hydrogen could not be detected therefore TGA was used for determination of water content in anhydrous materials.

The TGA technique was conducted in Nitrogen atmosphere in the temperature range of 20-1100°C and at an increase rate of 10°C/min. The powder samples described in section 2.1.2 were used. The amount of samples used in the analysis of WPC, tuff-1, tuff-2 and perlite were 44.56 mg (milligrams), 16.25 mg, 44.66 mg and 16.25 mg respectively.

2.4.1 TGA analysis of tuff-1

Figure 2.21 shows that the tuff-1 sample contained a significant amount of water which resulted in mass loss of 10.7% when the sample was heated up to 1100°C. However, the whole percentage of mass loss cannot be solely attributed to water loss as trace metal oxides within the material can be volatilized at high temperatures (>550°C). The most obvious characteristic distinguishing zeolites from other framework silicates are cavities in the framework (in the form of channels and cages) usually occupied by H₂O molecules, However, this is not a reliable means for distinguishing different zeolites from each other (Korkuna et al. 2006). The presence of these open cavities leads to a more open framework structure compared to other framework silicates (Wenk H.-R. 2005). Therefore, the presence of high amounts of water in the tuff-1 sample is justified by the occupation of cavities in the

Heulandite phase by water molecules. It should be noted that the water in zeolite minerals can be reversibly lost by heat and regained upon being exposed to moisture.

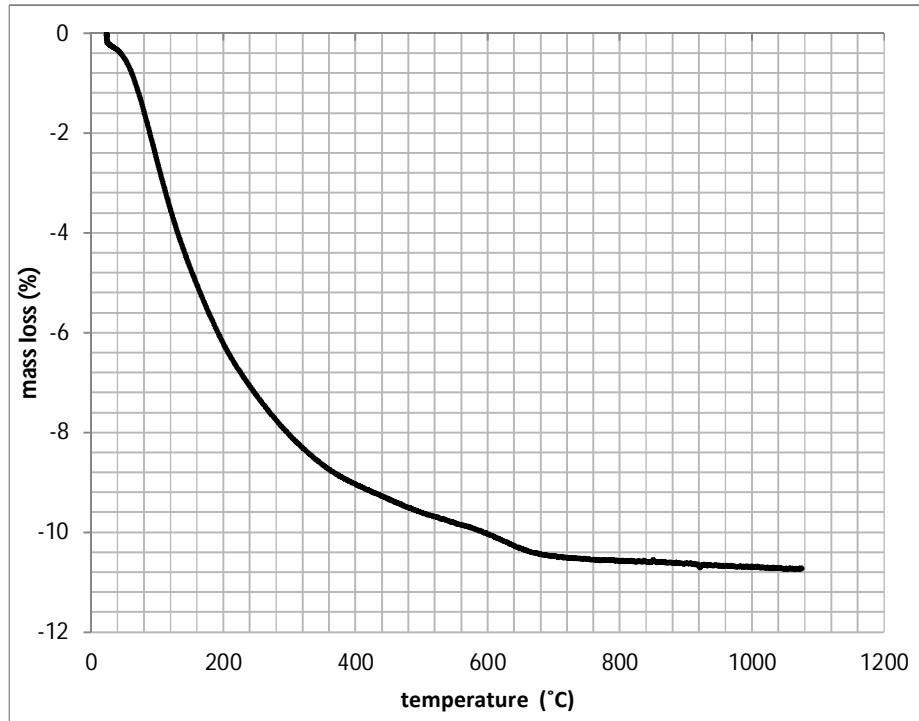


Figure 2.21. The TGA curve of tuff-1.

2.4.2 TGA analysis of perlite

Figure 2.22 gives the TGA curve of perlite. The mass loss at temperatures between 20 and 550°C can be, with good certainty, attributed to water loss of the perlite. The majority of the mass loss in this temperature range occurred between 20

and 200°C which is attributed to vaporization of the water adsorbed by perlite. Using Nitrogen environment for the test makes the combustion of substances impossible; therefore, the possibility of mass loss due to combustion of carbonated substances is ruled out and the high-temperature mass loss is attributed to the loss of chemically bound water and the trace metal oxides. It was suggested by (Ramachandran 2001) that there is a small quantity of water captured in the silicate structure; this water escapes upon the decomposition of the structure by heating to temperatures higher than 900°C when the silicates melt. The TGA curve obtained in the present research approves the statement of (Ramachandran 2001).

The mass loss as a result of heating up to 1100°C was measured as 3%. This implies that the perlite sample contained slightly less than 3% water which is in good agreement with the values recorded in the preceding literature for gray perlite (Erdem, Meral, Tokyay, and Erdoğan 2007; Keller, w.D., Picket 1954). The significant drops or bounces in the curve observed in the ranges of 600-700°C and 800-1100°C were caused by noises in the data acquisition.

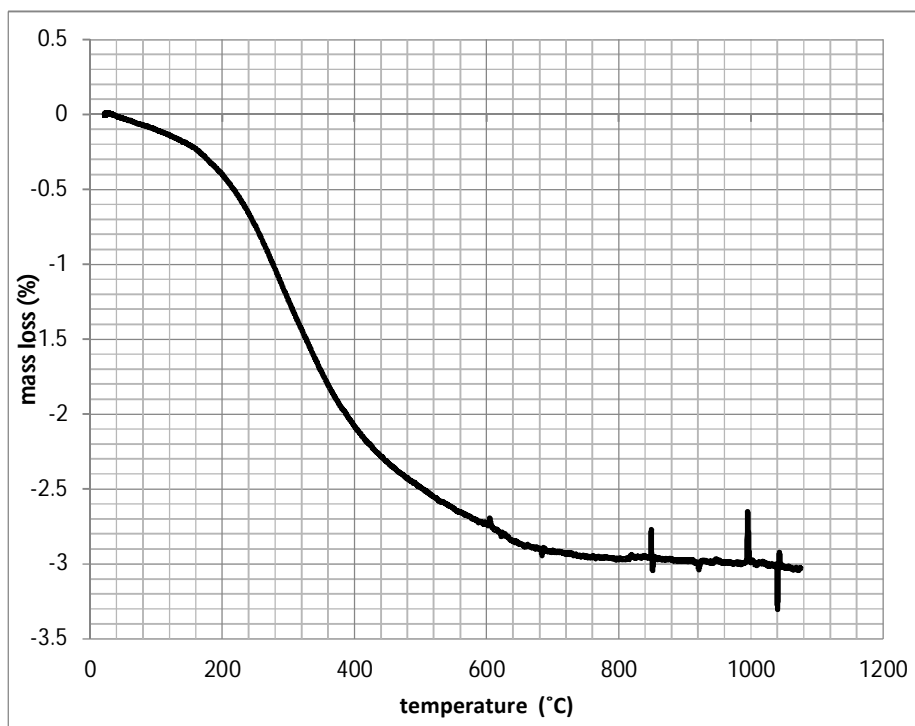


Figure 2.22. TGA curve of perlite.

2.4.3 TGA analysis of tuff-2

In the TGA curve of tuff-2 sample (Figure 2.23), a continuous mass loss up to about 600 °C was observed while a dramatic drop appeared between 600 and ca.730°C. In a Feldspar-rich material the continuous water loss is expected as the structure alters by temperature, this can happen even at temperatures higher than 900 °C as explained in sections 2.4.1 and 2.4.2 and it can be seen in the Figure. The considerable mass loss in 600-730°C range can be attributed to dehydration of Calcite formed as a result of carbonation. Observation of Calcium silicate phase in XRD and NMR analyses (sections 2.3.3 and 2.5.6) strengthens the possibility of the occurrence of carbonation in tuff-2 sample. In XRD analysis of tuff-2, the characteristic peaks of Calcite could be observed, however they were not showed on

the XRD pattern because the peaks had severe overlapping with high-intensity peaks of other phases. Therefore, we could not be sure about the presence of Calcite until the application of TGA technique.

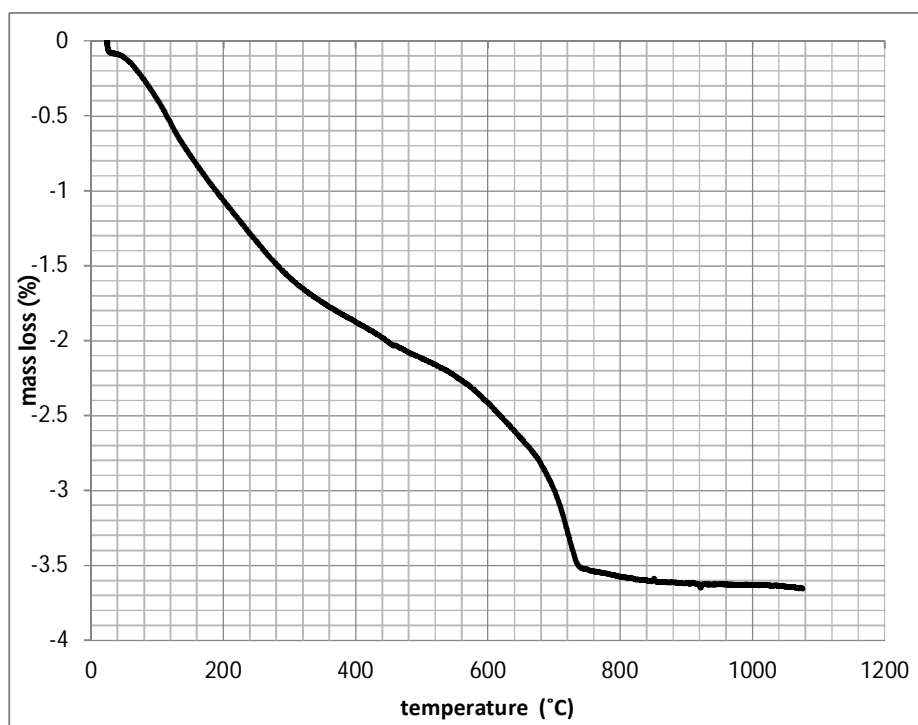


Figure 2.23. TGA curve of tuff-2.

2.4.4 TGA analysis of WPC

Figure 2.24 gives the TGA curve for the anhydrous WPC. The most significant mass loss (3 %) occurred between 600 and 780°C; this mass loss is

attributed to decomposition of Calcite ($\text{Ca}(\text{CO}_3)$) which was formed as a result of the carbonation of WPC. In temperature range of 20 to ca. 110°C adsorbed water is lost. The drop in the mass loss-temperature curve, about 0.1%, which occurred between 110 and ca. 120°C , can be attributed to dehydration of C-S-H phase. The WPC can take up some moisture from the environment during storage and hydrate slightly; this is in agreement with the mass loss between ca. 400 and ca. 450°C which is attributed to dehydration of Calcium hydroxide. Gypsum ($\text{CaSO}_4 \cdot 2\text{H}_2\text{O}$) dehumidification occurred between 120 and 200°C in two steps including the conversion of gypsum to hemihydrate gypsum ($\text{CaSO}_4 \cdot 0.5\text{H}_2\text{O}$) and then conversion of hemihydrate to anhydrite (CaSO_4). The continuous mass loss over the temperature ranges of $200\text{-}400^\circ\text{C}$ and $450\text{-}600^\circ\text{C}$ can be caused by dehydration and/or decomposition of various phases. For examples Aluminum hydrated oxides dehydrate between 200 and 400°C and MgCO_3 decomposes between 550 and 610°C . It is worth mentioning that some overlapping may occur among the above mentioned temperature ranges.

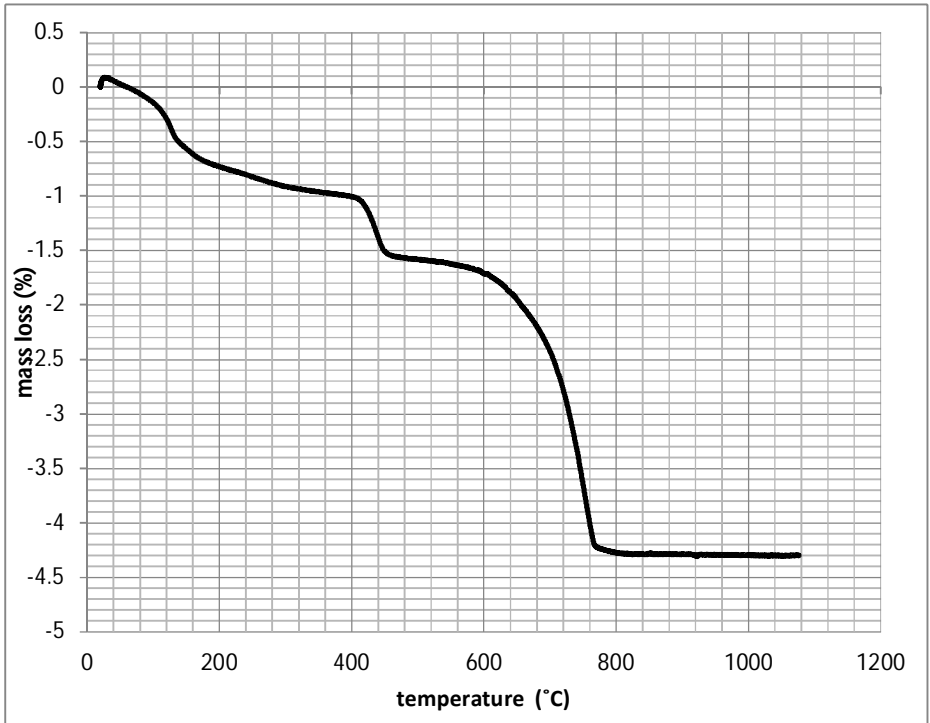


Figure 2.24. TGA curve of WPC.

2.5 Nuclear magnetic resonance (NMR) spectroscopy

2.5.1 Considerations about solid-state NMR spectroscopy

Direct investigation using techniques such as microscopy has only provided fragments of information that are mostly qualitative (Jennings 2000). Therefore in addition to techniques such as electron microscopy (SEM/TEM), indirect analytical investigation techniques such as NMR and XRD are necessary (J. Young and Sun 1999a). Due to the amorphous nature of C-S-H and the limitations of XRD associated with this type of materials, structural studies should be performed by techniques not dependent upon long-range structural order, such as MAS NMR (Black et al. 2006).

Solid-state ^{29}Si Nuclear Magnetic Resonance Spectroscopy (*NMR*) has been used extensively to study the hydration process and hydration products of cement and related compounds (C_3S and C_2S) with and without the addition of reactive SiO_2 (i.e. Supplementary cementitious materials) (Sun, Brough, and Young 1999). Numerous studies on cement hydration products specially C-S-H have been conducted utilizing ^{29}Si MAS NMR. This technique is applicable for detection of various silicate species with various degrees of anion condensation and consequently various degrees of silicate polymerization, namely Q^0 , Q^1 , Q^2_{B} , Q^2_{P} , Q^3 , Q^4 , their substituted forms such as $\text{Q}^2(\text{1Al})$ and their hydrated forms such as $\text{Q}^0(\text{H})$. Q^0 refers to silicon atoms in a mono-silicate tetrahedron, Q^1 shows silicon in end group silicate tetrahedra, Q^2 is the designation used for silicon in chains of silicate tetrahedra, Q^3 is used for silicon atoms in silicate tetrahedra in planes (cross-linked silicates) and silicon atoms in silicate tetrahedra in a 3-D network are designated as Q^4 (Lippmaa and Mägi 1981).

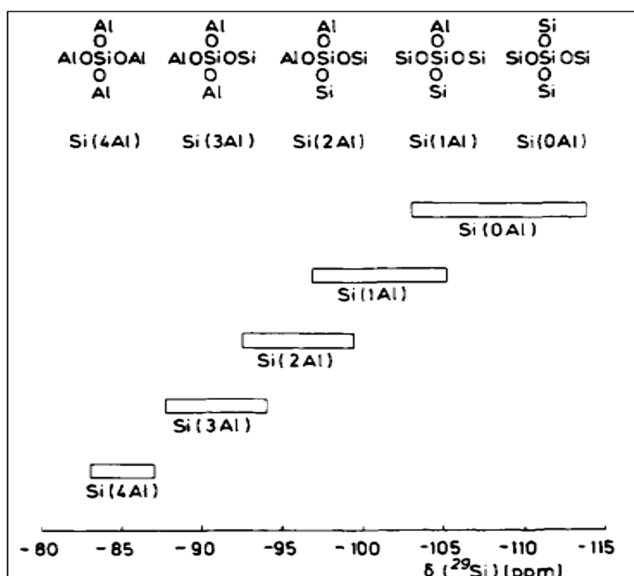


Figure 2.25. Chemical shift ranges of ^{29}Si nucleus in various Q^4 silicate species (Lippmaa and Mägi 1981)

Extensive studies on the structure of aluminosilicates using ^{29}Si NMR technique resulted in setting chemical shift (δ) ranges for various (alumino)silicate species (Figure 2.25 and Table 2.5). In Figure 2.25, the Si annotation represents the silicon atom in Q^4 environment, i.e. connected to four other tetrahedra.

It is very important to mention that the cation effects (caused by incorporation of different ions in the aluminosilicate structure) and the peculiarities in the geometry of molecular units cause significant variation in the values of chemical shift of ^{29}Si (and also ^{27}Al) nuclei, and thus leads to overlapping of the chemical shift ranges presented in Figure 2.25 and Table 2.5. The effects of changes in the Si-O-Si and/or Al-O-Si bond angles and distortion of tetrahedral units on the chemical shifts in ^{29}Si NMR are common examples in this respect. Therefore, in this study the chemical shift ranges of Q^n units that do not contain tetrahedral Al were assumed to be separate and do not overlap. Accordingly, the major chemical shifts were assigned by this assumption and then the Al substituted species were identified from the intermediate peaks (Magi et al. 1984).

Table 2.5. ^{29}Si Chemical shift ranges for various silicate species (J. Young and Sun 1999b).

Connectivity	Type	Chemical shift range (δ) [ppm]
Q ⁰	Orthosilicate (monomer)	-66 to -74
Q ¹	Pyrosilicate (dimer)	-77 to -82
Q ²	Linear chain or ring	-85 to -89
Q ³	Cross-linked chain	-92 to -100
Q ⁴	3-D network	-103 to -115

The data obtained by NMR spectroscopy can be used to determine the following factors:

- The mean silicate chain length of the C-S-H (Brough et al. 1994; Brunet et al. 2010; Méducin et al. 2007; I.G. Richardson 2008; Rodger and Groves 1988).
- The quantity of different silicate species (Nonat 2004; I. Richardson 1999; Skibsted, Jakobsen, and Hall 1995) and possibly the degree of hydration of the cementitious materials or pozzolanic activity of SCMs (Justnes and Meland 1990).
- The incorporation of guest ions such as Al^{3+} , OH^- and Ca^{2+} , in C-S-H structure and their location (Andersen, Jakobsen, and Skibsted 2003)
- The atomic ratios such as Ca/Si and Al/Si (a. V. Girao et al. 2007; Girão et al. 2007, 2010)

Solid-state ^{27}Al NMR is usually applied complementarily with ^{29}Si NMR. This technique is proved to be a very useful tool to probe Al sites in cement-based materials, and it can be used to detect, distinguish, characterize and quantify

different Al species and their accommodating sites; By difference in ^{27}Al chemical shift we can observe and distinguish between various coordinations of Aluminum, namely tetra-, penta- and octa-coordinated Al sites, in C-S-H [As shown in (Andersen, Jakobsen, and Skibsted 2003, 2004; Martinezramirez et al. 2006; Mozgawa et al. 2002; Pardal, Brunet, and Charpentier 2012; Ian G Richardson et al. 1993; Skibsted J., Jakobsen H.J. 1994)and (R. Taylor, Richardson, and Brydson 2010)].

Tetrahedral Aluminum (or tetra-coordinated Aluminum) is the Aluminum atom in tetrahedral sites of AlO_4 found within the aluminosilicate network. Aluminum in AlO_4 sites has Oxygen atoms as the nearest neighbor atoms and it can have either Silicon or other atoms as next nearest atomic neighbor. Tetra-coordinated ^{27}Al nucleus (Al_{IV}) is detected in NMR by observation of peaks in the range of +50 to +85 ppm (Mozgawa et al. 2002; Shtepenko et al. 2006).

Penta-coordinated Aluminum (Al_{V}) is Aluminum atom in extra-framework (or non-framework) Aluminum sites. Al_{V} can be identified from its peak in ^{27}Al NMR in the vicinity of 35 ppm. In addition, incorporation of guest ions (other than Al^{3+}) in the aluminosilicate structure can result in Aluminum sites in which these atoms act as the next nearest atomic neighbors to Aluminum; this can lead to down-field or up-field shift of tetrahedral Aluminum peaks. For example tetrahedral Aluminum having Boron as next nearest atomic neighbor (such as $\text{Al}(\text{OB})_4$) shows peaks at smaller chemical shifts (Xiu, Wang, and Liu 2011). Another type of extra-framework (or non-framework) Aluminum sites are octa-coordinated aluminum units which can be detected in ^{27}Al NMR data by peaks in the chemical shift range of -20 to about +20 ppm. Sometimes this Aluminum species can cause peaks at values higher than 20 ppm (20 to 30 ppm).

Incorporation of each four-coordinated Aluminum (AlO_4 tetrahedron) in C-S-H structure shifts the ^{29}Si signals in ^{29}Si NMR spectra to the low field by about 5-6 ppm (Brunet et al. 2010; Magi et al. 1984). Furthermore, there is a linear correlation between the intensities of ^{29}Si spectra of Al-incorporated species (e.g. $\text{Q}^2(1\text{Al})$) and the quantities of Al incorporated in the C-S-H phase (Andersen, Jakobsen, and Skibsted 2003). Therefore through detection of tetrahedral Al sites by

^{27}Al MAS NMR, the accuracy of ^{29}Si NMR spectra can also be examined and the peak assignment in ^{29}Si NMR can be corrected (Brunet et al. 2010).

All NMR experiments were conducted using a Bruker 400 MHz SS NMR AVANCE III spectrometer (BrukerBioSpin, Rheinstetten, Germany). The ^{29}Si NMR spectra were recorded at a resonance frequency of 79.495 MHz by collecting 2k transients with 30 s recycle delay under 14 kHz spinning rate using a triple-resonance 4 mm Bruker MAS probe. The 1D ^{27}Al NMR spectra were recorded at a resonance frequency of 104.266 MHz by collecting 1024 transients with 2 s recycle delay with 14 k spinning rate using a Double Resonance Broadband BB/1H 4 mm Bruker CP/MAS probe. Prior to Al acquisition, the Al chemical shift was optimized using Aluminum hydroxide as external references.

All samples were prepared by packing 60-80 mg of the samples in standard 4 mm zirconia rotors from Bruker and sealed at the open end with a Vespel cap. The temperature for all experiments was kept at 298 K. Bruker Topspin 3.0 software was used for data collection and for spectral analysis. The powder samples of anhydrous and hydrated materials used in NMR study were as described in section 2.1. While explaining the NMR analyses of hydrated samples the neat WPC paste will be referred to as *HWPC* and the blended pastes will be referred to as *Htuff-1*, *Htuff-2* and *Hperlite*.

The raw data obtained from NMR spectroscopy were inserted in IGOR Pro® software in order to perform peak deconvolution and obtain quantitative information about the arrangement of peaks (position, height, width and area of the peaks). For each set of spectra (i.e. a complete ^{27}Al or ^{29}Si NMR spectrogram), the peak-containing chemical shift zones were easily distinguished in the graphs in the form of humps, broad peaks, or a set of adjacent narrow peaks. The peak deconvolution comprises the task of fitting multiple peaks within a so-called peak-containing zone such that the corresponding simulated spectrogram is as close as possible to the experimental spectrogram. In the discussion on the NMR results presented in the upcoming sections of this chapter and chapter 3, whenever the appearance of the deconvoluted peaks look misleadingly different from the experimental spectrogram such that one may think the peak fitting task is not

correctly executed, the illustration of simulated and experimental spectrograms are presented.

Once the peaks were deconvoluted, the area of each peak was calculated in IGOR Pro software. This data were used to perform quantitative analysis on ^{29}Si NMR data. Quantitative analysis was performed by dividing the area of all the peaks corresponding to each species by the total area of all observed peaks and the resulting value was expressed in percent. In a ^{29}Si NMR spectrogram, if the total number of all observed peaks is shown by t and a certain number of peaks (m) are assigned to a particular silicate species (Q^n), then the Q^n content of the material for which the ^{29}Si NMR data were obtained can be calculated by Equation 2.1.

$$C_{Q^n}(\%) = \left(\frac{\sum_{i=1}^m A_{P_i}}{\sum_{j=1}^t A_{P_j}} \right) \times 100 \quad (\text{Eq. 2.1})$$

Where,

C_{Q^n} is the Q^n content of the material expressed in percent of the total (alumino)silicate species. $\sum_{i=1}^m A_{P_i}$ is the sum of the areas of all the peaks (m peaks) assigned to Q^n species. And $\sum_{j=1}^t A_{P_j}$ is the sum of all peaks observed in the spectrogram.

The results of quantitative analysis can be used to calculate the mean silicate chain length (MCL) of the C-S-H phase in hydrated pastes. The value of MCL represents the mean number of silicate (or aluminate) tetrahedra in the (alumino)silicate chains of the C-S-H phase. This value is calculated from equation 2.2 which was suggested by (A. V. Girao 2007).

$$MCL = \frac{2}{\left(\frac{q^1}{q^1 + q^2 + 1.5 \times q^2 (1A)} \right)} \quad (\text{Eq. 2.2})$$

Where, q^1 , q^2 and $q^2(1Al)$ are the C_Q^n values for the Q^1 , Q^2 and $Q^2(1Al)$ species respectively.

2.5.2 ^{29}Si NMR spectroscopy of anhydrous tuff-1

Figure 2.26 shows the ^{29}Si NMR spectrogram of tuff-1. In order to determine the location of peaks with respect to chemical shift, peak deconvolution was performed on the NMR spectrogram and four peaks were detected in the vicinity of -96.7, -101.8, -106.9 and -111.5 ppm chemical shift positions. The result of peak deconvolution can be seen in Figure 2.27.

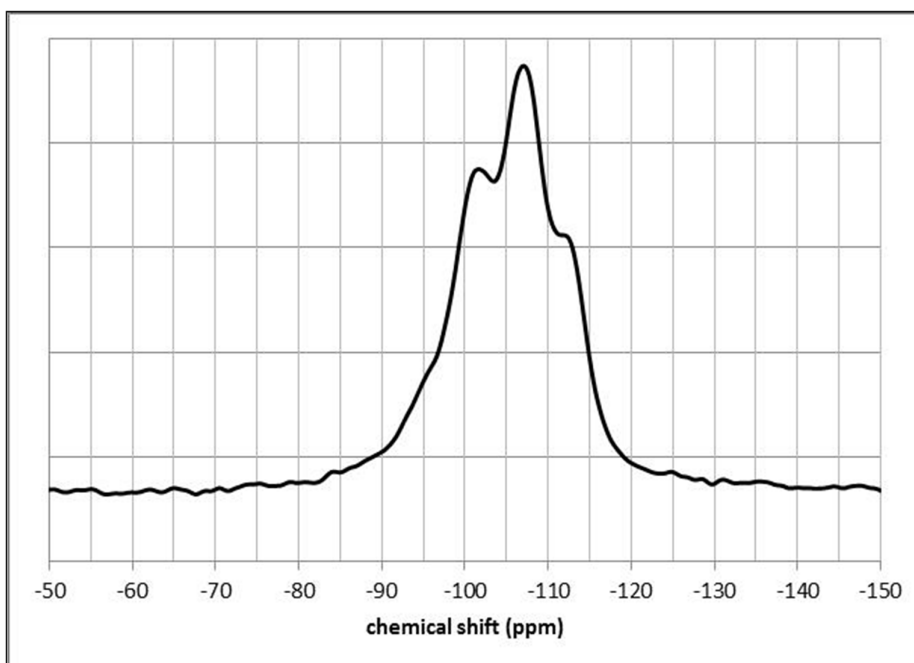


Figure 2.26. ^{29}Si NMR spectra of tuff-1.

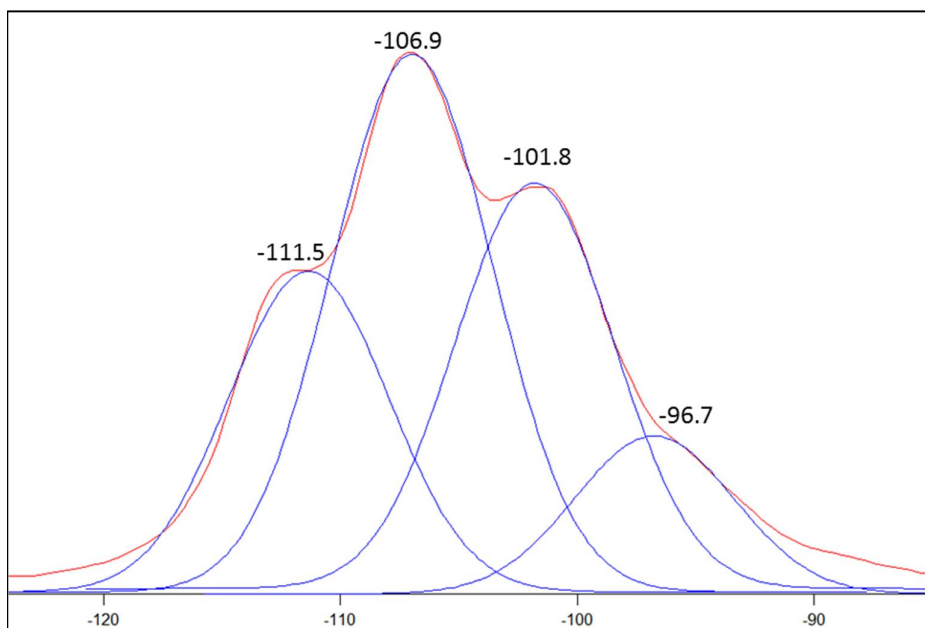


Figure 2.27. Deconvolution of peaks in ^{29}Si NMR spectrogram of tuff-1 and the respective chemical shift (ppm) of the peaks.

(J. Young and Sun 1999b) (Table 2.5) suggested the chemical shift range of -92 to -100 ppm for cross-linked silicate chains (Q^3), However as stated before, the incorporation of Aluminum into the silicate structure shifts the chemical shifts down-field. Furthermore, as reported by (Lippmaa and Mägi 1981), the (alumino)silicate structure of zeolites comprises a 3-D network of Al-substituted silicate tetrahedra. Therefore the Silicon atoms in zeolites belong to Q^4 structural units. The peak assignment was performed considering this structural characteristic of Zeolites and the identified species are as follows:

- $\text{Q}^4(2\text{Al})$ and $\text{Q}^4(3\text{Al})$: the peak at -96.7 was assumed to be indicative of the $\text{Q}^4(2\text{Al})$ species. The presence of $\text{Q}^4(3\text{Al})$ is also expected regarding the position of the peak and the hump at around -95 ppm. The peaks in this range can also have some contributions from Q^3 species, most probably $\text{Q}^3(0 \text{ or } 1 \text{ Al})$.

- Q⁴(1Al): the presence of this unit is indicated by peaks at -101.8 and -106.9.
- Q⁴(0Al): Having two considerable peaks at -106.9 and -111.5 is a strong sign of existence of this species.

It is worth mentioning that the assignment of a particular peak to a single (alumino)silicate unit is not accurately feasible because the chemical shifts of various tetrahedral sites are significantly affected by factors such as the distance between the Si and/or Al atoms (Q-Q distance) as well as the Q-O-Q angles (angles that Si and/or Al atoms make with Oxygen atom) (Ramdas and Klinowski 1984). Therefore, in this research the peak assignment was performed by taking the ranges, rather than absolute values, of chemical shifts for the (alumino)silicate species.

2.5.3 ²⁷Al NMR spectroscopy of anhydrous tuff-1

Figure 2.28 illustrates the ²⁷Al NMR spectrogram of the anhydrous tuff-1. The detected peaks were deconvoluted and shown in Figure 2.29. Six major peaks appeared at chemical shifts of 59.38, 55, 50.5, 46, 42 and 37.41 ppm. However it can be seen in Figure 2.29 that a set of very small peaks were observed in the range of -10 to +10 ppm.

Looking at Figure 2.29, one may question the accuracy of the intensity (height), location (chemical shift, ppm) and width (full width at half maximum or FWHM) of the peaks. This question may arise because the peaks do not seem to completely fit inside the obtained curve of spectrogram. In order to clarify the peak fitting process and show its accuracy, in Figure 2.30 the deconvoluted peaks and the spectrogram fitted to them (blue line) are illustrated viz-a-viz the spectrogram obtained in ²⁷NMR spectroscopy of tuff-1 (red line).

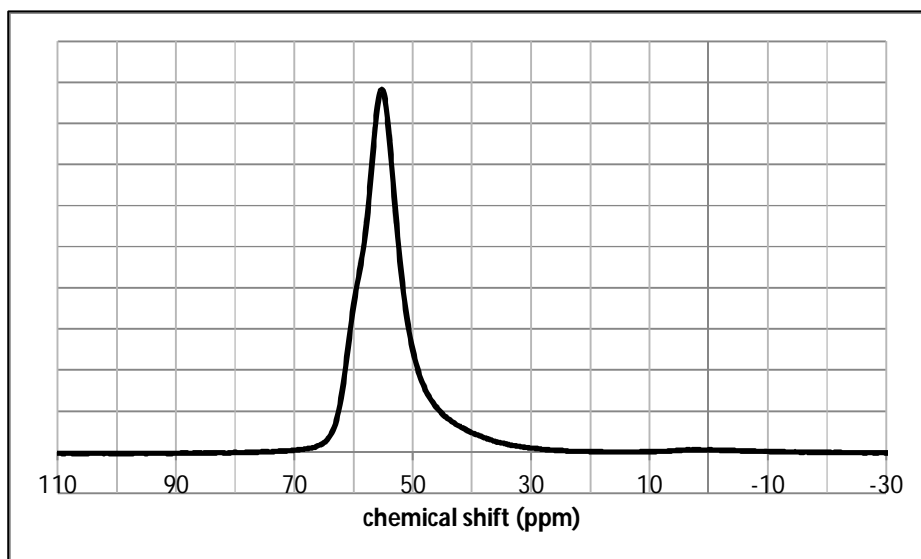


Figure 2.28. ^{27}Al NMR spectra of tuff-1.

The peaks at 59.38 and 55 ppm are assigned to tetra-coordinated Aluminum; However, the former that is observed as a shoulder in the vicinity of 60 ppm can be attributed to deformed forms of AlO_4 tetrahedra (Mozgawa et al. 2002). In most papers which have studied the ^{27}Al NMR spectra of zeolitic materials (Martinezramirez et al. 2006; Mozgawa et al. 2002; Ian G Richardson et al. 1993), the only peaks detected in the range of 20-100 ppm were a high-intensity peak at around 55 ppm and the shoulder in proximity of 60 ppm, while the shape of the ^{27}Al NMR spectra implies that there should be other peaks in this range.

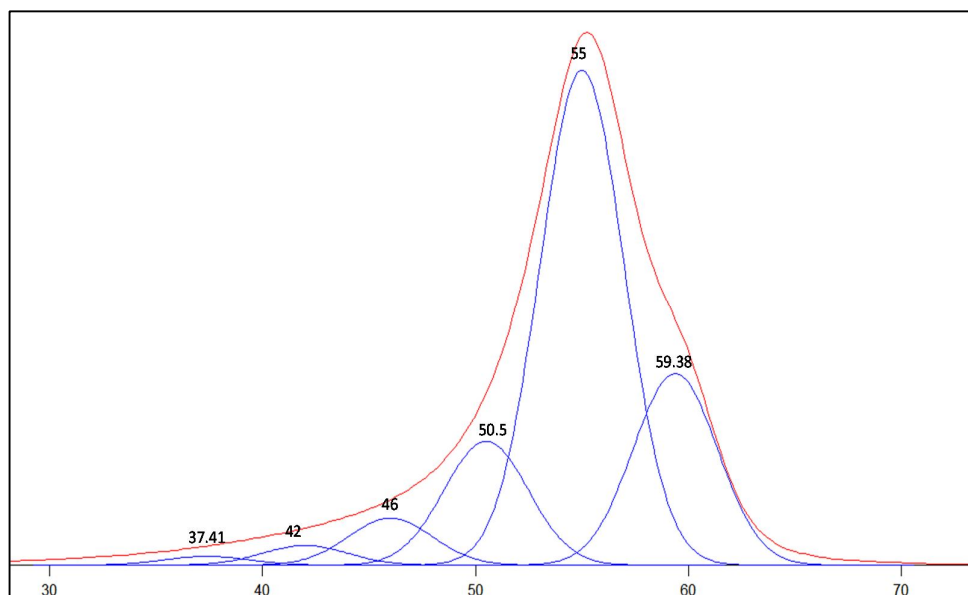


Figure 2.29. Deconvolution of peaks in ^{27}Al NMR spectrogram of tuff-1.

The peaks at 46 and 42 ppm were assigned to tetrahedral Aluminum having other atoms as next nearest atomic neighbors. Existence of Boron (B_2O_3) in the tuff-1 sample (1.72 % (wt.)) supplies further support to this assignment. The peak at 37.41 was assigned to penta-coordinated Aluminum sites. By the observation of a very small hump region between -10 and +10, arises the possibility of a set of peaks in the chemical shift range that is the characteristic of octa-coordinated Aluminum. Aluminum in octa-coordinated sites creates peaks between -15 and +20 ppm (Shtepenko et al. 2006; Skibsted J., Jakobsen H.J. 1994). It can be concluded that in addition to small amounts of tetra-coordinated Aluminum there are even less amounts of octa-coordinated Aluminum in tuff-1 sample; therefore, although there are extra-framework Aluminum sites, the absolute majority of Aluminum in this sample are accommodated in the aluminosilicate framework

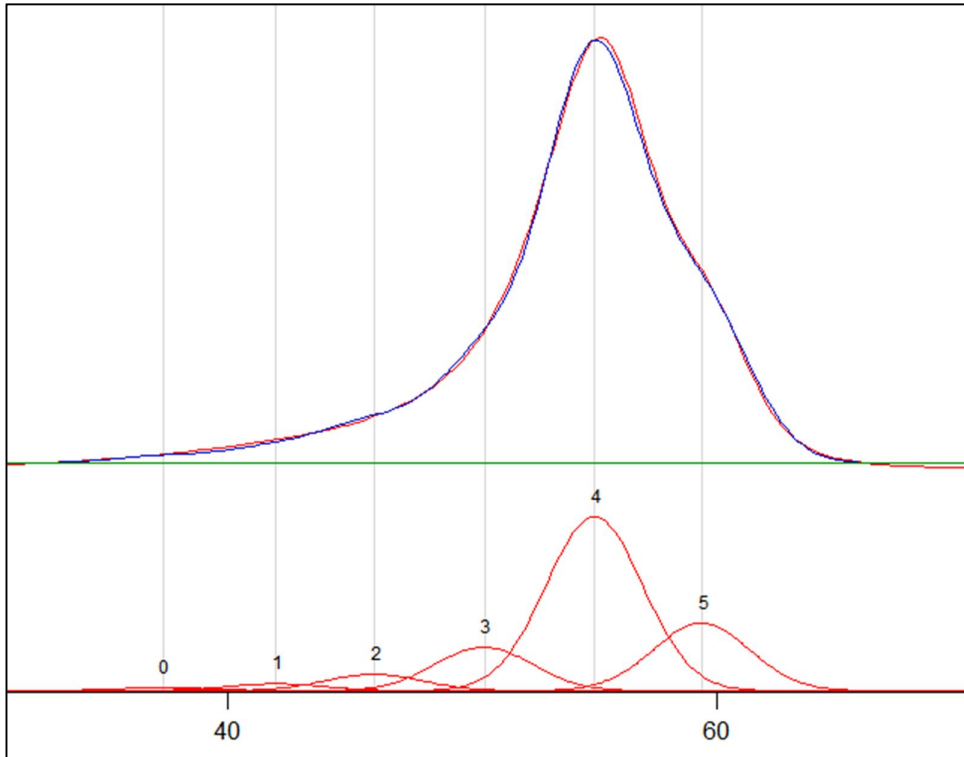


Figure 2.30. Experimental vs. simulated ^{27}Al NMR spectrogram of tuff-1.

2.5.4 ^{29}Si NMR spectroscopy of anhydrous perlite

The ^{29}Si NMR spectrogram of perlite sample is presented in Figure 2.31; it is seen in the Figure that a broad peak, stretching between ca. -80 and ca. -130 ppm, appeared in the spectra. The peak appearance observed here, is in agreement to the ^{29}Si NMR studies previously performed on volcanic glass of different origins (Petrini 2001; Petrini et al. 1999). Despite the severe peak broadening, three peaks centered at -98 and -106 and -117.7 ppm were deconvoluted within the range of the observed broad peak (figures 2.32 and 2.33).

The three detected ^{29}Si resonance peaks are located within the chemical shift ranges of Q^3 and Q^4 species. Two peaks at -106 and -117 ppm are attributed to Q^4

species, while, the peak at -98 ppm can be assigned to Q^3 species. From the ^{29}Si NMR spectra, it is understood that the (alumino)silicate phase is highly polymerized, which reportedly (Petrini 2001; Petrini et al. 1999), is a characteristic of volcanic glasses generated by cooling of the magma extruded at the first stages of eruption.

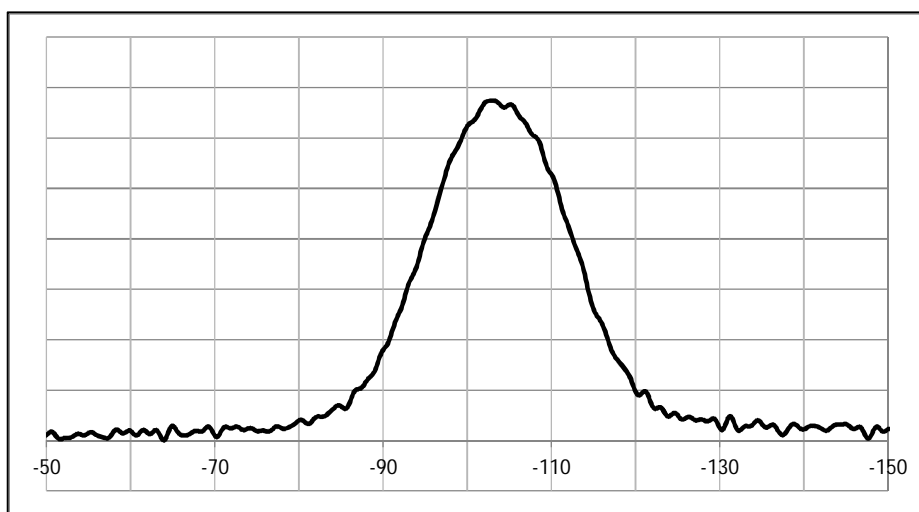


Figure 2.31. ^{29}Si NMR spectra of perlite.

The predominance of the peaks corresponding to highly polymerized Q^4 units suggests the high degree of polymerization as well as the likelihood of the presence of Aluminum substituted tetrahedral in the substance. Therefore, within the precision level of the peak fitting, the peaks at -106 and -117 ppm can be assigned to $Q^4(1 \text{ or } 2 \text{ Al})$ and $Q^4(0\text{Al})$ species respectively. However, considering the broadness of the peak appeared at -98 ppm and the high Aluminum content of the perlite sample, the probability of the presence of some Aluminum-substituted Q^3

species (i.e. $Q^3(1Al)$ and $Q^3(2Al)$) is still sustained. This probability also applies to the presence of higher levels of Aluminum substitution in Q^4 units (i.e. $Q^4(3Al)$); in fact, the relatively higher intensity of the peak at -106 ppm strengthens the possibility of high levels of Aluminum incorporation into the silicate chain structure.

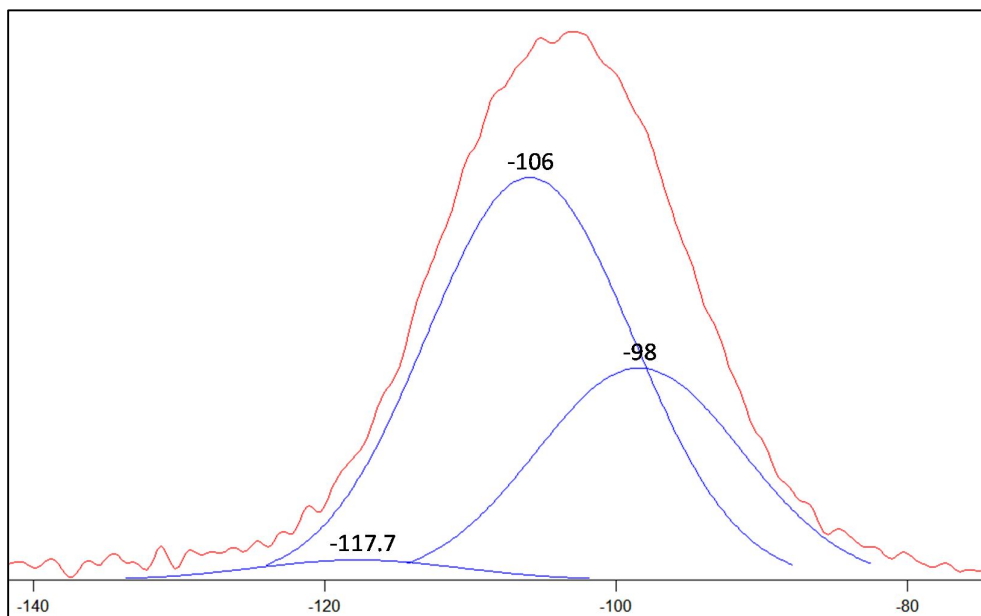


Figure 2.32. Deconvolution of peaks in ^{29}Si NMR spectrogram of perlite.

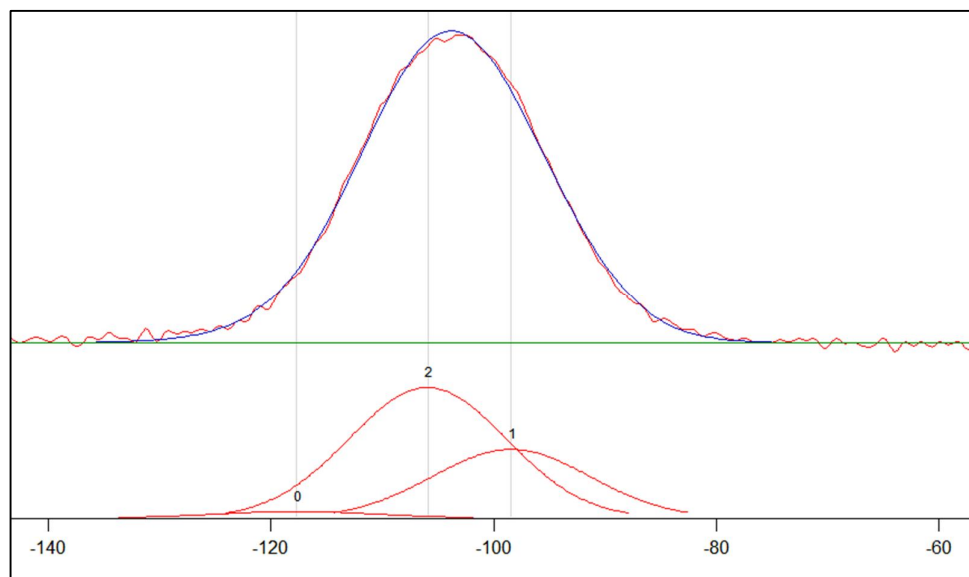


Figure 2.33. Experimental vs. simulated ^{29}Si NMR spectrogram of perlite.

2.5.5 ^{27}Al NMR spectroscopy of anhydrous perlite

The ^{27}Al NMR spectrogram of perlite (Figure 2.34) was analyzed for performing peak deconvolution (Figure 2.35). The simulated spectrogram corresponding to the deconvoluted peaks is shown in Figure 2.36.

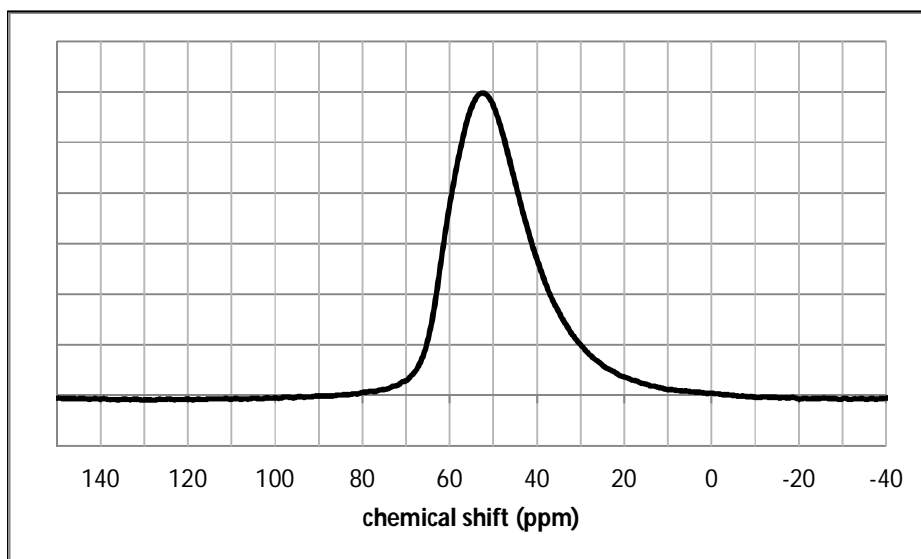


Figure 2.34. ^{27}Al NMR spectra of perlite.

According to (Mozgawa et al. 2002) the penta-coordinated Aluminum and distorted Al_{IV} species create peaks in the chemical shift range of 30 to 50 ppm. regarding the intensities of the peaks, the ^{29}Si NMR results and the chemical composition of the perlite, the peaks at 55, 47 and 37 ppm can be, with good precision, attributed to the Al_{IV} species in the aluminosilicate framework, distorted Al_{IV} (in the aluminosilicate framework) and penta-coordinated extra-framework Aluminum sites.

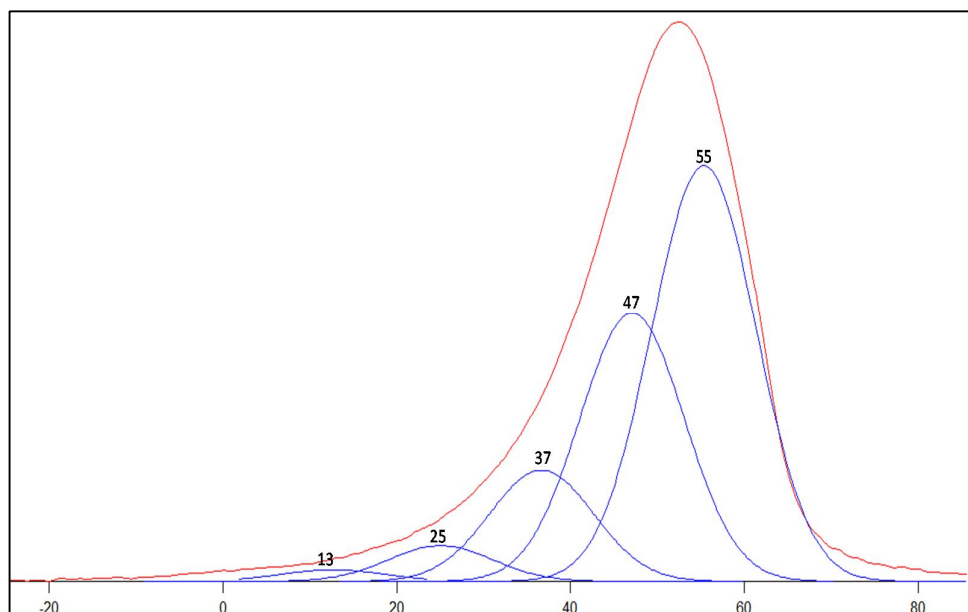


Figure 2.35. Deconvolution of peaks in ^{27}Al NMR spectrogram of perlite.

The very low-intensity peaks at 13 ppm can be attributed to octa-coordinated extra-framework Aluminum. The origin of the low-intensity peak at 25 ppm is quite difficult to be accurately identified. It can be attributed to both penta-coordinated and octa-coordinated Aluminum sites, however it is more likely to be caused by Al_{VI} species within amorphous aluminate components (Mozgawa et al. 2002).

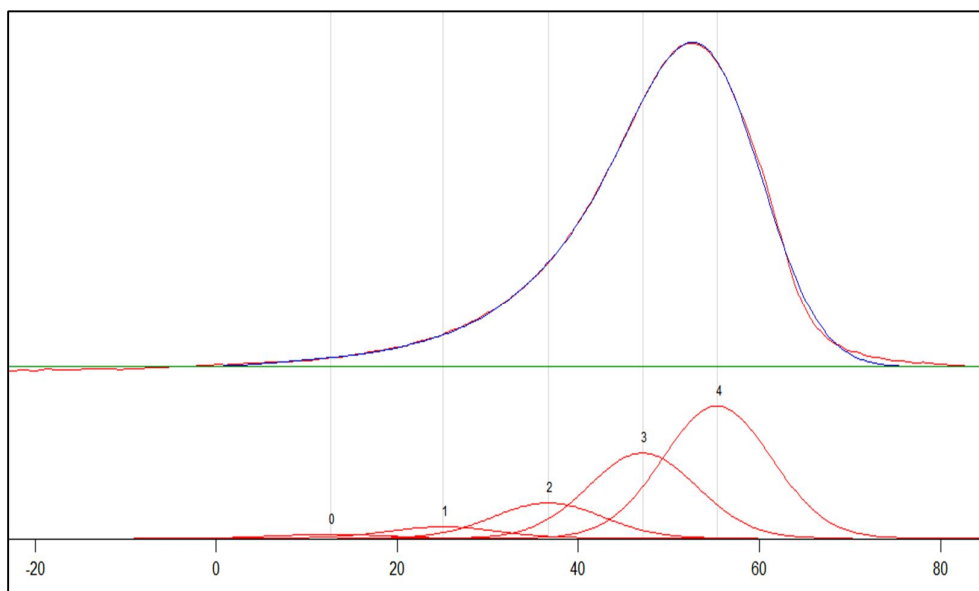


Figure 2.36. Experimental vs. simulated ^{27}Al NMR spectrogram of perlite.

The above discussed NMR peaks, indicate the predominance of the peaks corresponding to aluminosilicate framework structure, i.e. Al_{IV} species incorporated in tetrahedral Silicon sites. While, on the other hand, there are small amounts of non-framework Aluminum sites. Being in good agreement with the ^{29}Si NMR results, this implies the predominance of Al substitution for Silicon in tetrahedral sites and supports the idea that high levels of Aluminum substitution for Silicon occurred in the framework structure.

2.5.6 ^{29}Si NMR spectroscopy of anhydrous tuff-2

The ^{29}Si NMR data of tuff-2 along with the peak deconvolution and simulated spectrogram are presented in figures 2.37, 2.38 and 2.39. The peak assignments are discussed in the following according to the deconvolution performed on the diagram shown in figure 2.38.

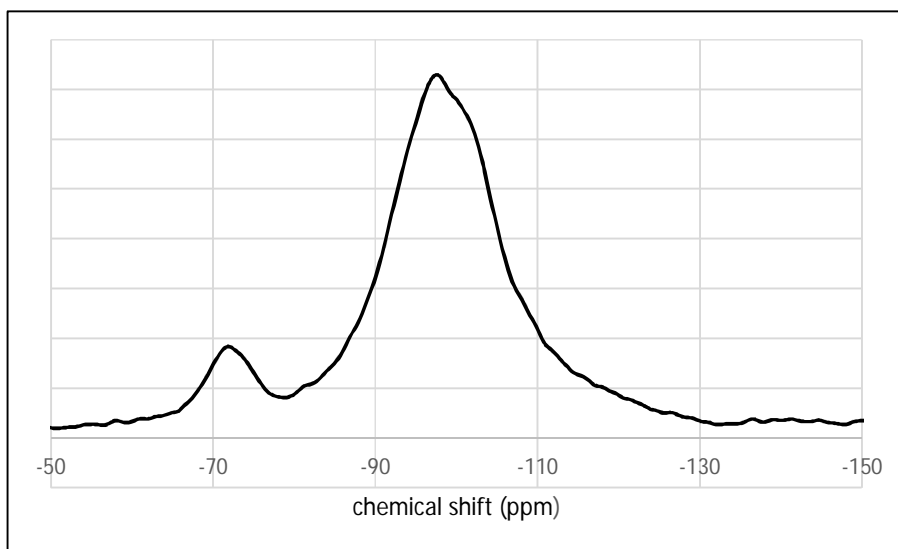


Figure 2.37. ^{29}Si NMR spectra of tuff-2.

Two major humps were observed in the plot of ^{29}Si NMR spectra of tuff-1, one broad peak-containing hump between ca. -80 and ca. -1340 ppm and one small hump in the vicinity of -71 ppm which was found to be consisting of one peak. The peaks in the chemical shift range of -80 and -130 ppm correspond to Q^2 , Q^3 and Q^4 species. Interestingly the alumino(silicate) structure of tuff-2 shows considerable divergence from that of tuff-1, as in tuff-2 (alumino)silicate units with lower degrees of polymerization are also observed despite tuff-1 which consisted almost entirely of Q^4 units. Two peaks at -81.5 and -88 ppm correspond to Q^2 units or highly Al-substituted Q^3 species, namely $\text{Q}^3(2\text{Al})$. However, to stay on the safe side we consider both these peaks to Q^2 units. Therefore, the peaks at -81.5 and -88 ppm are assigned to $\text{Q}^2(1\text{Al})$ and $\text{Q}^2(0\text{Al})$ respectively. The peaks in the range of -90 to -100 ppm (represented here with two peaks at -94 and -98 ppm) are assigned to Q^3 species which may or may not contain Aluminum ions as Silicon substitution. The peaks within the chemical shift range of -100 to -130 ppm correspond to Q^4 units with various degrees of Aluminum substitution for Silicon.

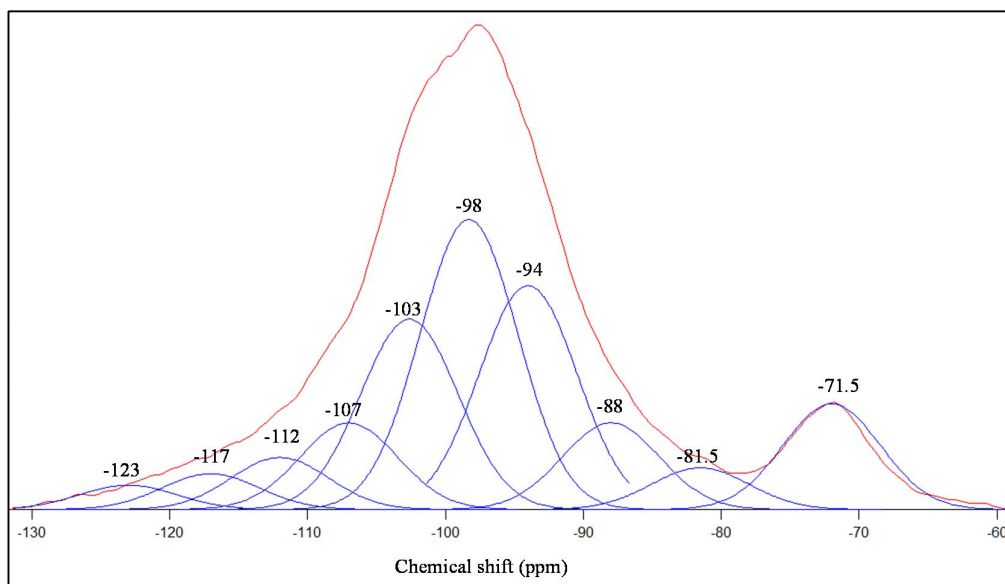


Figure 2.38. Deconvolution of peaks in ^{29}Si NMR spectrogram of tuff-2.

The most significant feature in the structure of tuff-2 was the presence of a Calcium silicate mineral phase which was observed in the XRD analysis of tuff-2 sample (section 2.3.3). The ^{29}Si NMR analysis supports the idea that the tuff-2 sample contains a Calcium silicate phase with a structure close to Alite and Belite. The ^{29}Si resonance peak at -71.5 is an indication of Q^1 species, it will be discussed in section 2.5.8 that Belite and Alite cause resonance peaks in the proximity of -71.5 ppm.

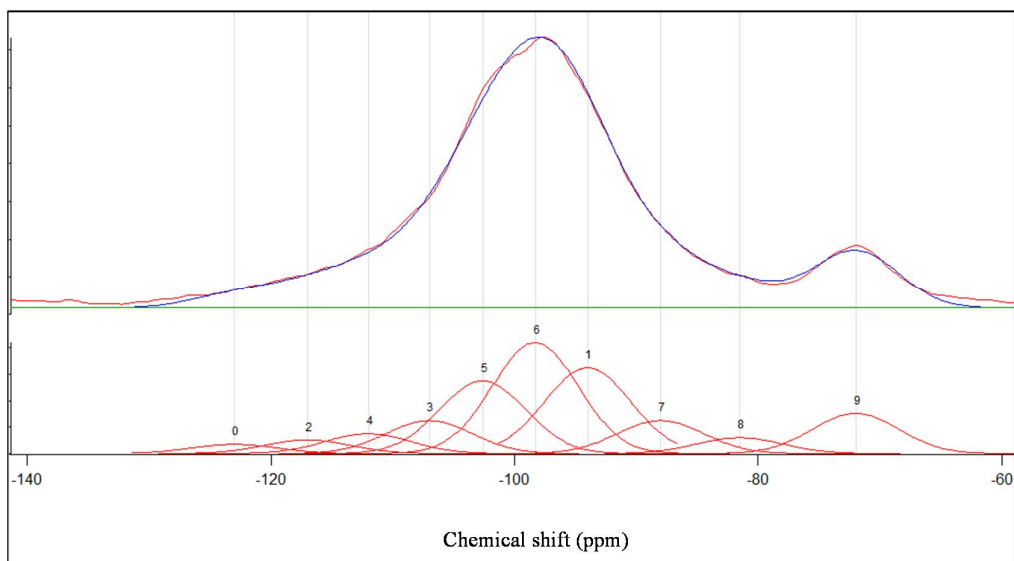


Figure 2.39. Experimental vs. simulated ^{29}Si NMR spectrogram of tuff-2.

2.5.7 ^{27}Al NMR spectroscopy of anhydrous tuff-2

Figure 2.40 gives the ^{27}Al NMR spectrogram of anhydrous tuff-2. The detected peaks deconvoluted and shown in Figure 2.41. It can be seen in figure 2.41 that the peaks are located continuously between -20 and 100 ppm. The simulated spectrogram vs. the experimental data is shown in Figure 2.42.

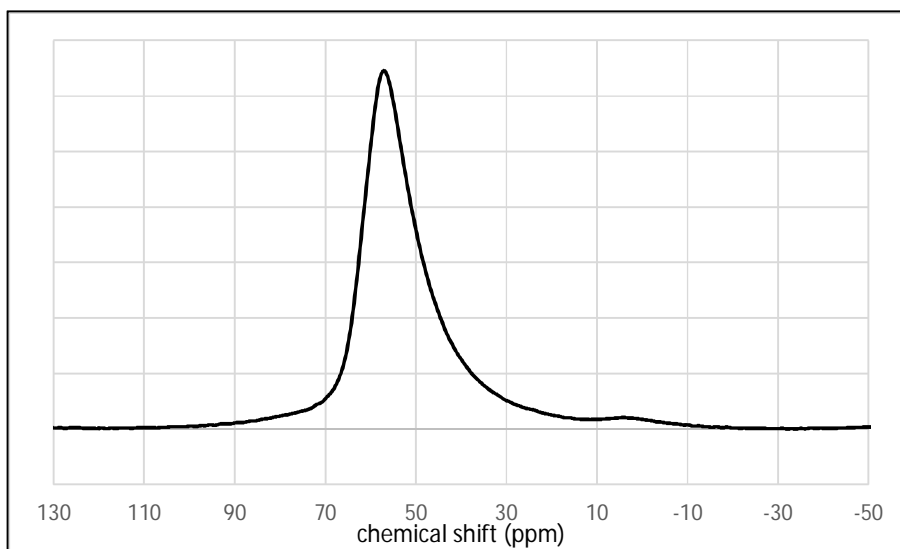


Figure 2.40. ^{27}Al NMR spectra of tuff-2.

The peaks corresponding to octa-coordinated Aluminum exhibited relatively low intensities. These peaks can be seen in figure 2.41 at -9, 0.8, 9 and 20 ppm. The peak at -35.5 ppm, which is definite indication of penta-coordinated Aluminum sites, showed higher intensity than octa-coordinated units. Distorted tetrahedral Aluminum species are possibly present in the sample contributing intensity to the peaks at 43 and 49 ppm. Therefore the two peaks at 43 and 49 ppm were both assigned generally to penta-coordinated and distorted tetra-coordinated Aluminum units.

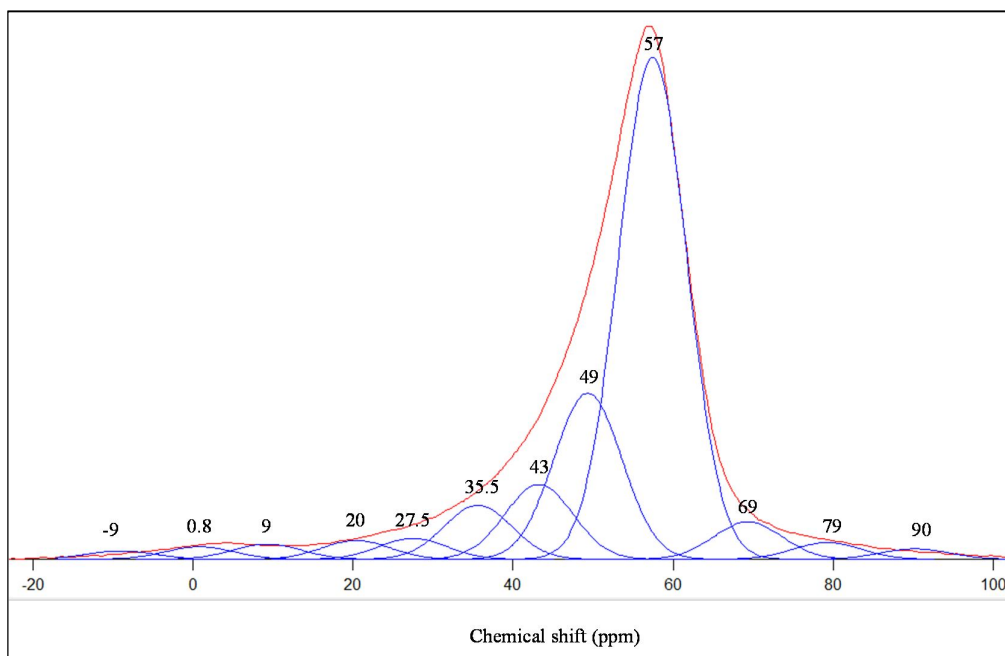


Figure 2.41. . Deconvolution of peaks in ^{27}Al NMR spectrogram of tuff-2.

The most intense peak appeared at 57 ppm being originated from tetrahedral Aluminum species. Tetrahedral Aluminum also created some low-intensity peaks between 60 and 100 ppm. All the peak assignments boil down to the conclusion that the predominant Aluminum species in tuff-2 sample is tetrahedral framework Aluminum, while extra-framework Aluminum (Al_V and Al_{VI}) are also present in its constituting phases.

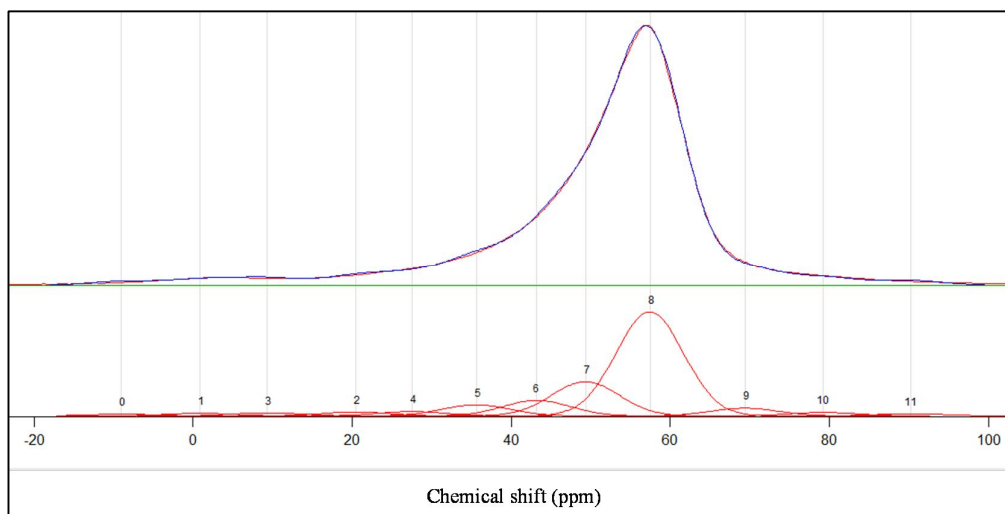


Figure 2.42. Experimental vs. simulated ^{27}Al NMR spectrogram of tuff-2.

2.5.8 ^{29}Si NMR spectroscopy of anhydrous WPC

Two peak containing chemical shift ranges between ca. -60 to ca. -80 ppm and between ca. -90 and ca. -126 ppm are observed in the ^{29}Si NMR of anhydrous WPC (shown in Figure 2.43). Deconvoluted peaks in the former range (range-1) are presented in Figure 2.44. The origin of the peaks in the latter range (range-2) will be discussed in the present section; for this purpose the XRD data will also be used to help deciphering the observed resonance peaks.

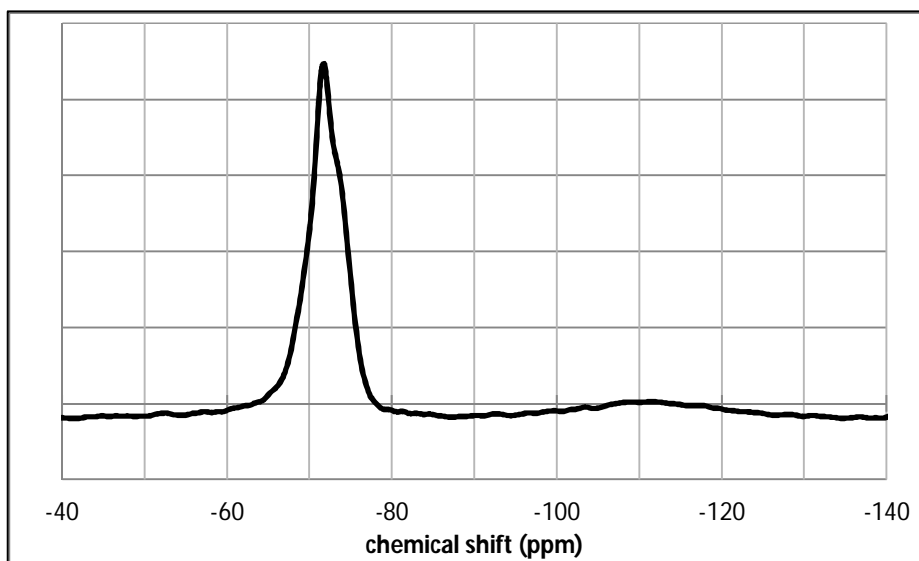


Figure 2.43. ^{29}Si NMR spectra of anhydrous WPC.

According to the silicate species chemical shift ranges presented in Table 2.5, all the peaks in the range-1 lie under the chemical shift range of Q^0 units. However, each of the four deconvoluted peaks is likely originating from a particular phase within WPC. Belite shows a single narrow ^{29}Si resonance peak at round -71.5; while, on the other hand, the ^{29}Si resonance peaks associated with Alite phase are constituted of several overlapping peaks (nine peaks according to (Brunet et al. 2010)) of different mono-silicate species generated by distortion of SiO_4 tetrahedra due to incorporation of impurities (most probably Al^{3+} and Mg^{2+}) in the crystal structure. Here, two distinct peaks at -69.19 and -66.5 ppm were assigned to Alite phase. In addition there is a contribution from Alite to the peak at -71.7 ppm, although the resonance associate with Belite is the predominant contributor to this peak. Figure 2.45 illustrates the ^{29}Si NMR spectrogram of synthetic Alite and Belite (Brunet et al. 2010). Figure 2.45 indicates that there must be another Alite-induced peak in the proximity of -74 ppm (-73.5 to -74.5 ppm). There is, indeed, a peak observed in the obtained spectra in this expected range, i.e. -74.1 ppm. However we

cannot be sure that Alite is the only phase contributing to this peak. (A. V. Girao 2007) reported that γ -C₂S exhibits ²⁹Si resonance peak in the vicinity of -73.5 ppm. γ -C₂S, due to its inert nature also creates a peak in the NMR spectra of hydrated WPC with the same intensity as its peak in anhydrous WPC, in fact, the contribution of the γ -C₂S phase to the intensity of the peak at ca. -74.1 is the same before and after hydration. Therefore, regarding the ²⁹Si spectra of hydrated WPC in chapter 3, it was assumed that the major contributor to the peak at -74.1 is Alite, while the intensity of the peak has contributions from γ -C₂S as well.

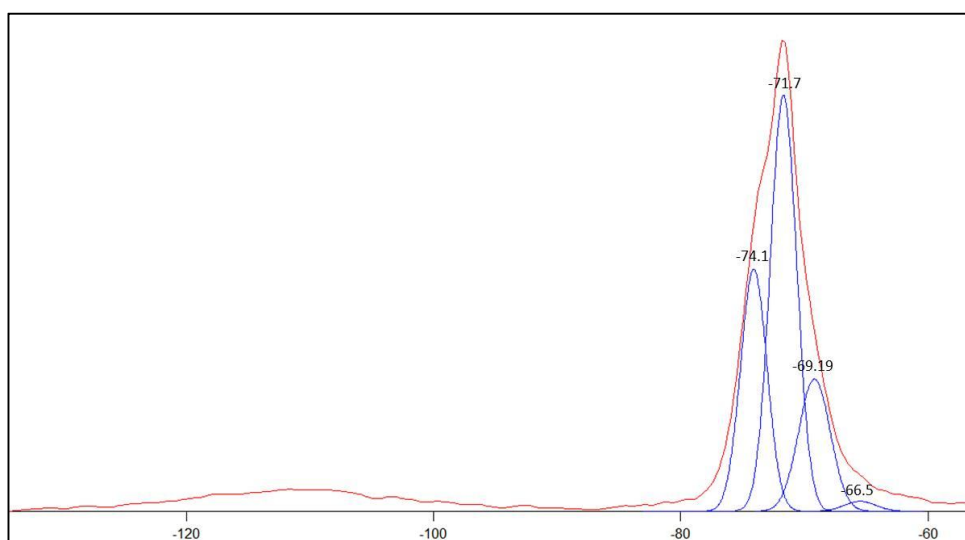


Figure 2.44. Deconvolution of peaks in ²⁹Si NMR spectrogram of anhydrous WPC in range-1.

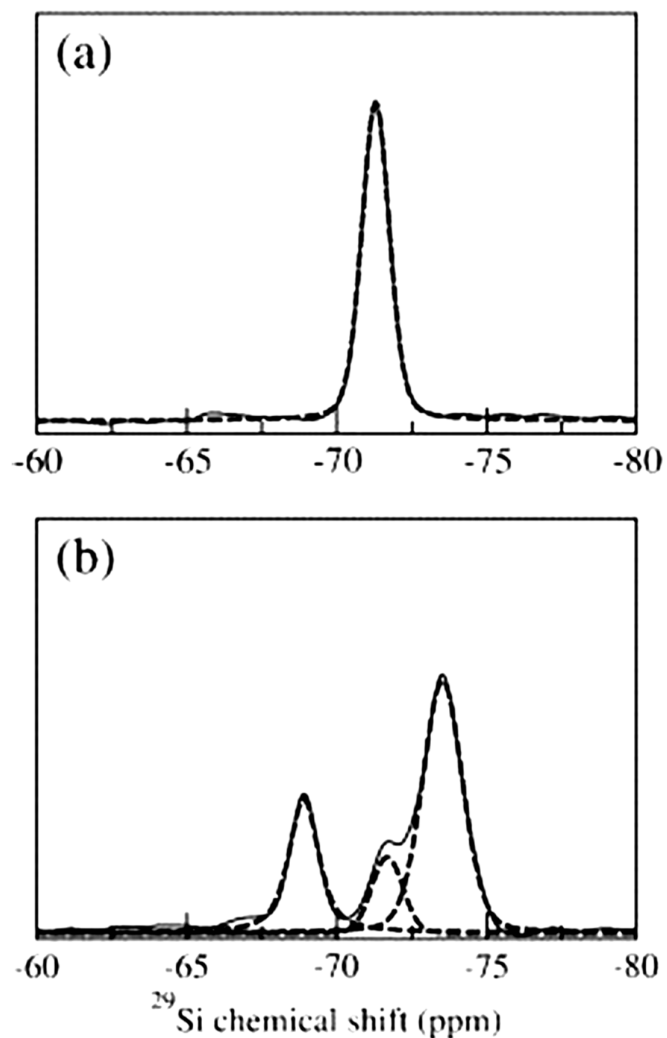


Figure 2.45. ^{29}Si NMR spectra of synthetic Belite (a) and Alite (b) (Brunet et al. 2010).

The very broad and low-intensity peak between -90 and -126 ppm indicates the presence of a set of peaks all of which are in the chemical shift range of Q^3 and Q^4 species. However, these are not entities normally found in PC and/or WPC. (Shtepenko et al. 2006) suggested that upon carbonation of PC, Q^0 species in C_3S (Alite) and C_2S (Belite) can further polymerize and transform into Q^3 and Q^4 units

with different degrees of Aluminum substitution for Silicon. The observation of these peaks and their respective attribution are in agreement with the XRD and XRF analyses of anhydrous WPC and also the XRD analysis of hydrated WPC. The identified Q³ and Q⁴ species are believed to be associated with the carboaluminate phases which are products of WPC carbonation. In addition, the adsorption of moisture by the carbonated WPC can result in generation of small amounts of so-called Calcium hemi-carboaluminate (at early stages) and Calcium mono-carboaluminate (at later stages) phases (Kemal Celik et al. 2013); these phases will be further discussed in sections 3.4.1 and 3.5.1.

2.5.9 ²⁷Al NMR spectroscopy of anhydrous WPC

Figure 2.46 shows the ²⁷Al NMR spectrogram for anhydrous WPC. The major peaks observed in the spectra are shown in Figure 2.47, however these are neither the exact and real appearance of the peaks nor the only peaks that appeared in the spectra. We showed the peaks in this form merely to show the approximate range of the principal resonance peaks. The peaks which were fitted to the spectra and the fitted trend line are presented in Figure 2.48, in this figure the blue line shows the fitted spectrogram while the red line shows the experimental spectrogram.

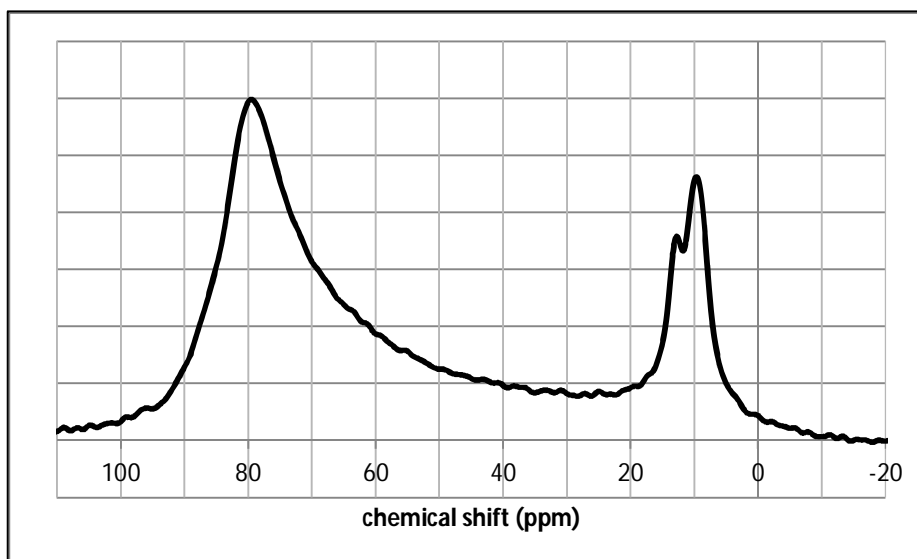


Figure 2.46. ^{27}Al NMR spectra of anhydrous WPC.

According to (Skibsted J., Jakobsen H.J. 1994) all the peaks between ca. 20 ppm and ca. 100 ppm can be attributed to a quadrupolar broadened Al_{IV} peak. However, according to (Mozgawa et al. 2002) the peaks between 30 ppm and 50 ppm can be attributed to both penta-coordinated Aluminum and distorted Al_{IV} . Therefore, we here consider all peaks between 50 ppm and 98 ppm (refer to Figure 2.4.9.3) as originating from tetra-coordinated Aluminum (Al_{IV}). Likewise, the small peaks between 17 ppm and 50 ppm (17 and 50 ppm excluded) are attributed to distorted Al_{IV} and penta-coordinated Aluminum. The peaks between 10 ppm and 17 ppm (including 10 and 17 ppm) are attributed to octahedral Aluminum sites.

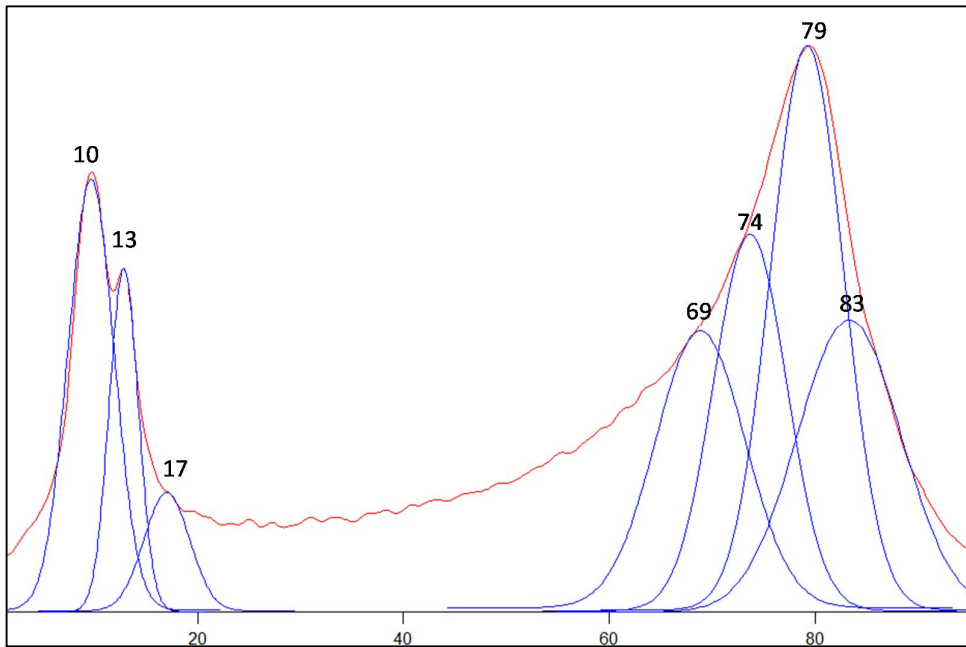


Figure 2.47. The principal peaks in ^{27}Al NMR spectra of WPC.

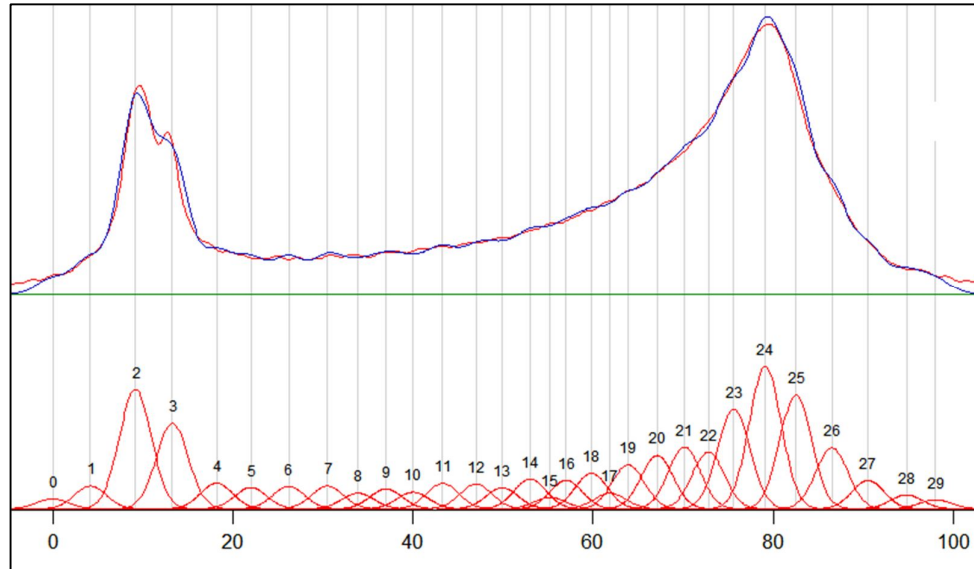


Figure 2.48. Experimental vs. simulated ^{27}Al NMR spectrogram of anhydrous WPC

2.6 Compressive strength performance tests

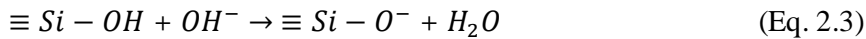
Compressive strength of a cementitious system can be used as a frame of reference to consider the effectiveness of the cementitious materials. In this research, two strength-based methods were used to assess the effect of the selected NPs on compressive strength of mortar samples.

Strength activity index (SAI) measures the compressive strength of mortar samples in which 20% of the PC is replaced with the pozzolan which is under study. Strength activity indices of the finely ground NPs were determined in accordance with ASTM C 311 standard to evaluate the performance of the selected NPs in practice. 7 and 28-day compressive strengths of mortars prepared with the blend of 80% ordinary PC (Limak ® CEM I 42.5 N) and 20% NP (by weight) were determined for each NP separately. Control samples were made by using neat OPC (Limak ® CEM I 42.5 N). The ratio of the strength of the blended cement sample to the strength of the same age PC sample is presented as Strength Activity Index.

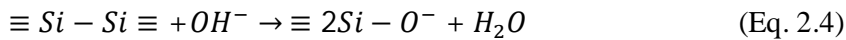
The strength performance of a cementitious system can be evaluated by following the evolution of compressive and flexural strengths. In this case, for high-volume-NP-PC (HVNP)-PC mortars 3-, 7-, 28- and 90-day compressive strengths were measured. The mortar mixtures consisted of 50 wt% NP and 50 wt% WPC; the water-to-binder ratio was kept as 0.5 in all mixtures. The sample preparation and measurements were performed according to ASTM C 348 and C-349 standards; the only inconformity to the standard was the addition of 4 wt. % polycarboxylate-based superplasticizer (Sika Viscocrete SF-18) to the mortar mixtures containing tuff-1 due to the significant increase of water demand by tuff-1 powder.

2.7 Effect of NPs on the expansion of mortar samples due to Alkali-Silica reaction (ASR)

The Alkali-Silica reaction is defined in (Page, C.L., Page 2007) as :” the reaction between alkali hydroxides in the pore solution of concrete and thermodynamically unstable Silica in certain aggregates”. When the alkali-silica reactive aggregate is exposed to the alkaline environment of the pore solution of the cementitious system (mortar or concrete), primarily the Silanol groups (Si-OH) in the aggregate structure are attacked by hydroxyl (OH⁻) functional groups in the system. The occurring reaction can be roughly expressed as equation 2.3.



Depending on the availability of hydroxyl groups in the system, more hydroxyls may penetrate in the structure (of siliceous aggregate) and also attack siloxane groups (Si-O-Si) (equation 2.4).



The negative charges on the Oxygen atoms are balanced by incorporation of Alkali cations (Na⁺ and K⁺) into the structure (Page, C.L., Page 2007). The resulting reaction product is an alkaline-silicate solution (called Alkali-Silica gel) which is capable of imbibing water and swelling. Hence, the Alkali-Silica gel expands upon

absorption of water. The exerted stress due to the expansion of the Alkali-Silica gel can damage the concrete or mortar and cause what is called Alkali-Silica cracking. SCMs have been proved to generally decrease or suppress the deleterious expansion caused by ASR. SCMs can suppress ASR either by reduction of the Alkali content in the pore solution or by binding the alkali cations more effectively. Reduction of the Pc content can result in decrease of the Alkali content in the binding materials. In addition the SCMs consume Calcium Hydroxide through pozzolanic reaction which results in less availability of hydroxyl groups. Pozzolanic cementitious materials can generate C-S-H phases with lower Calcium-to-silicon atomic ratio and consequently a less positive molecular structure; this improves the Alkali cation binding ability of the C-S-H structure and helps to suppress the ASR.

The capability of a mortar or concrete for being expanded due to ASR is one of the major durability factors. Therefore, the effects of the selected NPs on the alkali-silica-expansion potential of mortar samples containing reactive aggregates were investigated. For this purpose blends of 50%NP and 50%PC were used to make mortar samples with reactive aggregates. Highly reactive river aggregate containing opal was used to make the mortars. Then the potential expansion due to alkali-silica reaction was determined according to the ASTM C1260 standard. The only unconfomities to the standard was the application of white Portland cement (WPC) instead of ordinary Portland cement (OPC) and application of 4% superplasticizer in mortars which contained tuff-1 . To be able to relate the results of other applied methods to the ASR test results, WPC was used in lieu of OPC.

2.8 Heat evolution and setting time

2.8.1 Isothermal calorimetry

The structure and consequently the properties of the hardened cement paste depend on the temperature of hydration which itself is related to heat of hydration. In addition, the heat evolution is an indication of the speed of hydration reactions. Isothermal calorimetry is a technique which can be used to follow the evolution of heat during the hydration of neat and/or blended cement pastes. In this technique the generated heat during the hydration process is measured and recorded as a function of time. Figure 2.49 shows a typical calorimetry diagram of ordinary Portland cement. In order to monitor the heat evolution during the hydration of the neat WPC

and the NP-PC blended cements, *isothermal calorimetry* experiment was performed on the mixtures containing 0 (control samples) and 50% (by weight of cementing materials) natural pozzolan blended with white Portland cement. Cement pastes were cast at room temperature (23 °C) while the mixing water, the cement and mineral additives were kept at room temperature. Each samples used in calorimetry consisted of 5 grams of binder (50%C-50%NP in blended pastes and 100%WPC in control pastes) with a water-to-binder ratio of 0.5. The data measured were the rate of heat flow (in Watts), which after being normalized by the weight of the paste, was expressed in “*J/s/ (gram of paste)*”, and the cumulative heat expressed in Joules. In tuff-1 samples 4% (by weight of binder) superplasticizer (Sika Viscocrete SF-18) was applied to maintain uniformity between the samples in different experiments.

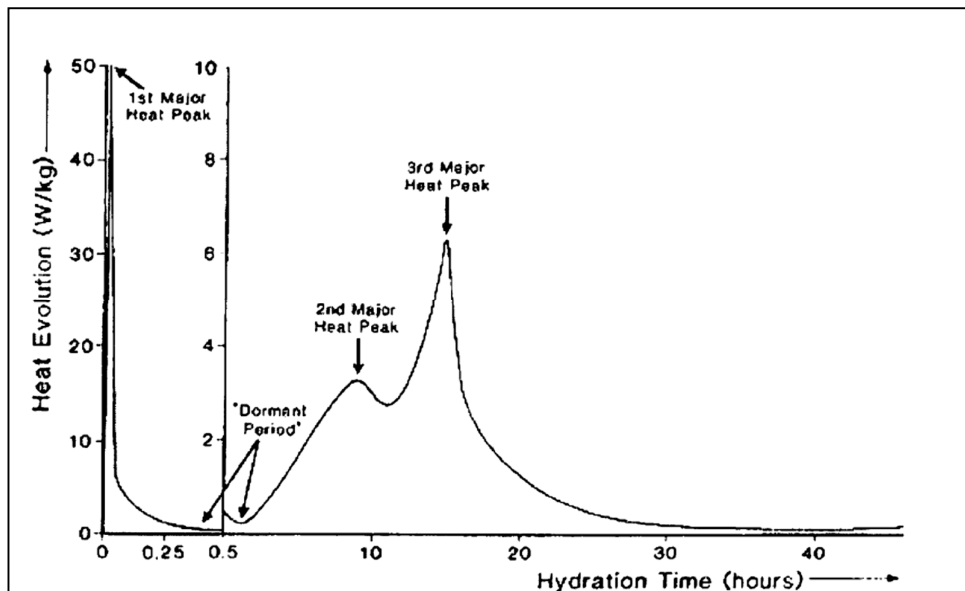


Figure 2.49. a typical isothermal calorimetry diagram of ordinary Portland cement (A. V. Girao 2007).

2.8.2 Setting time

Initial and final setting times of control and 50% (by weight of cementing materials) NP-containing pastes were measured according to ASTM C191-13 standard practice. For tuff-1 samples the setting times were measured by applying 4% superplasticizer (the same mentioned in section 2.8.1). Also in a separate practice the setting times of pastes were measured keeping the water-to-binder ratio at 0.5 and thus normal consistency was not attained in the pastes. The second set of setting time tests were also done according to ASTM C191-13 standard with the difference in water-to-binder ratio stated in the above.

CHAPTER 3

RESULTS AND DISCUSSION

3.1 Strength performance

3.1.1 Strength activity index (SAI)

The 7- and 28-day strength activity indices of the three NPs are given in Table 3.1. The results proved the conformity of the NPs to SAI specifications prescribed by ASTM C618 standard at both ages.

Table 3.1. Strength activity indices of the NPs.

Natural pozzolan	Strength activity index (%)	
	7-day	28-day
Tuff-1	78.00	98.00
Tuff-2	76.50	96.70
perlite	75.75	95.00

3.1.2 Compressive strengths of HVNP-PC mortars

Figure 3.1 gives the graphic presentation of the evolution of compressive strength over a 90-day course in mortar samples containing 50% (by weight of cementing materials) of NP. Strengths of control samples having WPC as the only cementing material are presented in the same figure for the purpose of comparison. The results corresponding to samples containing each of the studied NPs are given in separate curves. It can be seen in the figure that at 3-day age tuff-1 and perlite provided almost similar strength values, while tuff-2 had a higher 3-day compressive strength. The tuffaceous NPs provided a better compressive strength evolution than perlite. The 3-day strengths of tuff-2 samples were considerably higher than both other NPs, while tuff-1 samples showed a significantly higher strength development rate in the first 10 days of hydration. As a result of the more rapid strength development of tuff-1 samples, its curve met the curve of tuff-2 around the 15th day of hydration and showed higher strength values than tuff-1. However, the strengths of tuff-1 and tuff-2 samples after 10 days were very similar to each other.

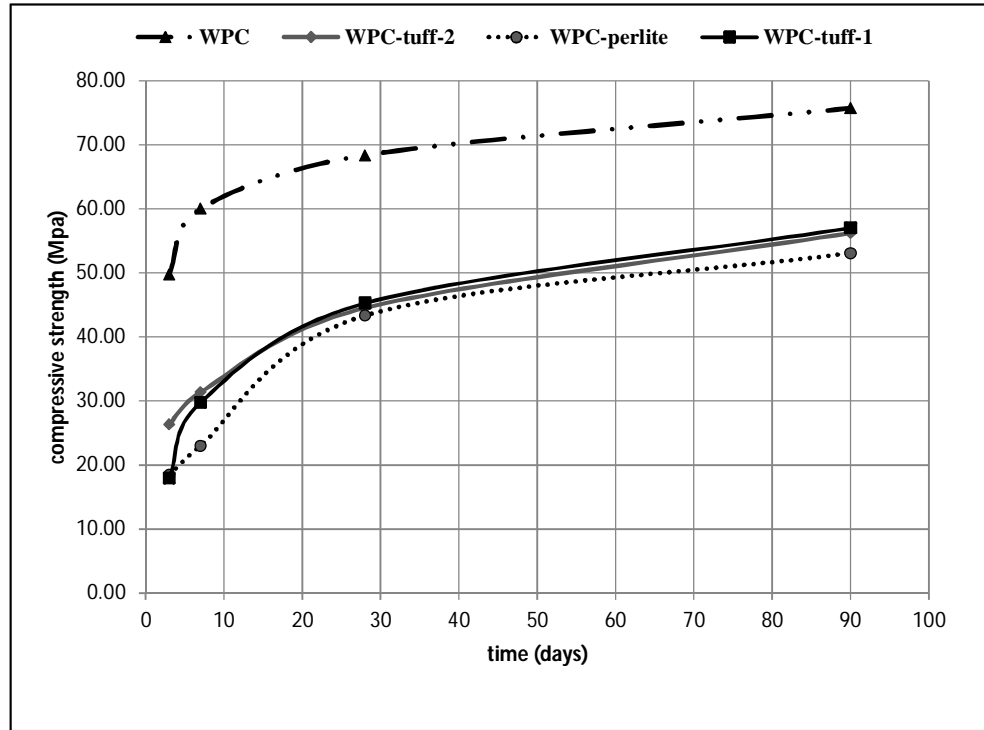


Figure 3.1. The graphic presentation of the results of compressive strength tests.

3.2 Heat evolution and setting time

3.2.1 Normal consistency pastes

Table 3.2 gives the initial and final setting times for the neat and blended cement pastes of normal consistency. The blended cement pastes called with the names of each NP, as explained in chapter 2, comprised WPC and the respective NP with 1:1 proportion. For each sample, the water demand to attain normal consistency is also presented in the table.

Table 3.2. Initial and final setting times of normal consistency paste samples.

	<i>WPC</i>	<i>perlite</i>	<i>Tuff-2</i>	<i>Tuff-1</i>
<i>Water-to-solid ratio for normal consistency</i>	0.3	0.29	0.32	0.39
<i>Initial setting time (min)</i>	96	117	117	84
<i>Final setting time (min)</i>	135	185	180	220

Tuff-1 paste had the shortest initial setting time while its final setting time was longer than all other pastes. This can be attributed to higher water-to-binder ratio and it is in agreement with the previous studies (Pane and Hansen 2005). Tuff-2 and perlite pastes gave very close results having exactly the same initial setting times while the final setting time of tuff-2 was slightly shorter than perlite.

3.2.2 Pastes with water-to-binder ratio of 0.5

To be able to establish a connection between the setting times and the heat evolution measurements, the setting times of the pastes with water-to-binder ratio of 0.5 were measured and presented in Table 3.3 along with their corresponding normalized cumulative heat of hydration. The heat values were normalized by the weight of pastes. It is seen in the table that WPC had the shortest final setting time, while the shortest initial setting time belonged to tuff-1. Interestingly, the WPC samples placed the third in heat evolution up to the times of both initial and final setting, the tuff-1 and perlite samples being first and second respectively. Among the NPs, tuff-1 samples had the shortest initial and final setting times. Tuff-2 samples generated the lowest amount of heat over the measured time period, whereas, their initial and final setting times were shorter than perlite samples. Perlite samples, despite generating high amounts of heat, had the longest initial and final setting times

than all paste samples. The explained order of setting times and heat evolutions are in agreement with (Pane and Hansen 2005) who stated that “higher heat of hydration does not necessarily mean higher degree of hydration”. It should be noted that the initial and final setting times of all pastes in the two sections 3.2.1 and 3.2.2 lie within the limits prescribed by ASTM C150 standard for Portland cement.

Table3.3. Setting times and their equivalent heat of hydration values of pastes having water-to-binder ratio of 0.5.

		WPC	perlite	Tuff-2	Tuff-1
Initial setting	Time (minutes)	215	266	235	146
	Equivalent heat (J/g)	32.93	35.85	28.32	39.10
Final setting	Time (minutes)	300	386	366	350
	Equivalent heat (J/g)	48.06	50.65	42.44	69.00

Figure 3.2 gives the curves of heat flow during the hydration of the pastes over a 3-day course (72h). In all pastes an initial high-heat flow stage was observed which can be attributed to the fast reaction of some highly soluble components in the PC. This stage is stopped shortly after the beginning of hydration by formation of a thin layer of hydration products which surround the cement particles. In the WPC curve, after the induction (dormant) period a fast growth was observed in the heat flow

which resulted in three consecutive peaks at about 5.5, 6.5 and 10.5 hours. These peaks can be attributed to the hydration of Alite, hydration of aluminous phases (generating Ettringite) and the onset of the hydration of Belite. The formation of C-S-H phase is believed to begin in this stage. In tuff-1 paste, higher heat flow during the induction period was observed. This heat flow in the time range believed to be the induction period is even higher than WPC and seems somehow anomalous. However, the isothermal calorimetry on the tuff-1 paste was performed in three different times with three paste samples on each attempt, and the same strange curve trend was observed in the results obtained from all attempts. In addition the induction period of tuff-1 paste was prolonged and the rate of the acceleration period (following the induction period) was increased. Interestingly, after the appearance of a sharp peak at about 5.5 hours the heat flow was decreased significantly to values lower than all neat and blended pastes after about 7.5 hours. In tuff-2 and perlite pastes the induction period was prolonged and the rate of acceleration period was reduced. The heat flow curves of tuff-2 and perlite pastes laid below the curve of WPC over the entire length of the measurement time.

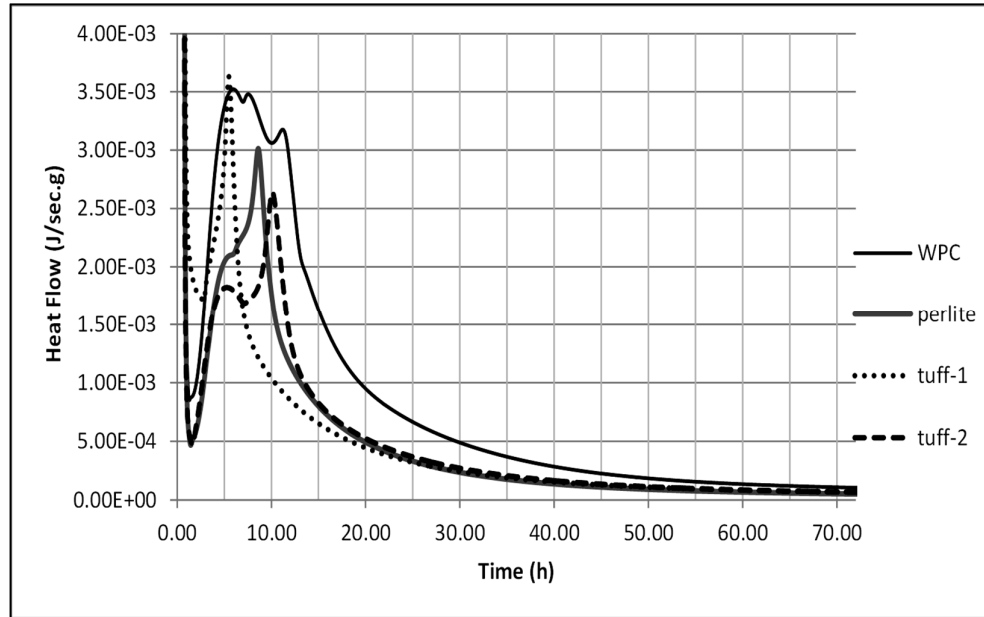


Figure 3.2. Normalized heat flow-time curves of neat and blended pastes with water-to-binder ratio of 0.5 over a 3-day course.

Figure 3.3 gives the cumulative heat generated during the hydration of the neat and blended pastes over a 10-day period. The heat values were normalized by the weight of pastes presenting the results in Joules per gram of paste. It can be seen in the figure that the tuff-1 paste generated higher heat than tuff-1 and perlite pastes over the entire time period. The tuff-1 sample generated higher heat than WPC up to about 4.7 hours. The heat generation during the hydration of perlite paste was higher than WPC up to 2.8 hours. Over the entire length of measurement, the heat generated by the hydration of the tuff-2 paste was lower than WPC and tuff-1 pastes. While, on the other hand, the heat generation associated with tuff-2 paste was less than the perlite paste up to about 140 hours when the curves of the two pastes meet; after this point, the tuff-2 curve laid over the curve of perlite paste. At the end of 10 days, the total heat generated by the hydration of WPC, tuff-1, tuff-2 and perlite pastes were respectively 261, 163, 159 and 156 Joules per gram of paste.

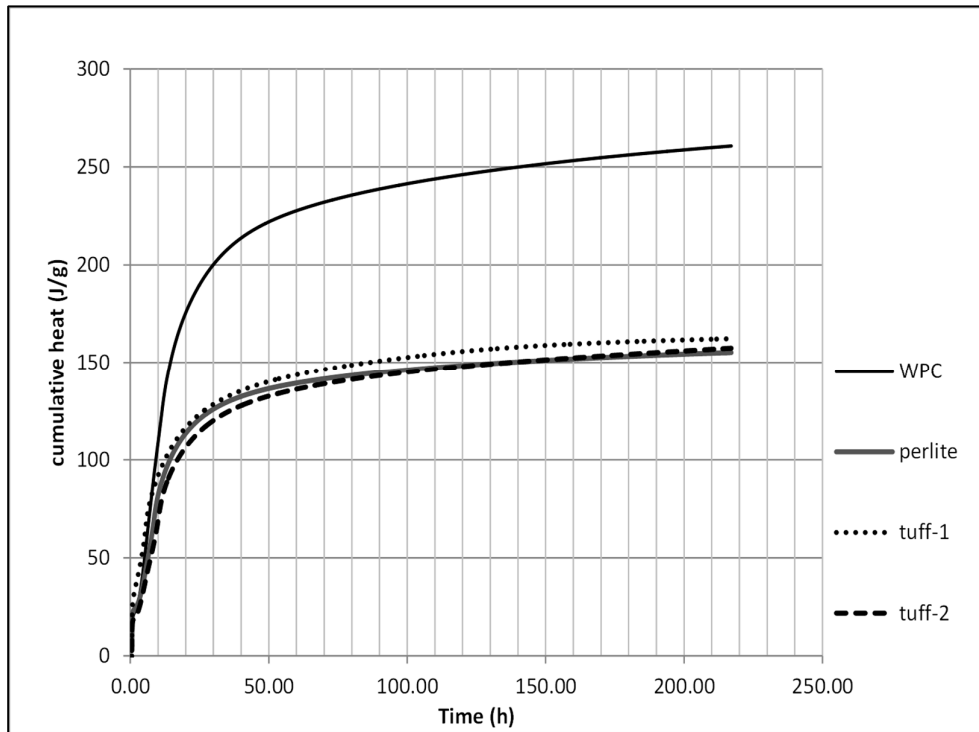


Figure 3.3. The curves of normalized cumulative heat of hydration of the neat and blended pastes with water-to-binder ratio of 0.5 over a 10-day course.

3.3 Alkali-silica reactivity

Figure 3.4 gives the graphic presentation of the ASR expansion of prismatic mortar samples over a 14-day course. As it can be seen in the graph, all three NPs have affected the expansion potential significantly resulting in considerable decrease of the length percentage by which the mortars expanded. Whilst the effect of tuff-2 and perlite were very similar, the samples containing tuff-1 showed a relatively better performance than tuff-2 and perlite samples. Taking the expansion of WPC samples as reference, tuff-1, tuff-2 and perlite samples respectively exhibited 86.5, 78.8 and 81.2 percent less expansion in 14 days. Perlite (Bektas, Turanli, and Monteiro 2005) and zeolite-rich tuffs (similar to tuff-1) (Quanlin and Naiqian 2005) have been proved to have desirable effect on ASR expansion. (Naiqian and Tingyu

1998) postulated that natural zeolites can suppress the ASR expansion by reducing the concentration of alkaline ions in the pore solution if the cementitious system of the cementitious system through multiple mechanisms which include pozzolanic reaction, adsorption and ion exchange. However, the mechanism by which perlite reduces the ASR expansion has not been individually investigated. For perlite and tuff-2, the mechanisms generally stated in the above can be roughly assumed to be responsible of their effect on ASR expansion.

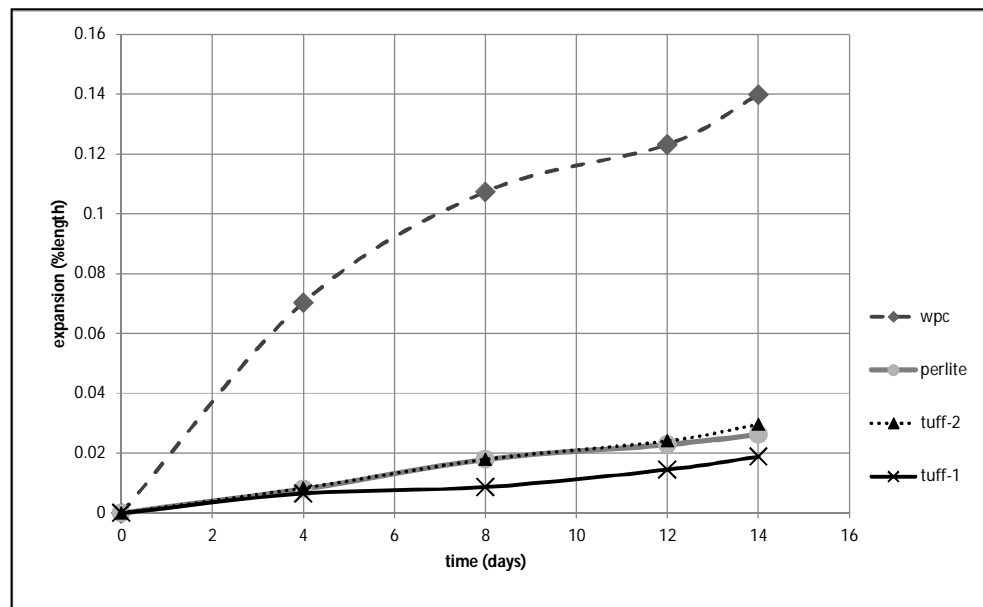


Figure 3.4. The graphic presentation of the results of ASR tests.

3.4 XRD analysis of hydrated WPC and hydrated pastes

In this chapter first the XRD pattern of HWPC will be analyzed in detail, then following the discussions made on the XRD patterns of the anhydrous materials (WPC and NPs) and the discussions presented in section 3.4.1, the XRD patterns of tuff-1, tuff-2 and perlite will be analyzed. Therefore, in the analyses associated with

htuff-1, perlite and htuff-2 the detailed process of peak assignment is not explained; rather, identified phases are directly introduced with the least explanations possible and the peaks corresponding to each phase are labeled in the XRD patterns. More detailed explanations will be provided when there is any need to clarify the back scene of the assignment of a particular peak.

3.4.1 HWPC

Figure 3.5 shows the XRD pattern of the WPC compared with the simulated XRD patterns (“JCPDS PDF-2 Database” 2004) of the identified phases. As seen in the Figure 3.5 the peak at $2\theta=11.71^\circ$ (marked by star) does not conform to any of the identified patterns. This peak corresponds to a crystal structure with $d\text{-spacing}=7.56 \text{ \AA}$ (“JCPDS PDF-2 Database” 2004). (Ipavec et al. 2011) reported that during the hydration of Calcite-containing Portland cements, CaCO_3 tends to react with C_3A and C_4AF to form hemi- and mono-carboaluminates. Calcium hemi-carboaluminate phase forms as early as the first day of hydration, then after three days of hydration starts to convert into Calcium mono-carboaluminate until about 28th day of hydration when the Calcium hemi-carboaluminate is almost completely converted into Calcium mono-carboaluminate phase (K. Celik et al. 2014; Ipavec et al. 2011). As it was previously mentioned in section 2.5.8, (Shtepenko et al. 2006), from the investigation of the carbonation of OPC and C_2S , reported that the exposure of anhydrous OPC and C_2S can also result in generation of carbonated products with higher degrees of silicate polymerization than the hydration products of OPC or C_2S . This carbonation product in anhydrous WPC was observed in the XRD analysis in section 2.3 and the NMR analysis in section 2.5. Following the above discussion, the $d\text{-spacing}$ of the unidentified phase was compared with the mono-carboaluminate and hemi-carboaluminate phases which can potentially be generated in the hydration of PC. Consequently, the carboaluminate substance in the HWPC was identified as Calcium mono-carboaluminate with the chemical formula $[\text{3CaO} \cdot \text{Al}_2\text{O}_3 \cdot \text{CaCO}_3 \cdot 11\text{H}_2\text{O}]$ that forms a crystal structure with $d\text{-spacing}(\text{layer thickness})=7.56 \text{ \AA}$ (Moon et al. 2012).

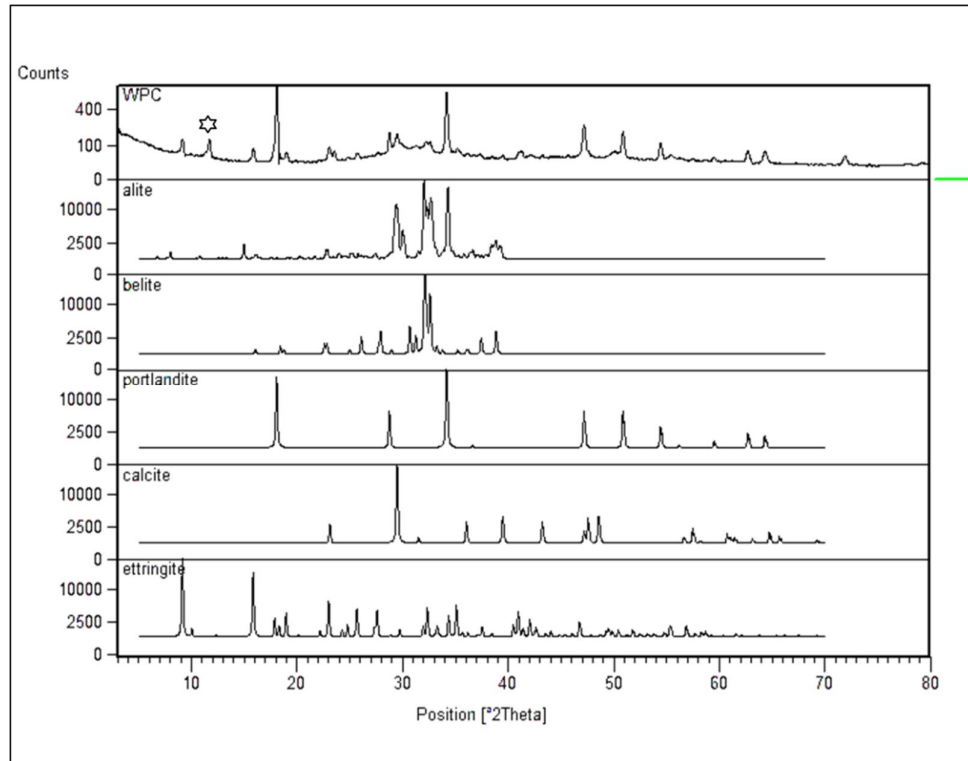


Figure 3.5. The XRD patterns of HWPC and identified phases.

To conclude this section the crystalline phases identified in HWPC are listed in the following:

- Anhydrous tricalcium silicate (C_3S) and dicalcium silicate (C_2S) originating from unreacted WPC. These phases are referred as Alite and Belite, respectively, in Figure 3.1.
- $Ca(OH)_2$ (Portlandite) that is a result of WPC hydration.
- $CaCO_3$ (Calcite).
- Ettringite ($Ca_6Al_2(SO_4)_3(OH)_{12} \cdot 26H_2O$).
- Calcium mono-carboaluminate ($3CaO \cdot Al_2O_3 \cdot CaCO_3 \cdot 11H_2O$).

Figure 3.6 shows the peaks corresponding to each of these phases in the XRD pattern of HWPC. The labels are E: Ettringite, M: Calcium mono-carboaluminate, P: Portlandite, C: Calcite, B: Belite and A: Alite.

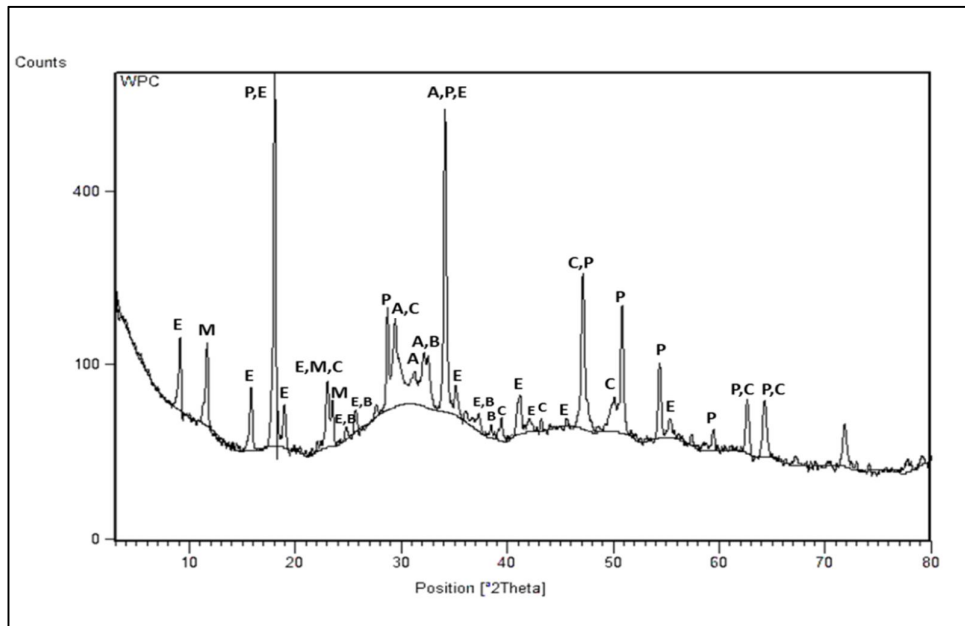


Figure 3.6. Main peaks of the identified phases in the XRD pattern of HWPC.

3.4.2 Htuff-1

The crystalline phases identified in the Htuff-1 pastes are presented in the following along with their respective labels in Figure 3.7. The labels are presented in the brackets:

- *Unhydrated clinker phases (alite and belite) [CL]*

- *Calcite* (CaCO_3) [CA]
- *Portlandite* (Ca(OH)_2) [P]
- *Ettringite* (calcium sulfo-aluminate hydrate) [E]
- *Quartz* (SiO_2) [Q]
- *Heulandite-II* [H]
- Calcium mono-carboaluminate ($3\text{CaO} \cdot \text{Al}_2\text{O}_3 \cdot \text{CaCO}_3 \cdot 11\text{H}_2\text{O}$) [M]

The main points found by XRD analysis of the hydrated paste are related to Ettringite, tetracalcium aluminate hydrate, Calcite, Portlandite and Heulandite phases. (Burak Uzal 2007) studied the hydrated pastes containing 55% of the same NP used in this study in a 28-day period. He reported that the amount of Ettringite experienced a reduction until the 28th day of hydration when the XRD peaks corresponding to Ettringite showed very low intensities. However, in the XRD pattern obtained at 7th month of hydration in this research, quite high intensity of the Ettringite peaks implies the presence of considerable amounts of Ettringite in the hydration products. Hence, Ettringite is possibly regenerated in the later ages of hydration. In addition, (Burak Uzal 2007) detected the tetra calcium aluminate hydrate ($4\text{CaO} \cdot \text{Al}_2\text{O}_3 \cdot 13\text{H}_2\text{O}$) phase as a product of pozzolanic activity; on the contrary, in our study, this phase was not detected by XRD analysis. Therefore it can be assumed that the tetra calcium aluminate hydrate was either not produced in the course of hydration or it was decomposed and converted to other phases in hydration ages later than 28 days. The Calcite phase is likely to be generated as a result of carbonation of either WPC or the NP. The very low amount of Portlandite in the paste (indicated by low-intensity peaks) is an indication of high pozzolanic activity of the NP which consumes the Ca(OH)_2 produced through hydration reactions of the WPC; this is in good agreement with the low intensity of Heulandite-II peaks showing that small amounts of NP has remained unreacted.

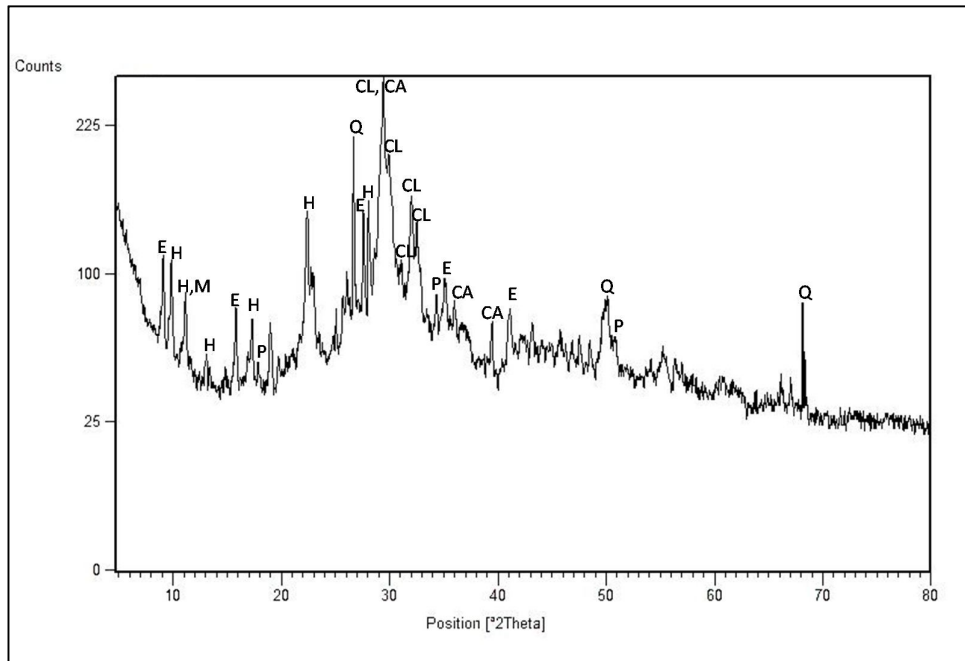


Figure 3.7. Main peaks of the identified phases in the XRD pattern of Htuff-1.

3.4.3 Hperlite

Figure 3.8 shows the XRD pattern of Hperlite. The crystalline phases identified in the Hperlite pastes are:

- *Unhydrated clinker phases (alite and belite) [CL]*
- *Calcite (CaCO₃) [CA]*
- *Portlandite (Ca(OH)₂) [P]*
- *Ettringite (calcium sulfo-aluminate hydrate) [E]*
- *Quartz (SiO₂) [Q]*
- *Biotite [B]*
- *Albite [A]*
- *Calcium mono-carboaluminate (3CaO . Al₂O₃ . CaCO₃ . 11H₂O) [M]*
(discussed in section 3.4.1)

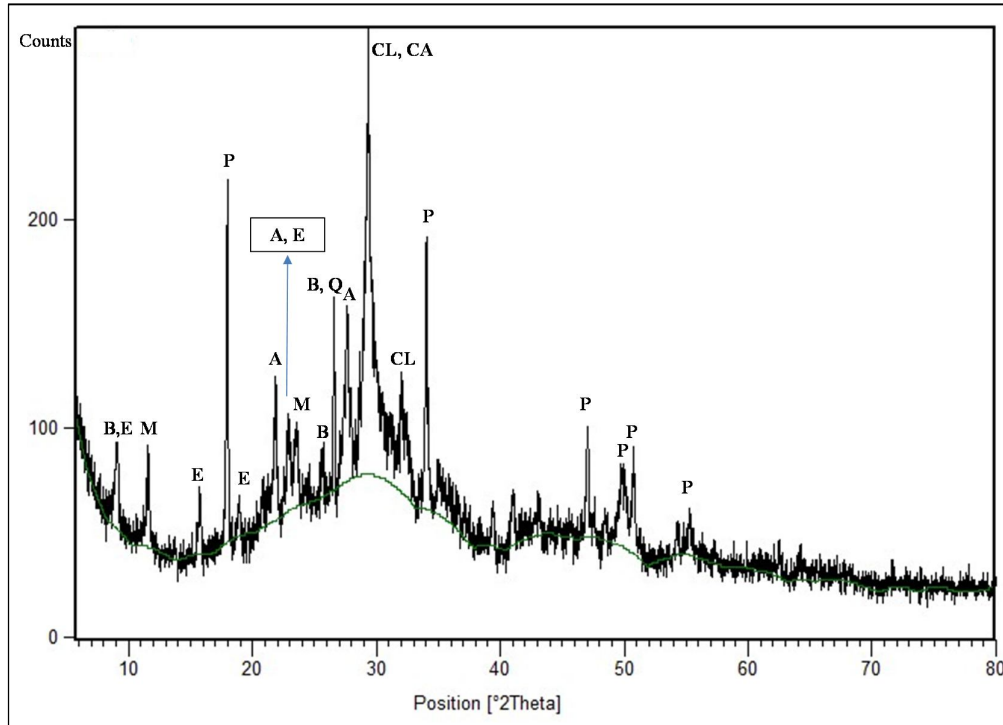


Figure 3.8. Main peaks of the identified phases in the XRD pattern of Hperlite.

3.4.4 Htuff-2

Figure 3.9 gives the XRD pattern of tuff-2. The crystalline phases identified in the Htuff-2 pastes are presented in the following along with their respective labels (in Figure 3.9). The labels are presented in the brackets:

- *Unhydrated clinker phases (alite and belite) [CL]*
- *Calcite (CaCO₃) [CA]*
- *Portlandite (Ca(OH)₂) [P]*
- *Ettringite (calcium sulfo-aluminate hydrate) [E]*
- *Quartz (SiO₂) [Q]*
- *Anorthoclase [A]*

- *Muscovite* [Mu]
- Calcium mono-carboaluminate ($3\text{CaO} \cdot \text{Al}_2\text{O}_3 \cdot \text{CaCO}_3 \cdot 11\text{H}_2\text{O}$) [M]. This phase was discussed in section 3.4.1.

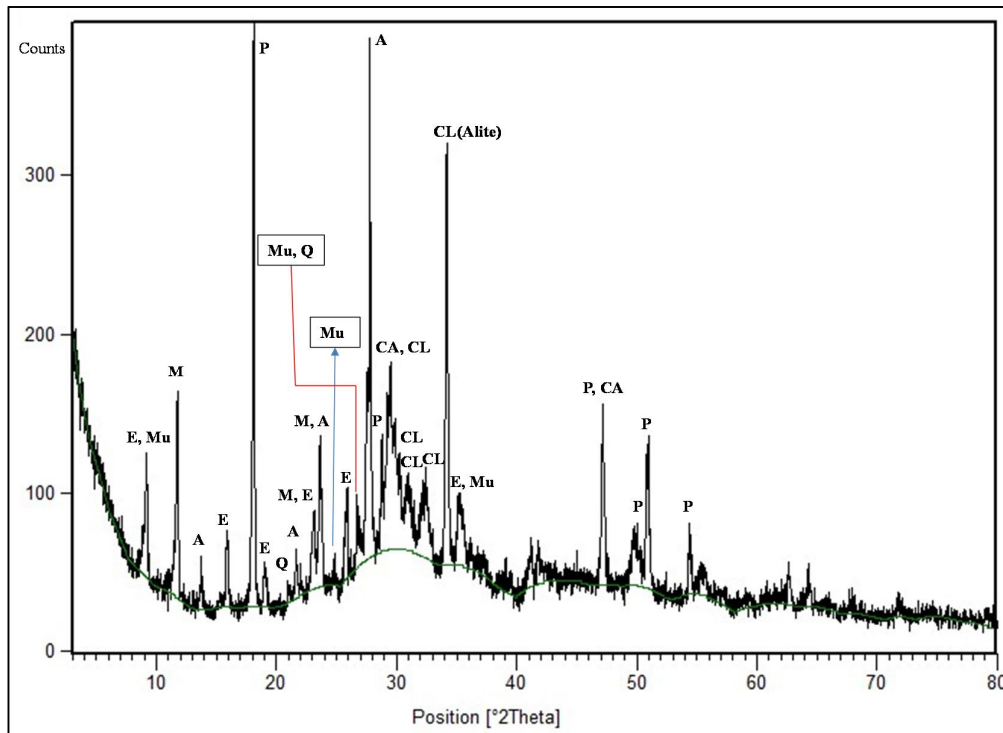


Figure 3.9. Main peaks of the identified phases in the XRD pattern of Htuff-2.

3.5 NMR spectroscopy of pastes

3.5.1 ^{29}Si NMR study of HWPC

In Figure 3.10, the ^{29}Si NMR spectrogram of HWPC is presented. A hump is observed between ca. -95 and ca. -126 ppm. As already mentioned in section 2.5.8, this hump contains a set of peaks in the chemical shift range of Q^3 and Q^4 originating from the so-called Calcium carboaluminate phases. The Q^3 and Q^4 species detected in the ^{29}Si NMR spectra of WPC originate from both carbonated anhydrous WPC and the mono-carboaluminate ($3\text{CaO} \cdot \text{Al}_2\text{O}_3 \cdot \text{CaCO}_3 \cdot 11\text{H}_2\text{O}$) phase generated during hydration of calcite-containing PC (as is the case with the WPC used in this research).

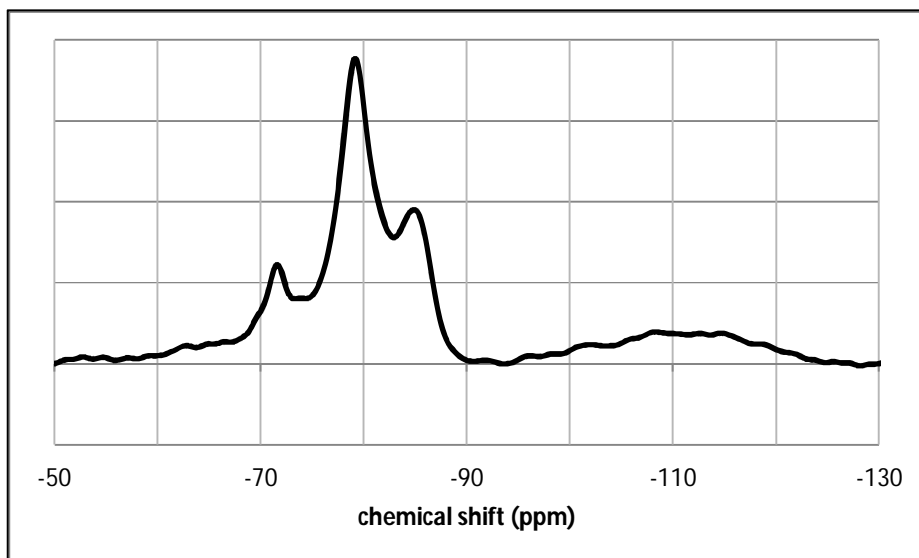


Figure 3.10. ^{29}Si NMR spectra of hydrated WPC.

The peak deconvolution for this spectrogram was very problematic due to the broadening of some peaks and severe peak overlapping, the best fitting set of peaks and their respective simulated curve are presented in figures 3.11 and 3.12 respectively. The deconvolution of peaks lead to detection of nine peaks within the chemical shift range of Q^0 , Q^1 and Q^2 species (Figure 3.11). The peaks at chemical shift values greater (i.e. less negative) than -79 ppm are attributed to C_3S and C_2S phases in unreacted WPC. The peaks at -62.9, -66.5, -69 and -75.59 ppm are attributed to unreacted C_3S . It is worth mentioning again that the chemical shifts of the resonances associated with C_3S may experience variations due to the incorporation of impurities such as Al^{3+} and Mg^{3+} , hence, the position of C_3S -induced resonances can be slightly different between anhydrous and hydrated WPC. The resonance of unreacted $\beta.C_2S$ can be seen in -71.5 ppm; regarding the higher reactivity of C_3S in comparison with C_2S , this resonance has a slight contribution from unreacted C_3S phase. It is somehow complicated to assign the peak appearing in the vicinity of -73 ppm to a distinct species. As discussed in section 2.5.8, contributions from C_3S and $\gamma.C_2S$ may create resonance peak in the range of -73 to -74 ppm. Here, this peak at -73 ppm was assigned to very small amount of inert $\gamma.C_2S$ and the negligible amount of C_3S that was remained unreacted. The peaks at -79.09, -82 and -85.2 ppm were assigned respectively to Q^1 (end-chain), Q^2 (1Al) and Q^2 (middle-chain) species present in the C-S-H phase.

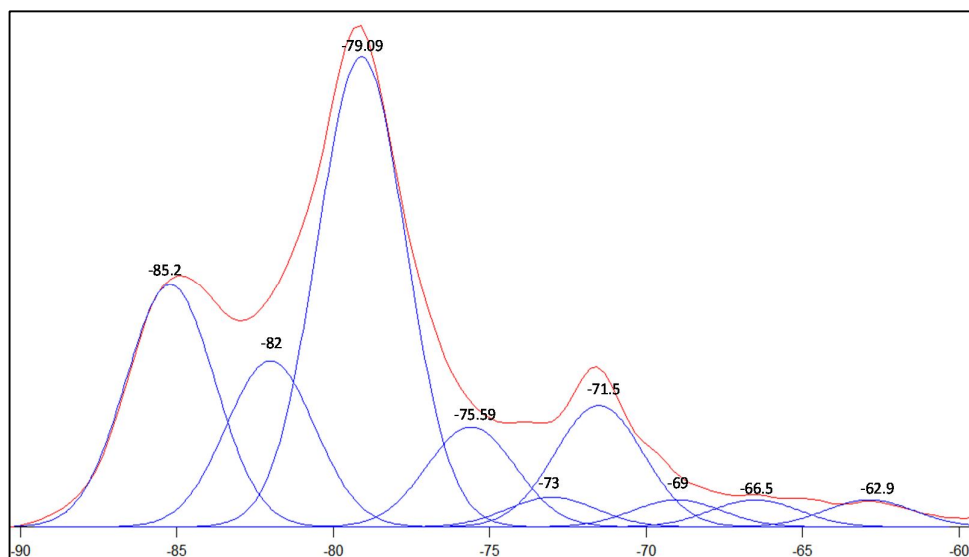


Figure 3.11. The principal peaks in ^{29}Si NMR spectra of HWPC.

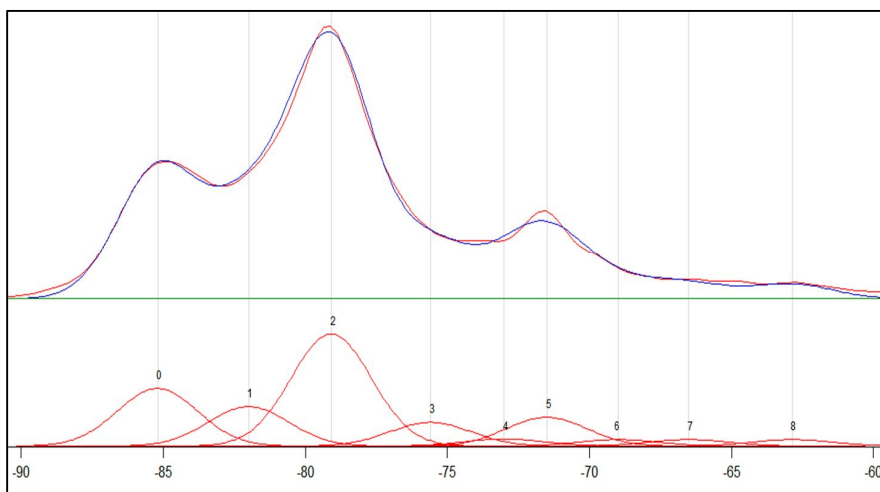


Figure 3.12. Experimental vs. simulated ^{29}Si NMR spectrogram of HWPC.

As seen in figure 3.13 the Q^0 silicate species in the anhydrous WPC was considerably consumed during the hydration process and lead to the formation of Q^1 and Q^2 aluminosilicate units.

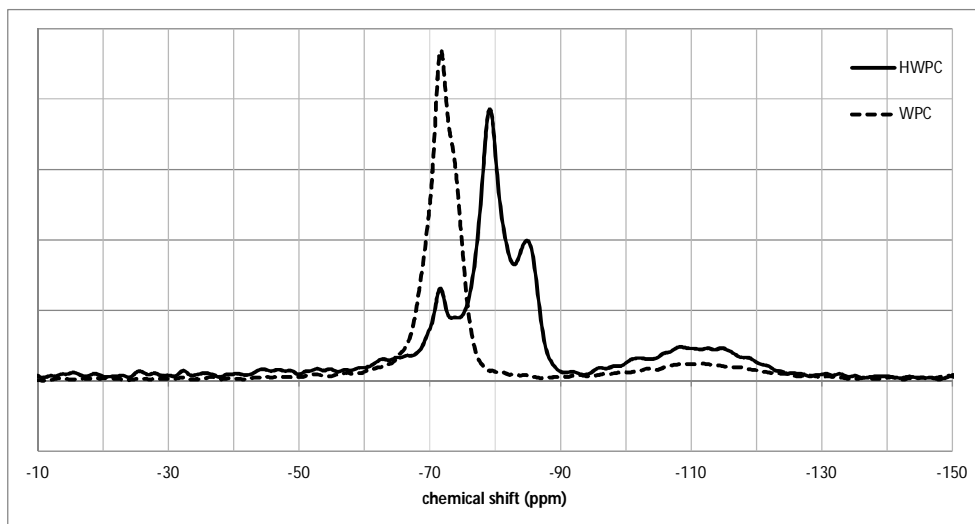


Figure 3.13. Comparative presentation of ^{29}Si NMR spectra of HWPC, and anhydrous WPC

3.5.2 ^{27}Al NMR study of HWPC

In the ^{27}Al NMR spectra of HWPC (Figure 3.14) the principal peaks appeared in the chemical shift range associated with octa-coordinated Aluminum (ca. -15 to ca. +20 ppm, Figure 3.15), while, in the chemical shift ranges of Al_V and Al_{IV} broadened and/or low-intensity peaks were observed. The observed configuration of ^{27}Al resonance peaks and its comparison with section 2.5.3, indicates that the framework Aluminum species, within anhydrous WPC, were significantly decomposed and consumed during hydration which is why the peaks in the chemical shift range of 30 to 100 ppm were considerably reduced in intensity or even completely disappeared.

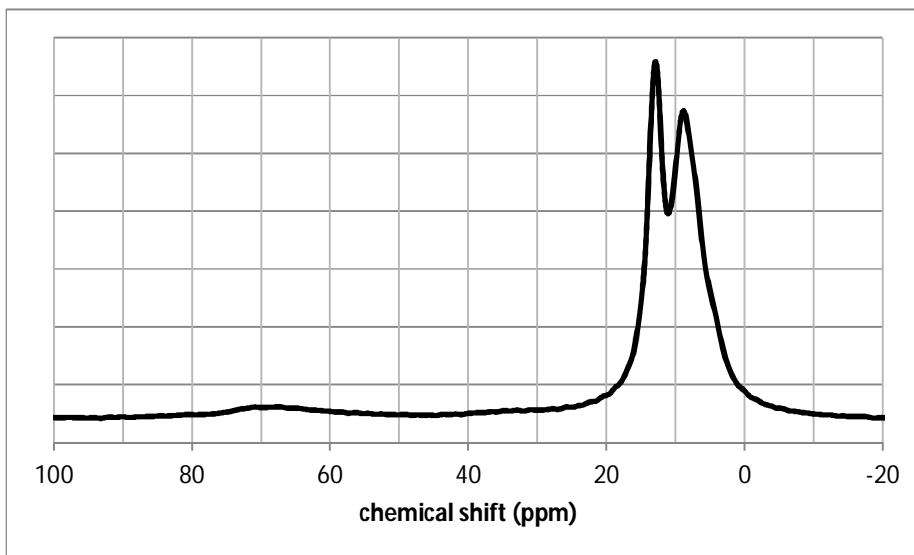


Figure 3.14. ^{27}Al NMR spectra of hydrated WPC.

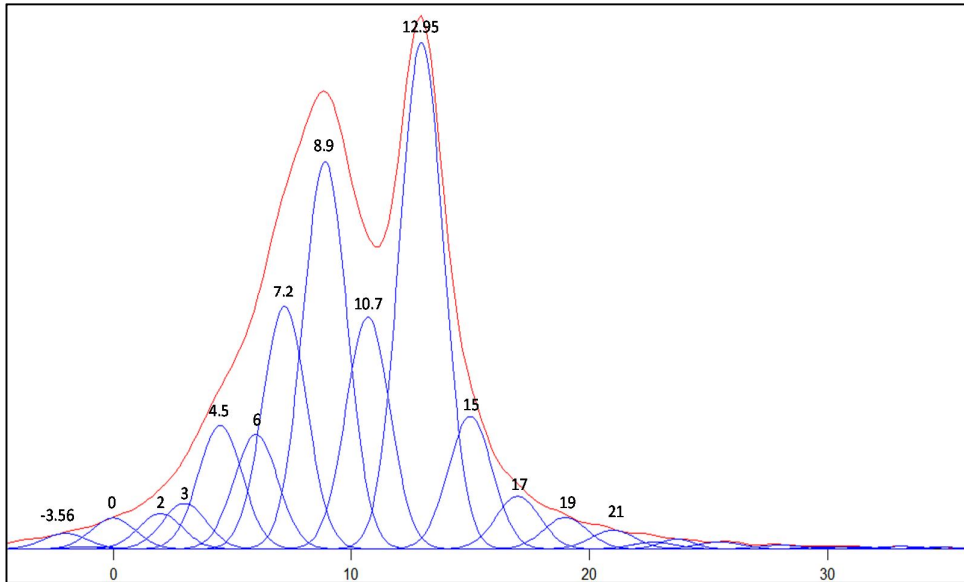


Figure 3.15. The principal peaks in ^{27}Al NMR spectra of HWPC.

The octa-coordinated Aluminum species showing peaks at around 20 ppm can be attributed to amorphous aluminate units within C_2S phase (Smith et al. 2011). Octa-coordinated Aluminum present in Ettringite (Smith et al. 2011) and probably some other Calcium aluminate hydrate phases (Faucon et al. 1999) such as the Calcium mono-carboaluminate, likely cause the peaks in the chemical shift range of 10 to 13 ppm. The peaks at 6 and 7.2 ppm are attributed to octa-coordinated Aluminum in the C-S-H phase (Smith et al. 2011). The ^{27}Al resonance associated with various orders of octa-coordinated Aluminum in the Calcium aluminate mono-sulfate (AFm) phase tend to create ^{27}Al resonance peaks between 3 and 9 ppm (Rawal and Smith 2010); therefore, the peaks at -3, -4.5, -6, -7.2 and -8.9 likely have contributions from these species. The peaks in the chemical shift range of -4 to +3 ppm are possibly associated with Calcium aluminate hydrate phases (Faucon et al. 1999; Smith et al. 2011).

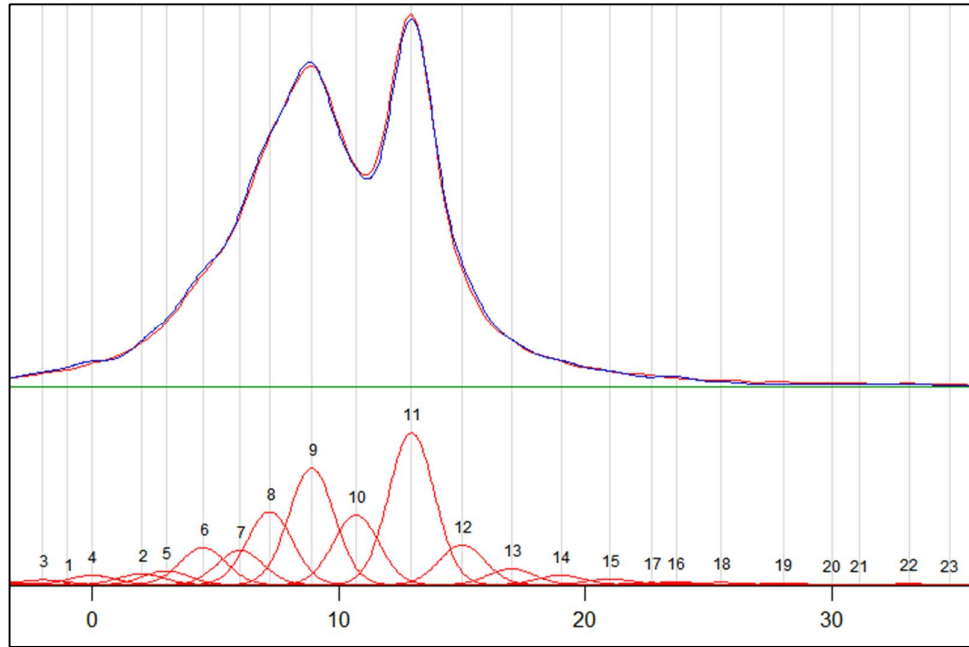


Figure 3.16. Experimental vs. simulated ^{27}Al NMR spectrogram of HWPC.

3.5.3 ^{29}Si NMR study of Htuff-1

The ^{29}Si NMR spectrogram of Htuff-1 (hydrated 50% WPC-50% tuff-1 blend) is presented in Figure 3.17 and the deconvoluted peaks are shown in Figure 3.18. Following the explanations presented in the previous sections and chapter 2 on the assignment of ^{29}Si NMR peaks the obtained spectra were interpreted as follows. The peak at -71.5 ppm is attributed to unreacted $\beta\text{-C}_2\text{S}$ and C_3S . It is seen in Figure 3.18 that there are fewer C_3S -induced peaks in the obtained spectra, this is in agreement with the amount of WPC used in the mixture which is 50% less than the neat WPC paste. The peak at -74 ppm is attributed to C_3S and $\gamma\text{-C}_2\text{S}$ phases. Q^0 species in C_3S also gave a resonance peak at -76 ppm. The peaks at -79.6, -81.6, -83.4 and -85.2 ppm are attributed to silicate and aluminosilicate species within the C-S-H phase and they are assigned to Q^1 , $\text{Q}^2(1\text{Al})$, $\text{Q}^2(1\text{Al})$ and Q^2 (middle chain) species respectively. It should be highlighted that two peaks at -81.6 and -83.4 are

attributed to $Q^2(1Al)$ units; this may be caused either by peak broadening (i.e. one broad peak instead of two narrower peaks was present) or by variation of chemical shift caused by factors such as molecular geometry, ion incorporation, etc.

The resonance peaks in the chemical shift range of ca. -87 to ca. -103 ppm are very difficult to be attributed to exact phases solely by the use of ^{29}Si and ^{27}Al NMR spectroscopy. The trickiest among them is the peak located at -87.5 ppm which can be assigned to both Q^2 and Q^3 species. However, by referring to Table 2.5 and Figure 2.25 and their respective discussions presented in section 2.5, this peak can be attributed either to distorted Q^2 species or to Q^3 units containing other atoms (particularly Mg or Na) as guest ions (Magi et al. 1984).

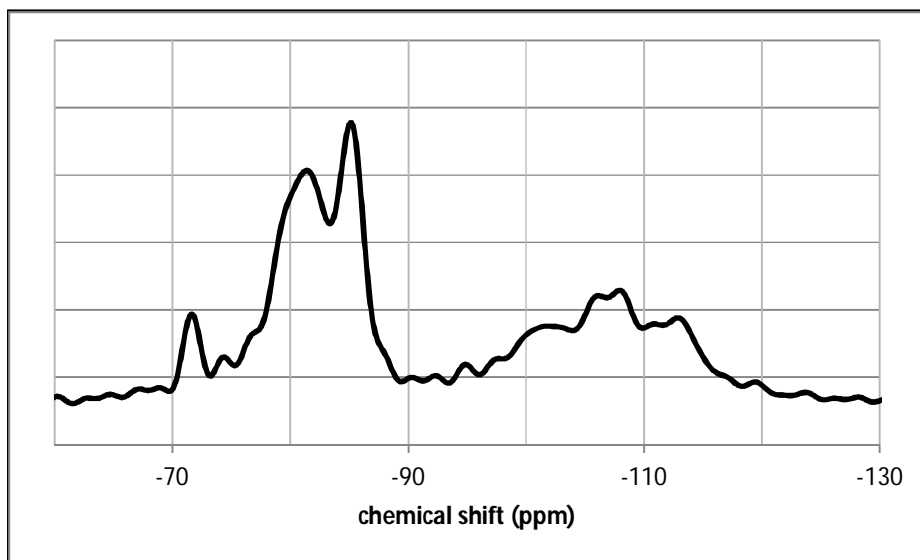


Figure 3.17. ^{29}Si NMR spectra of Htuff-1.

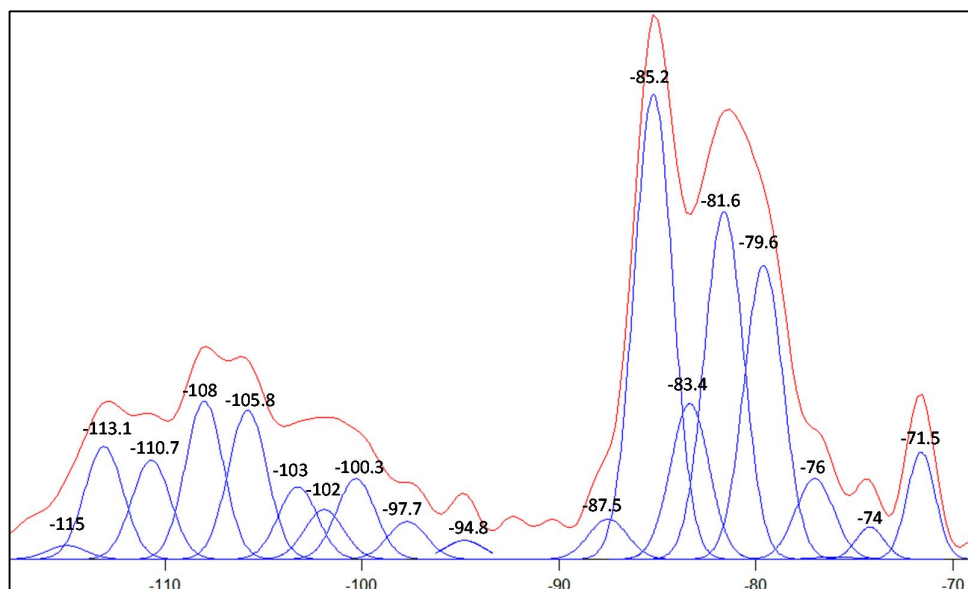


Figure 3.18. The principal peaks in ^{29}Si NMR spectra of Htuff-1.

In the chemical shift range of ca. -95 to ca. -115 there are a numerous peaks originated from (alumino)silicate species within tuff-1, carbonated anhydrous WPC, hydration products of WPC (refer to section 3.5.1) and probably the hydration products of the entire blended system. Although the accurate differentiation between the species in this chemical shift range is very capable of mistake, the peak assignment can be performed over chemical shift ranges. Consequently, the peaks between -94 and -103 ppm can be attributed to Q^3 units ($\text{Q}^3(0\text{Al})$, $\text{Q}^3(1\text{Al})$, $\text{Q}^3(2\text{Al})$) and possibly $\text{Q}^4(3\text{Al})$ species and the peaks between -105 and -115 ppm can be attributed to Q^4 species ($\text{Q}^4(0\text{Al})$, $\text{Q}^4(1\text{Al})$ and $\text{Q}^4(2\text{Al})$).

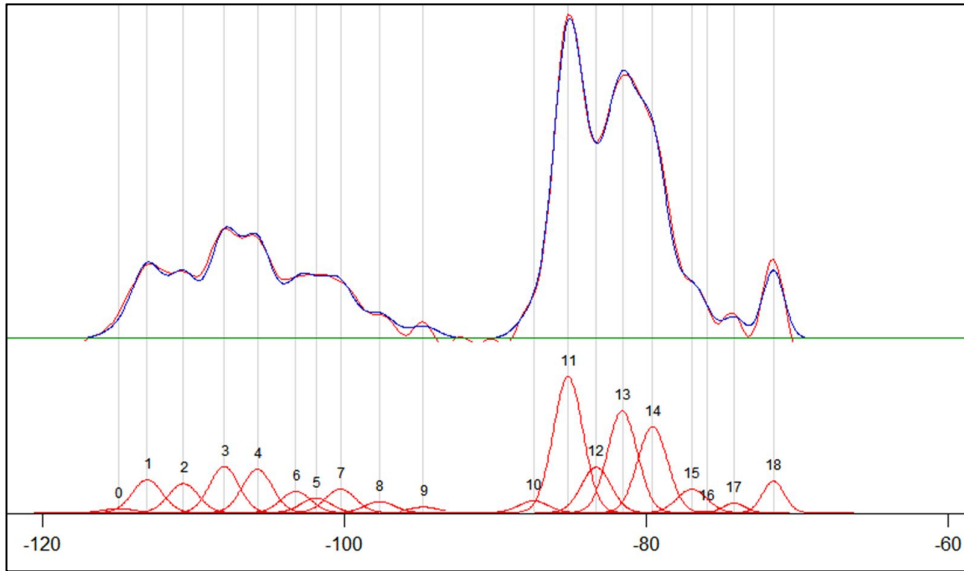


Figure 3.19. Experimental vs. simulated ^{29}Si NMR spectrogram of Htuff-1.

Figure 3.20 reveals that a significant portion of the Q^4 and Q^3 species of the Zeolite phase were consumed during hydration; thus it can be claimed that the structure of Zeolite framework decomposes to some extent when exposed to the alkaline environment of the pore solution in the hydrating paste (Ragnarsdóttir 1993). The hydration products are mostly Q^2 and Q^3 species; these species are the constituents of the structure of C-S-H phase.

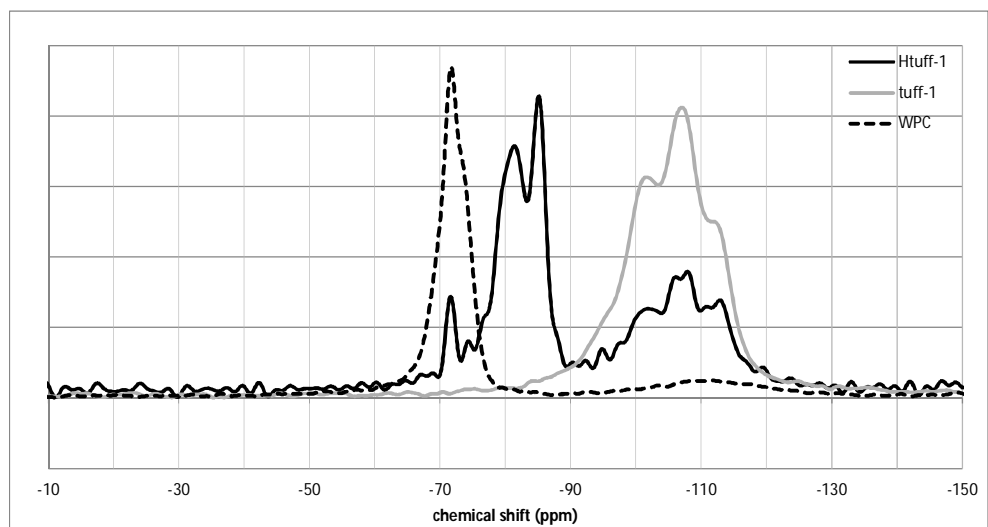


Figure 3.20. Comparative presentation of ^{29}Si NMR spectra of Htuff-1, anhydrous tuff-1 and anhydrous WPC.

3.5.4 ^{27}Al NMR study of Htuff-1

Figure 3.21 shows the ^{27}Al NMR spectra of Htuff-1 and the respective deconvoluted peaks are shown in Figure 3.22. Since there were a great number of peaks observed in the spectra, the peaks that were believed to be originated from similar phases were shown collectively as broader peaks in Figure 3.23. Figure 3.24 gives the comparison of the spectrogram simulated by the use of peaks shown in Figure 3.22 and experimental spectrogram.

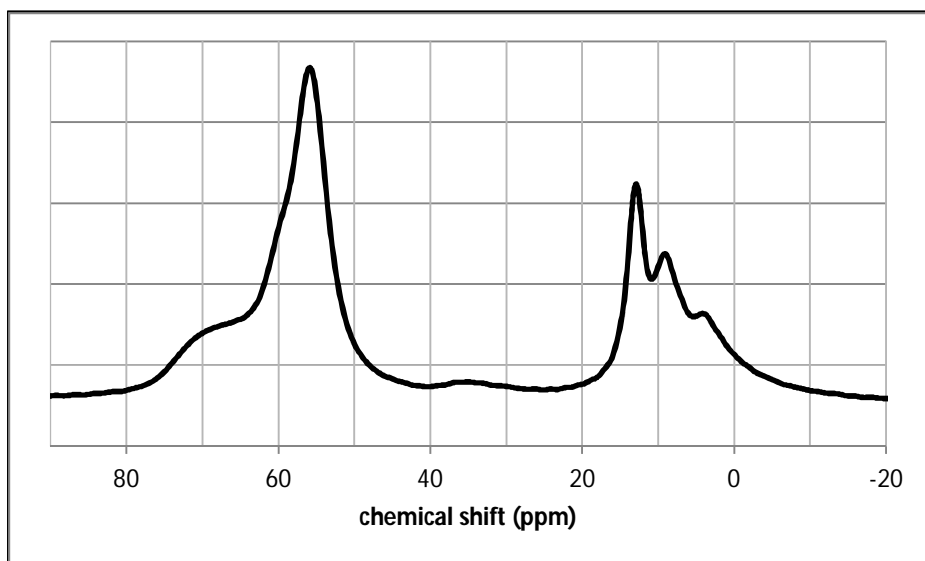


Figure 3.21. ^{27}Al NMR spectra of Htuff-1.

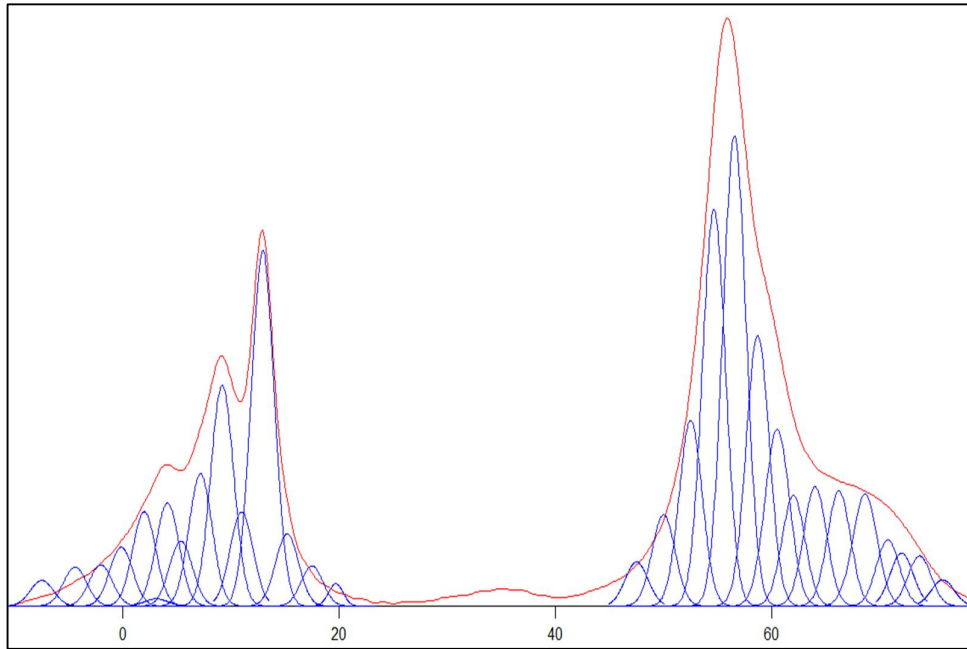


Figure 3.22. The principal peaks in ^{27}Al NMR spectra of Htuff-1.

The peaks in the chemical shift range of 50 to 85 ppm are obviously originated from Aluminum in tetrahedral environments within the unreacted WPC and tuff-1. The peak at 49.5 ppm was attributed to Aluminum nuclei in distorted tetrahedral environments (distorted tetra-coordinated Aluminum) (Mozgawa et al. 2002). The broad peak at ca. 34.8 ppm (Figure 3.23) was attributed to penta-coordinated Aluminum species. All the peaks in the chemical shift range of -2 and 20 ppm were assigned to octa-coordinated Aluminum; these Aluminum species can be attributed either to hydration products of the WPC-tuff-1 blend or to the unreacted WPC.

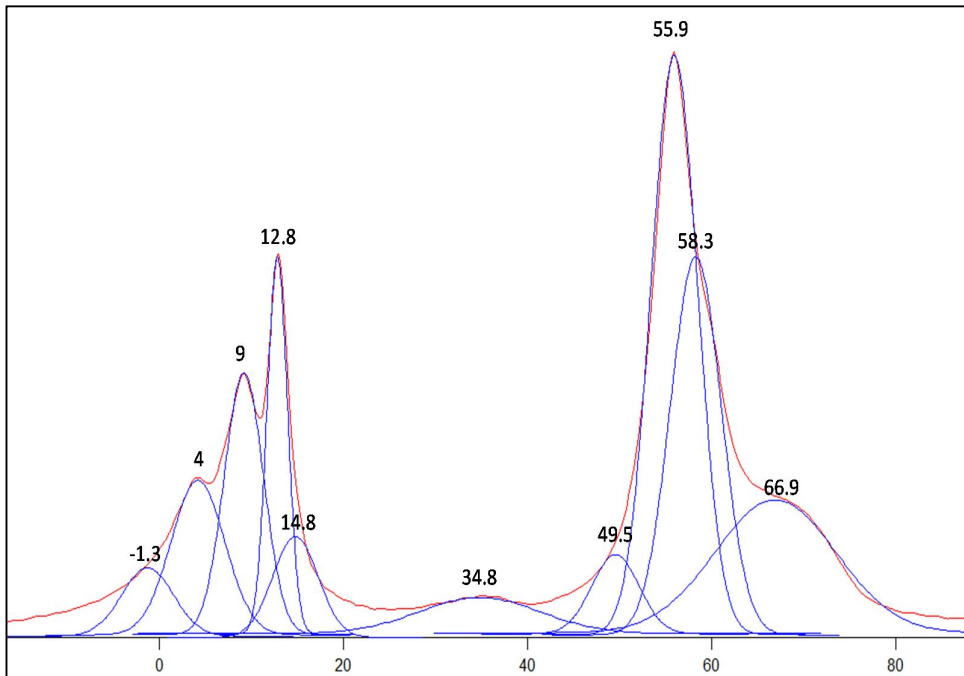


Figure 3.23. Collective presentation of principal peaks in ^{27}Al NMR spectra of Htuff-1.

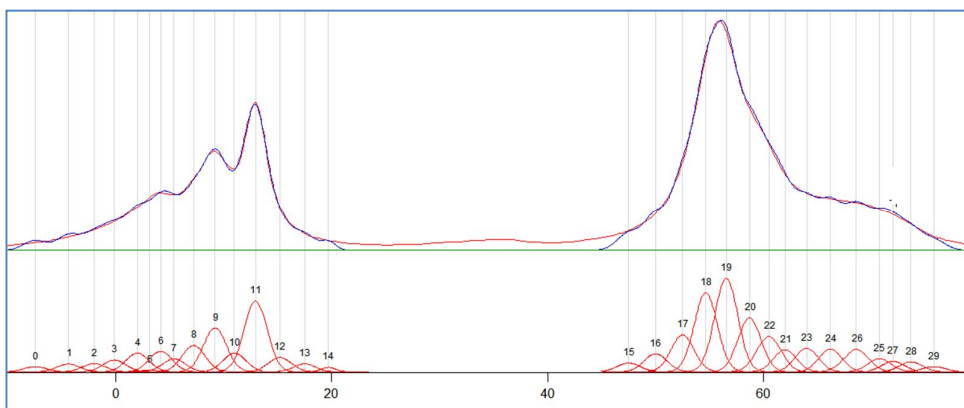


Figure 3.24. Experimental vs. simulated ^{27}Al NMR spectrogram of Htuff-1

3.5.5 ^{29}Si NMR study of Hperlite

Figures 3.25 and 3.26 respectively give the ^{29}Si spectrogram of Hperlite and the deconvoluted peaks in the spectrogram. Following the discussions in sections 3.5.1, 3.5.3 and the ^{29}Si NMR analyses of anhydrous materials in chapter 2, the assignment of peaks to their corresponding phases are presented in this section. The comparison of experimental and simulated spectrograms is presented in Figure 3.27.

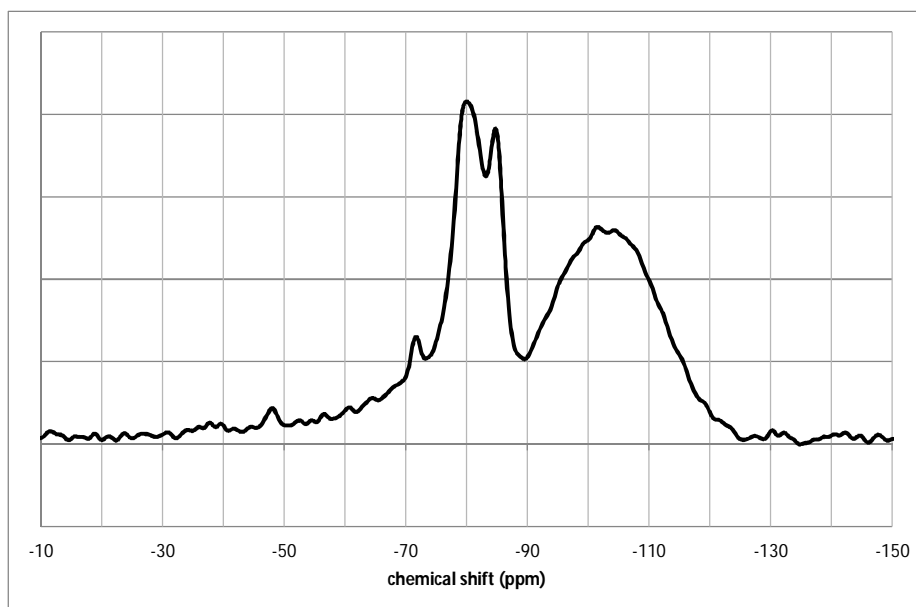


Figure 3.25. ^{29}Si NMR spectra of Hperlite.

The peaks at chemical shifts greater than -79 ppm are ascribed to unreacted Alite and Belite phases. Hence, the peaks at the chemical shift range of -60 to -68 ppm are all assigned to unreacted C_3S . The peak at -71.7 ppm is attributed to unreacted $\beta.C_2S$ and C_3S , while the resonance from the former phase is dominant. The peak at -75 ppm is attributed to Unreacted C_3S and small amounts of inert $\gamma.C_2S$ phase. Other peak of unreacted C_3S appeared in the vicinity of -77 ppm. The peaks at -79.5 ppm and -85 ppm are attributed to Q^1 and $Q^2(OAl)$ species respectively. The two peaks at -82 and -83.5 are assigned to $Q^2(1Al)$ units.

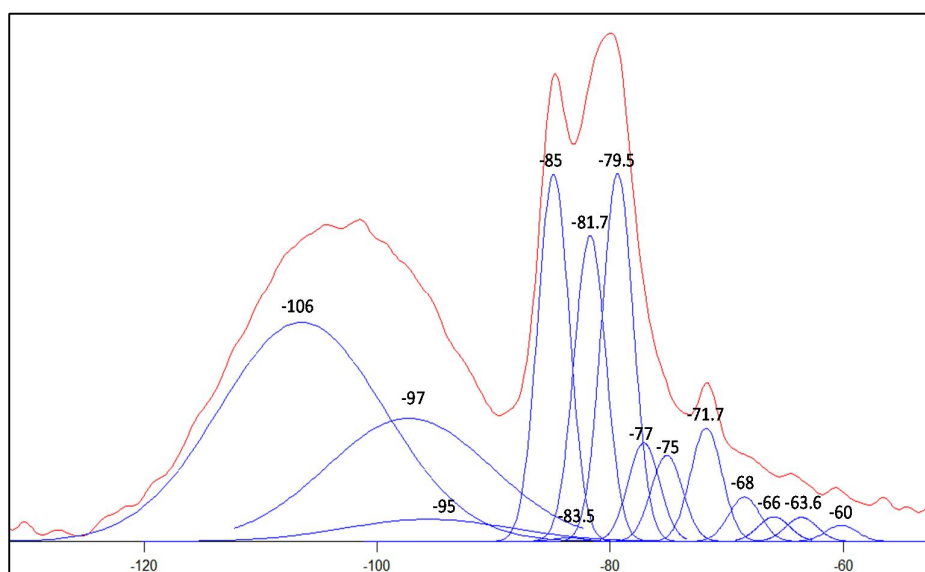


Figure3.26. The principal peaks in ^{29}Si NMR spectra of Hperlite.

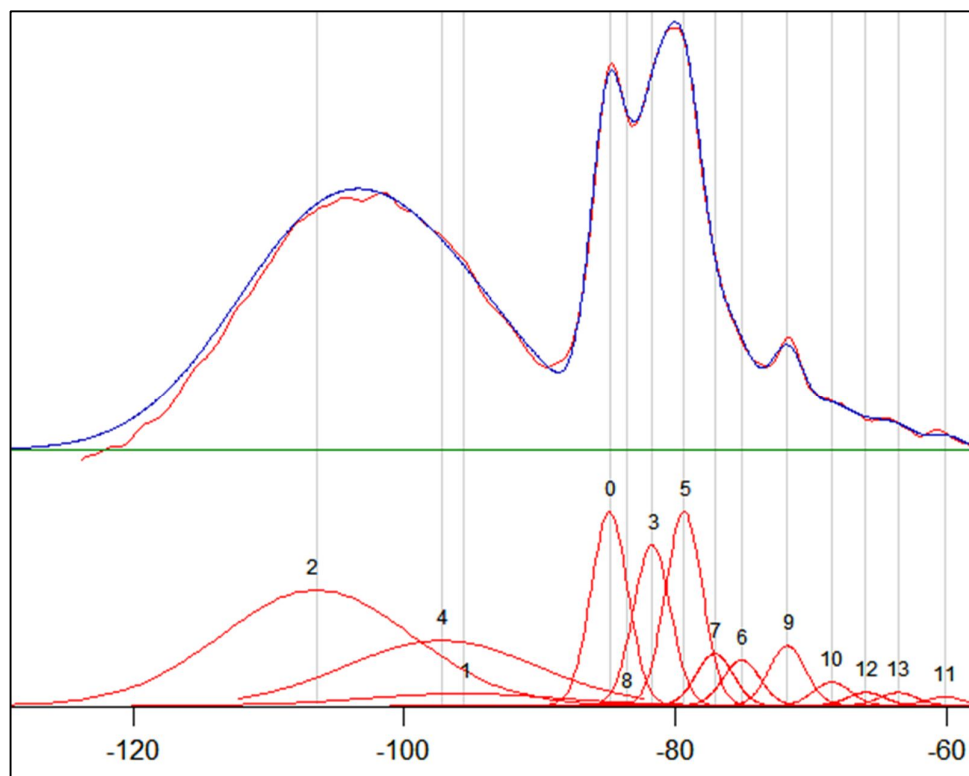


Figure 3.27. Experimental vs. simulated ^{29}Si NMR spectrogram of Hperlite.

It was seen in figures 3.25 and 3.26 that a broad peak had stretched between ca. -90 and ca. -125 ppm. This broad peak was decomposed into three peaks centered at -95, -97 and -106 ppm. As discussed in the previous sections, this peak indicates the presence of a continuous range of Q^3 and Q^4 species within the unreacted materials and possibly the hydration products. The two principal peak-containing chemical shift zones, i.e. the -60 to -85 and the -90 to -125 ranges, are adjacent which increases the possibility of peak overlapping and makes it difficult to separate the peaks of the two zones. Therefore, we assume that Q^3 and Q^4 species with various degrees of Aluminum substitution for silicon are present in the studied paste. In Figure 3.28 it can be seen that the peaks originating from Q^3 and Q^4 units have not been significantly reduced in intensity by 7-month hydration. Therefore, it can be

claimed that the highly polymerized (alumino)silicate phases within the hydrating materials did not provide a significant contribution to the hydration reactions. Rather, the pozzolanic reactivity of perlite powder can be ascribed to the amorphous non-polymerized siliceous phases.

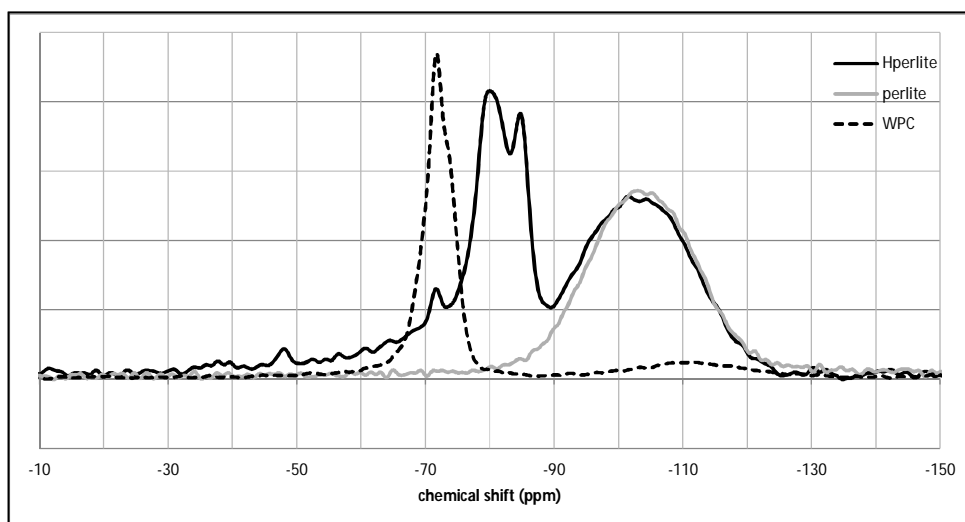


Figure 3.28. Comparative presentation of ^{29}Si NMR spectra of Hperlite, anhydrous perlite and anhydrous WPC.

3.5.6 ^{27}Al NMR study of Hperlite

The ^{27}Al NMR spectra of Hperlite is presented in figure 3.29. Figures 3.30 and 3.31 show the peak deconvolution and the simulated ^{27}Al NMR curve.

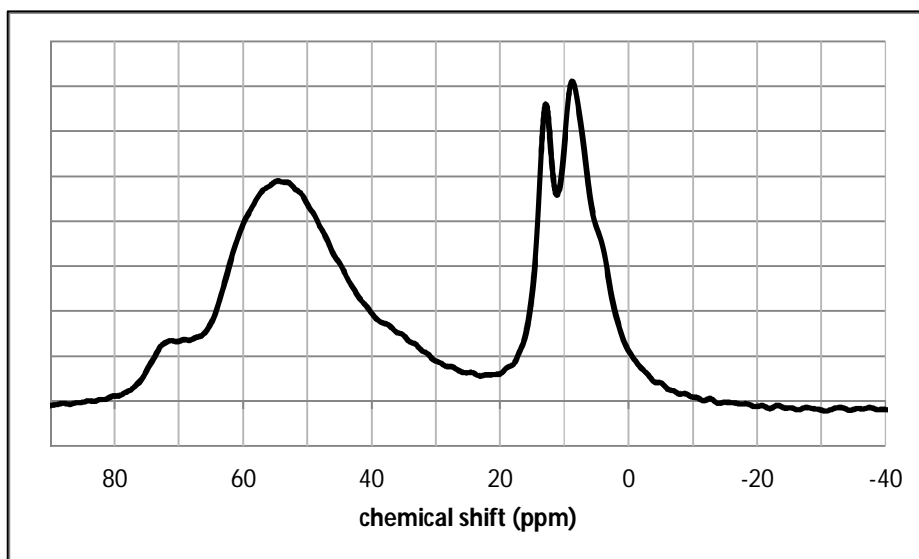


Figure 3.29. ^{27}Al NMR spectra of Hperlite.

The peaks in the chemical shift range of about 50 to 75 ppm are obviously originated from Aluminum in tetrahedral environments within the unreacted WPC and perlite. The peaks at 49 and 44 ppm can be attributed to Aluminum nuclei in distorted tetrahedral environments (distorted tetra-coordinated Aluminum) (Mozgawa et al. 2002). The peaks at ca. 30 and 36 ppm can be, with good certainty, attributed to penta-coordinated Aluminum species. All the peaks in the chemical shift range of -4 and 20 ppm were assigned to octa-coordinated Aluminum; these Aluminum species can be attributed either to hydration products of the WPC-perlite blend or to the unreacted WPC.

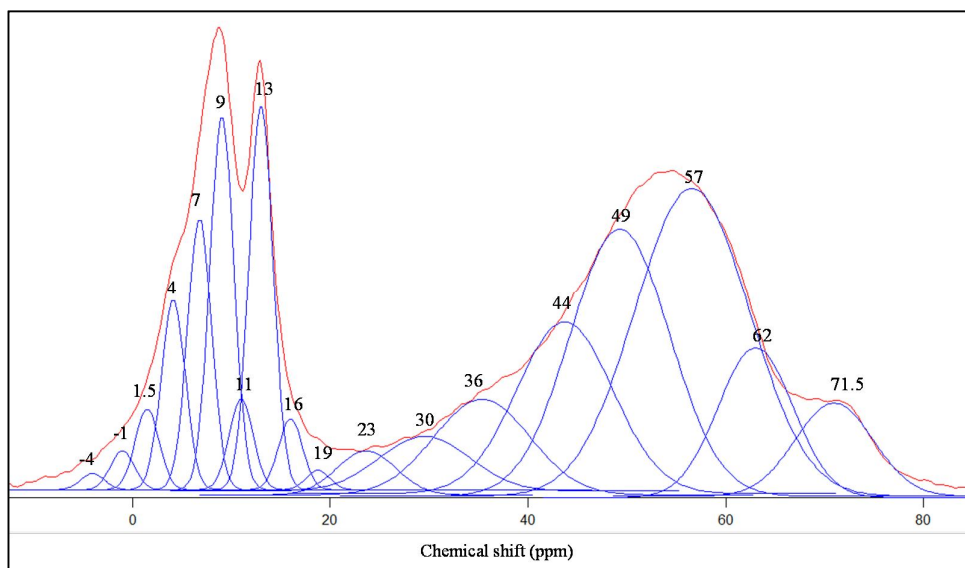


Figure 3.30. The principal peaks in ^{27}Al NMR spectra of Hperlite.

The exact origin of the peak observed at 23 ppm is ambiguous; the presence of two peak-containing chemical shift ranges located very close to each other can cause inaccuracies in the correction of baseline. In addition, special formations of octa- and penta-coordinated Aluminum units can create peaks in this range.

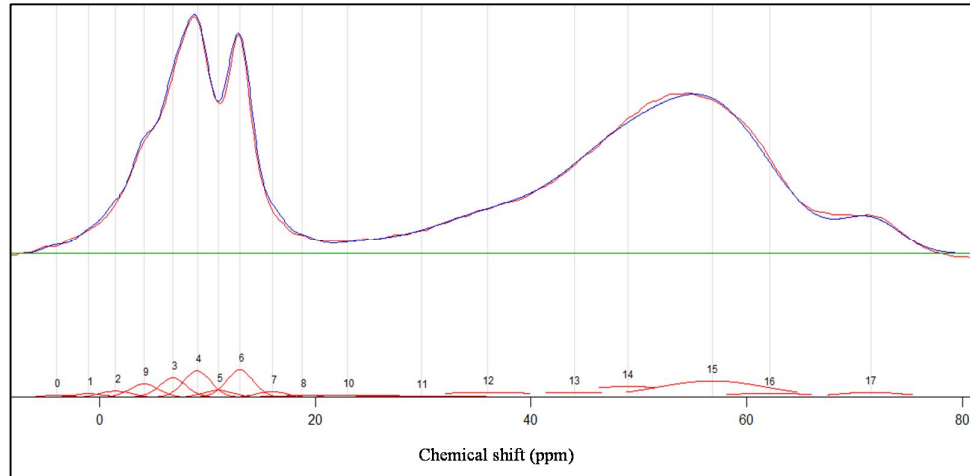


Figure 3.31. Experimental vs. simulated ^{27}Al NMR spectrogram of Hperlite.

3.5.7 ^{29}Si NMR study of Htuff-2

The (alumino)silicate species identified in the WPC-tuff-2 paste sample are presented in this section from the ^{29}Si NMR data in figures 3.32, 3.33 and 3.34. Following the discussions in previous sections, the main species which were readily distinguished in Htuff-2 sample and are presented in the following. The observed characteristic peak(s) of the species are presented in the brackets:

- Unreacted β . C_2S and unreacted C_3S . [-71.7 ppm]
- Unreacted C_3S and possible inert γ . C_2S . [-75.7 ppm]
- Silicate and aluminosilicate species in the C-S-H phase, i.e. Q^1 end-chain nuclei [-79.5 ppm], $\text{Q}^2(1\text{Al})$ [-82 ppm], $\text{Q}^2(0\text{Al})$ middle-chain species [-85 ppm].

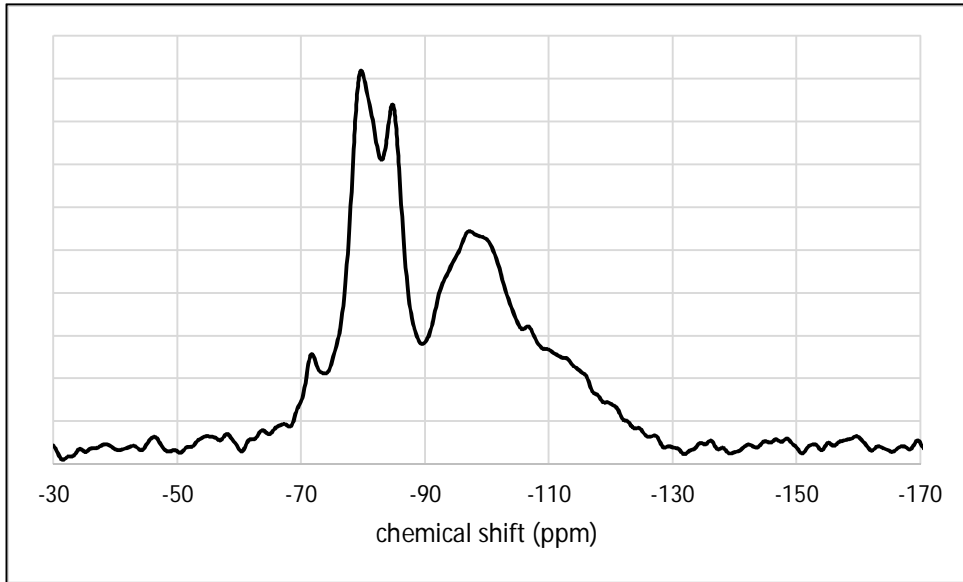


Figure 3.32. ^{29}Si NMR spectra of Htuff-2.

The peaks between -88 and -130 ppm are not identified as easily as the above-mentioned peaks. However, from figure 3.35 and the NMR analyses of anhydrous WPC and anhydrous tuff-2 it becomes quite clear that the peaks in this chemical range shift originate from anhydrous materials. For example in the (-110 ppm)-(-130 ppm) chemical shift range, the effect of the overlapping of resonances from both anhydrous materials is obviously seen. Figure 3.35 shows that the aluminosilicate framework of the framework silicates (feldspar) in tuff-2 is decomposed to some extent. Consequently, a portion of the framework aluminosilicate in tuff-2 participates in pozzolanic reaction and is consumed during hydration. However, as understood from ^{29}Si NMR data of tuff-1 and tuff-2, the feldspar phase is less reactive than the Zeolite phase. It is assumed that the so-called Calcium silicate phase in tuff-2 has a significant contribution to the strength of WPC-tuff-2 systems.

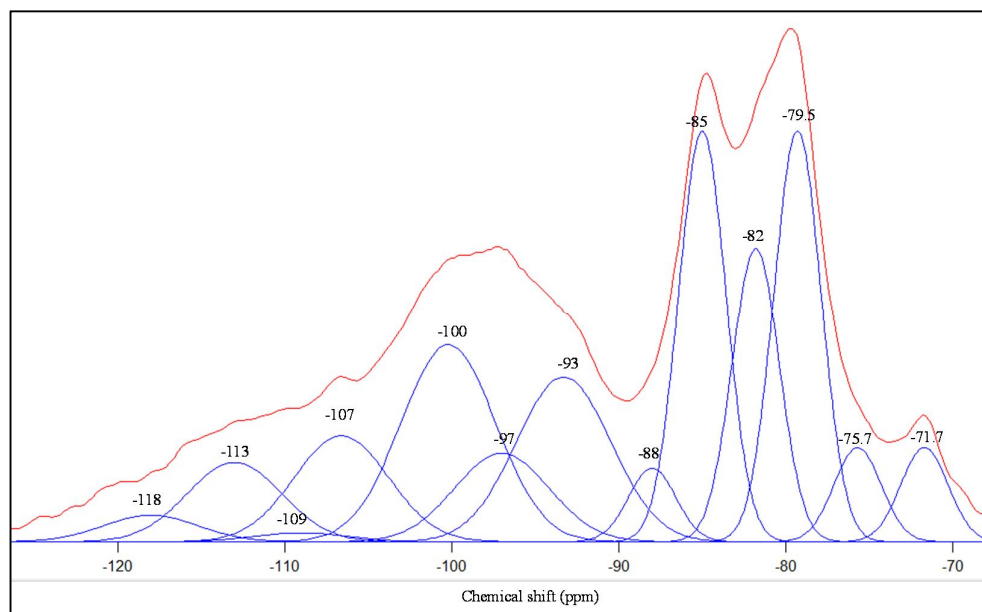


Figure 3.33. The principal peaks in ^{29}Si NMR spectra of Htuff-2.

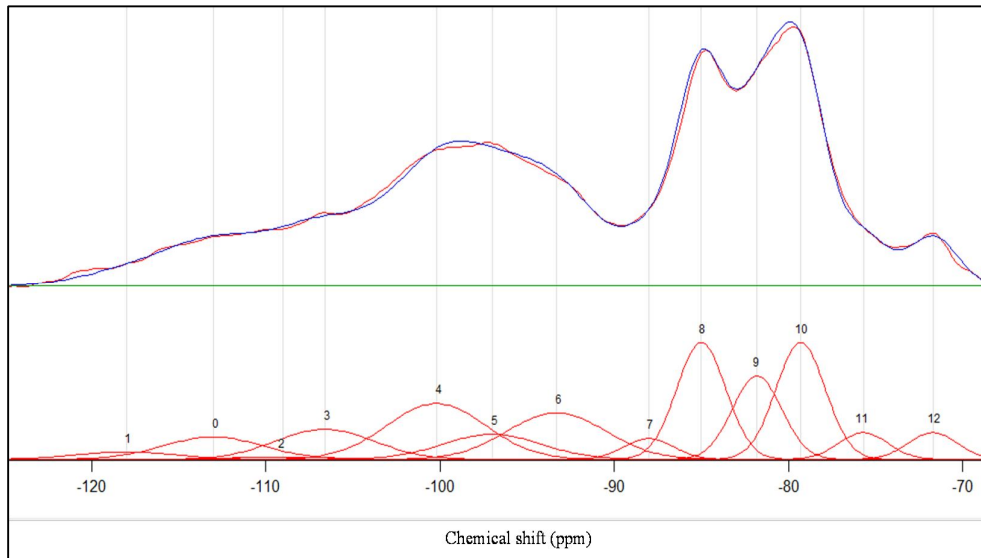


Figure 3.34. Experimental vs. simulated ^{29}Si NMR spectrogram of Htuff-2.

Figure 3.35 shows that a portion of the Q^4 and Q^3 species of tuff-2 sample, attributed to the feldspar and mica phases, were consumed during hydration resulting in production of hydration products which are mainly constituted by Q^1 and Q^2 units. This function of the highly polymerized (alumino)silicate species reveals that the silicate phases within the tuff-2 sample were decomposed to some extent and participated in hydration reactions. However, the reactivity of these phases seems to be lower than the zeolite phase in tuff-1.

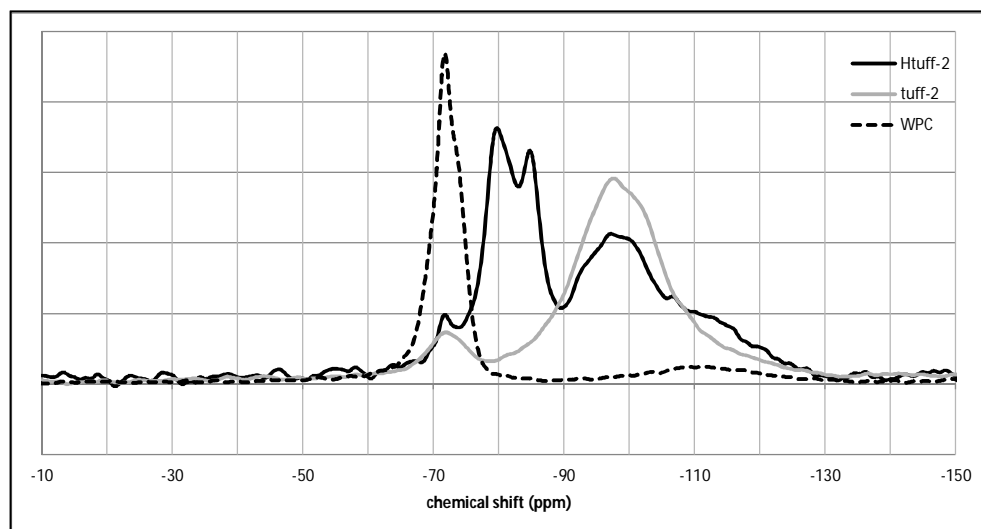


Figure 3.35. Comparative presentation of ^{29}Si NMR spectra of Htuff-2, anhydrous tuff-2 and anhydrous WPC.

3.5.8 ^{27}Al NMR study of Htuff-2

Figures 3.36 to 3.38 give the ^{27}Al NMR data of hydrated WPC-tuff-2 paste. The peaks in the chemical shift range of 50 to 80 ppm are caused by Aluminum in tetrahedral environments, tetrahedral Aluminum is assumed to be supplied by unreacted WPC and tuff-1.

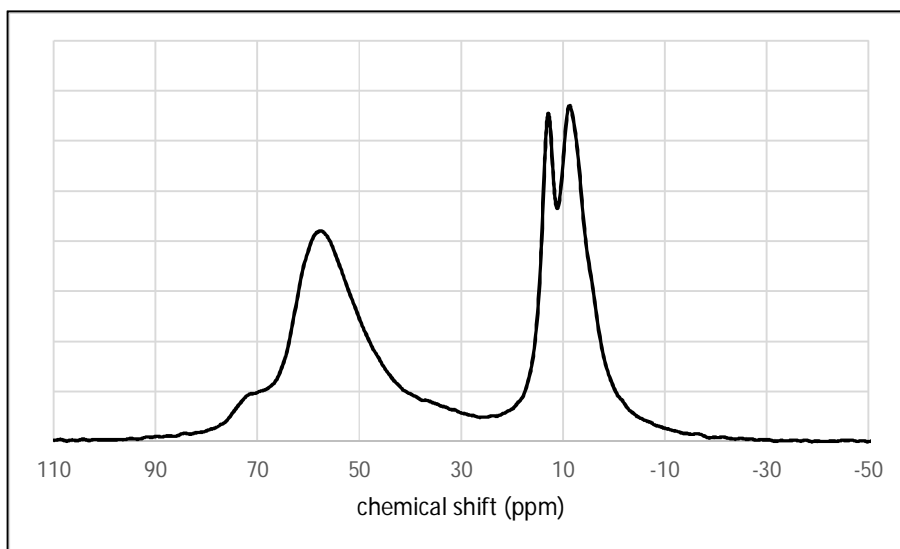


Figure 3.36. ^{27}Al NMR spectra of Htuff-2.

The peak at 48 ppm was attributed to Aluminum nuclei in distorted tetrahedral environments. The broad peak at ca. 37 ppm was attributed to penta-coordinated Aluminum species. All the peaks in the chemical shift range of -2 and 20 ppm were assigned to octa-coordinated Aluminum; these Aluminum species can be attributed either to hydration products of the WPC-tuff-2 blend or to the unreacted WPC. The contribution of unreacted tuff-2 to the intensity of Al_V -induced resonance peaks is assumed to be negligible.

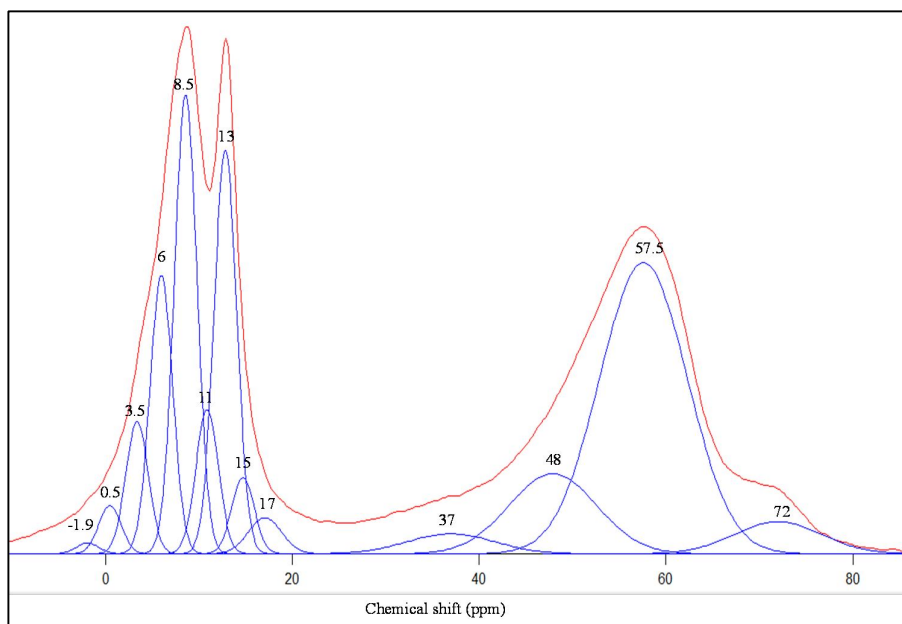


Figure 3.37. The principal peaks in ^{27}Al NMR spectra of Htuff-2.

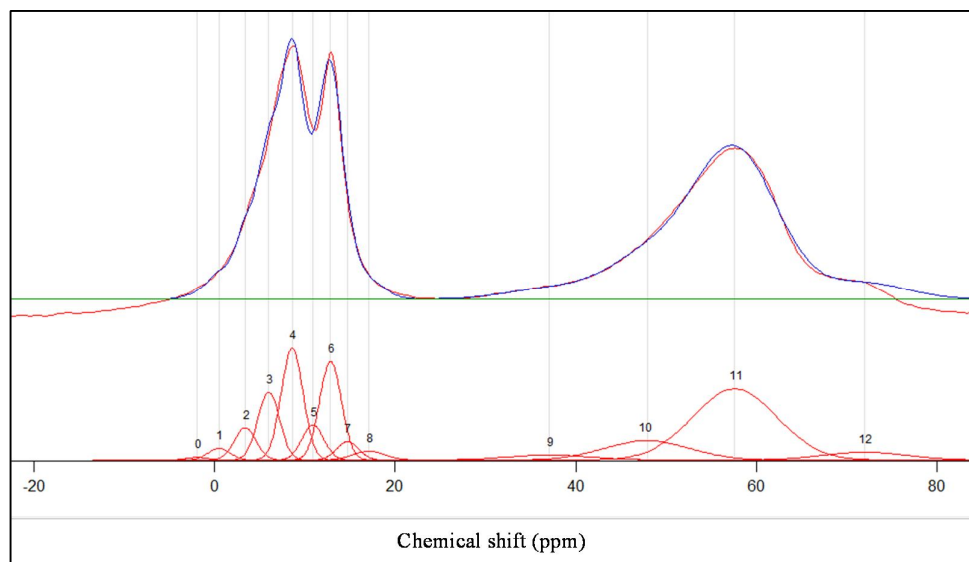


Figure 3.38. Experimental vs. simulated ^{27}Al NMR spectrogram of Htuff-2.

3.6 Quantitative analysis of NMR data

Table 3.4 gives the quantitative analysis of the data obtained by ^{29}Si NMR spectroscopy and discussed in the previous sections (NMR analysis sections in chapters 2 and 3). High concentration of Aluminum in the hydration sites (as we expect in case of additive materials used in our research) results in longer average chain lengths. The mean silicate chain length was considerably increased by the use of tuff-1. The other two NPS also increased the MCL, however they were less effective on this property compared to tuff-1. Considering that the anhydrous tuff-2 already contained some amounts of Q^2 species, its effect on the increase of MCL becomes less significant and thus it should be said that the influence of perlite on the increase of MCL is higher than tuff-2 more than it can be understood from the values of MCL.

Table 3.4. Quantitative analysis results of ^{29}Si NMR data.

	WPC	HWPC	tuff-1	Htuff-1	perlite	Hperlite	tuff-2	Htuff-2
(alumino)silicate species	%							
Q0	85.46	21.40	N.O	9.64	N.O.	9.75	9.96	6.92
Q1	N.O.*	30.70	N.O	12.60	N.O.	11.23	3.92	15.14
Q2 (total)	N.O.	26.57	1.22	43.04	N.O.	20.70	8.16	28.65
Q2(0A) in CSH		15.79		21.54		11.23		17.84
Q2(1A) in CSH		10.79		21.50		9.47		10.81
Q3	2.81	4.07	33.92	11.14	33.36	23.25	41.29	33.08
Q4	11.73	17.26	64.85	23.58	66.64	35.07	36.67	16.22
Mean silicate chain length in CSH [number of silicate tetrahedra]		4.08		10.54		6.53		6.50

* Not observed in the NMR spectra.

Table 3.5 gives the quantitative analysis of the ^{27}Al NMR data. The quantity of each Aluminum species is presented as percentage of the total Aluminum species present in each sample.

Table 3.5. Quantitative analysis results of ^{27}Al NMR data.

Aluminum coordination	WPC	HWPC	tuff-1	Htuff-1	perlite	Hperlite	tuff-2	Htuff-2
	%							
tetra	69.55	8.01	92.76	60.35	81.28	48.43	78.32	48.17
penta	5.82	4.39	6.14	3.34	17.35	13.25	15.93	2.39
octa	24.63	87.60	1.11	60.35	1.37	38.31	5.75	48.17

In tables 3.6 the percentages of the different (alumino)silicate species in anhydrous WPC-NP blends (precursors) and hydrated WPC-NP pastes (products) are compared. This comparison helps to detect the consumption or generation of various species through hydration reactions. Table 3.7 gives the same information in the case of Aluminum species in various coordination sites, i.e. tetra-, penta- and octa-coordinated Aluminum. The mix proportions of the blends were described in chapter 2.

From Table 3.6 it can be deciphered that some amounts of Q^3 and Q^4 species were formed as a result of WPC hydration. Many researchers have investigated the possibility of the generation of silicate species with degrees of polymerization higher than Q^2 in the hydration of neat or pozzolanic Portland cement. (J. F. Young 1988) suggested that any kind of cross-linking in the silicate chains cannot occur in the aluminosilicate structure of PC paste; in other words, Q^3 and Q^4 species are not included in the structure and it is made up only of linear silicate chains. On the other hand, (Currel et al. 1985) had indicated the presence of cross-linked species in a previous study and later (Brough et al. 1994) and (J. Young and Sun 1999b) supported the possibility of the presence of Q^3 and Q^4 species in SCM-blended or carbonated pastes by detection of their peaks in ^{29}Si NMR spectra. However they

couldn't prove the C-S-H origin of the observed Q^3 and Q^4 peaks. (Andersen, Jakobsen, and Skibsted 2003) also reported the absence of any Cross-linking. In this research, the Q^3 and Q^4 species were proved to be formed by the hydration of carbonated WPC. This can be attributed to the carbonation of WPC, as stated before in previous sections of this thesis. However, the XRD results, in which Calcium mono-carboaluminate phase was found, support the idea that these species do not form in the C-S-H phase and they rather constitute a separate Calcium-Carbon-aluminum entity.

Table 3.6 also shows that Q^4 species in tuff-1 and tuff-1 were considerably consumed during the hydration, while in perlite sample the contribution of Q^4 species to hydration reactions was very limited. In tuff-1, the Q^3 units also showed reactivity and were consumed during hydration. While in contrast, the Q^3 species in perlite and tuff-1 did not show considerable reactivity. In fact, the hydration of WPC-perlite and WPC-tuff-2 samples resulted in further generation of Q^3 species beyond the amount generated in the neat WPC paste. Therefore, it can be claimed that the silicate polymerization was enhanced by the presence of these two pozzolans. However, if we assume, based on the existing literature, that most of the observed Q^3 and Q^4 units are not the constituents of the C-S-H phase, the pozzolanic performance of tuff-1 becomes more significant. As seen in table 3.6, the amount of Q^2 species (as the principal constituent of the C-S-H phase) which was produced in the Htuff-1 sample was significantly higher than the other pozzolanic and even neat WPC pastes. The Q^2 content of Htuff-2 was almost similar to that of WPC. This somehow reveals the better pozzolanic performance of tuff-based pozzolans than glass-based pozzolans.

Location and coordination of Aluminum atoms in the C-S-H structure has been subject to numerous studies; however it still remains controversial. (I.G. Richardson 2004; Ian G Richardson et al. 1993) and (Andersen, Jakobsen, and Skibsted 2004) assumed that Al can only substitute for Si in BRIDGING sites (i.e. Q^2_B) with tetrahedral coordination. (P. Faucon, T. Charpentier, D. Bertrandie, A. Nonat, J. Virlet 1998) suggested that Al preferentially substitutes Si in NON-BRIDGING SiO_4 tetrahedra; they also reported the presence of penta-coordinated and octa-coordinated Al in the CaO layer. (Klemesch & Ray 1999) reported the detection of Al in Octahedral coordination in a tobermorite-like structure (I. Richardson 1999).

(Andersen, Jakobsen, and Skibsted 2003) ascribed the octahedral Al to a separate less crystalline calcium aluminate hydrate phase. On the contrary, (Ian G Richardson et al. 1993) argues that Al cannot substitute for Ca in octahedral sites.

The results of this research, shown in tables 3.5 and 3.7, showed that tetrahedral Aluminum sites were present mostly as Aluminum substituted for Silicon in Q² species. Therefore, it can be claimed that Aluminum is more likely to incorporate into the silicate structure of the neat WPC hydration products by substituting Silicon in bridging sites. Although it is also possible that the substituted silicon atoms were the paired Q² units, however, based on the MCL values the bridging tetrahedra were assumed to be the dominant Q² species in the hydration products. The MCL values of the WPC-NP pastes suggest that longer silicate chains are present in the C-S-H phase, consequently it cannot be certainly claimed that bridging sites are the preferred locations of Aluminum accommodation.

Table 3.6. The percentage of various (alumino)silicate species in anhydrous and hydrated WPC-NP blends.

(alumino)silicate species	WPC		WPC-tuff-1		WPC-perlite		WPC-tuff-2	
	%							
	precursors	products	precursors	products	precursors	products	precursors	products
Q0	85.46	21.40	42.73	9.64	42.73	9.75	47.71	6.92
Q1	0.00	30.70	0.00	12.60	0.00	11.23	1.96	15.14
Q2 (total)	0.00	26.57	0.61	43.04	0.00	20.70	4.08	28.65
Q2(0Al)		15.79	0.00	21.54	0.00	11.23	0.00	17.84
Q2(1Al)		10.79	0.00	21.50	0.00	9.47	0.00	10.81
Q3	2.81	4.07	18.36	11.14	18.08	23.25	22.05	33.08
Q4	11.73	17.26	38.29	23.58	39.18	35.07	24.20	16.22

The data in Table 3.7 show that tetrahedral Aluminum is the primary Aluminum species which participates in the hydration reactions. Penta-coordinated Aluminum was also consumed in the hydration reactions of the WPC-tuff-1 and WPC-tuff-2 blends as well as neat WPC. In perlite paste, penta-coordinated Aluminum was produced by the hydration reactions. Octa-coordinated aluminum was the most principal aluminum species produced through the hydration reactions. However the exact accommodating location of these octa-coordinated Aluminum units could not be determined. In NP-blended pastes the amount of the tetrahedral Al is significantly higher than the neat WPC paste. This was attributed to the tetrahedral Aluminum within the aluminosilicate structure of unreacted pozzolans.

Table 3.7. The percentage of various Aluminum species in anhydrous and hydrated WPC-NP blends.

Aluminum coordination	WPC		WPC-tuff-1		WPC-perlite		WPC-tuff-2	
	%							
	precursors	products	precursors	products	precursors	products	precursors	products
tetra	69.5	8.0	81.2	60.4	75.4	48.4	73.9	48.2
penta	5.8	4.4	6.0	3.3	11.6	13.3	10.9	2.4
octa	24.6	87.6	12.9	60.4	13.0	38.3	15.2	48.2

CHAPTER 4

CONCLUSION

4.1 Concluding remarks

In this study three volcanic natural pozzolans were characterized to investigate their chemical and mineral compositions, particle size distribution and fineness as well as the properties of cement-based systems containing these NPs. Tuff-1 had the lowest specific gravity and the highest specific surface area (Blaine fineness) among all the three NPs and the WPC, while its average particle size was larger than the others. This characteristics were attributed to the porosity of the tuff-1 particles, caused mainly by the nano-porous structure of zeolite minerals, which provides a great quantity of surface area for chemical reactions. The particle size and texture properties of the NPs were best reflexed in the setting time and heat of hydration tests.

All the three NPs showed acceptable pozzolanic reactivity with respect to SAI and 90-day compressive strength. Although, the NP-containing mortar samples expectedly gave lower strength than the control (WPC) samples, their rate of strength gaining (the slope of strength-time curve) after 15th day of hydration were higher than control samples. In addition the desirable effect of the NPs on suppressing the ASR expansion of mortar samples was approved by experiment. Tuff-1 exhibited the best performance with respect to effect on compressive strength and ASR expansion. However, tuff-1 is not desirable from workability point of view as its very high water absorption capability results in significant increase in water demand.

The TGA analysis of the anhydrous materials showed that tuff-2 contained very small amounts of water (<2.5wt%) while a significant water content (\approx 10wt%)

was found in tuff-1. This implies the difference in the structure of feldspars and zeolite minerals which relates mainly to the cavity-containing cage structure of zeolites. Perlite was found to contain less than 3wt%. The interesting feature of the TGA analysis of perlite was the loss of a small amount of water at temperatures higher than 900 °C. This is ascribed to the ability of the silicate structure of glass to capture some water which can escape only after decomposition of the silicate structure at temperatures higher than 900 °C.

NMR studies of the anhydrous materials revealed the (alumino)silicate species present in the structure of the material. Tuff-1 consisted mainly of Q⁴ and Q³ units, the former being dominant; very insignificant quantities of Q² units were found in tuff-1 sample. Q⁴ and Q³ species showed the absolute dominance in the perlite sample in which no Q² species could be detected. The structure of tuff-2 was found to have the most complete set of (alumino)silicate units with various degrees of polymerization among all samples, as Q⁰, Q¹, Q², Q³ and Q⁴ units were present in tuff-2. In WPC, Q⁰ units are the only species normally observed; however, on this research Q³ and Q⁴ units were also found in the WPC sample due to carbonation.

The NMR studies showed that the source of the pozzolanic properties of the three NPs were somehow different from each other. Tuff-1 and Tuff-2 did not exhibit high amorphousness in their structure, while perlite was found to be mostly constituted by amorphous siliceous materials. Therefore, factors other than amorphous silicate entities would be involved in the pozzolanic reactivity of the tuff-based NPs. Tuff-1 participates in pozzolanic reactions due to the decomposition of its aluminosilicate framework upon being exposed to alkaline environment of the pore solution. It can be seen in NMR studies that the aluminosilicate framework of tuff-1 participates in the production of C-S-H phase. This is also obviously seen in ²⁷Al NMR. The better performance of tuff-1 in ASR test can also be attributed to the decomposition of its aluminosilicate framework which results in the formation of less positive C-S-H framework by providing more silicate and aluminosilicate anion groups.

As seen in ²⁹Si NMR results of perlite, the framework aluminosilicates have a small contribution to hydration reactions and the majority of reacting phases are within the amorphous aluminosilicate bulk material. Therefore, the pozzolanic

properties of perlite can be attributed to its amorphous aluminosilicate structure. The pozzolanic activity of tuff-2 is ascribed to partial decomposition of the aluminosilicate structure of its constituents (mainly feldspar), however the contribution of the aluminosilicate framework of tuff-2 to pozzolanic reactivity was less than that observed in tuff-1. The reactivity of tuff-2 was enhanced by the presence of a calcium silicate phase in its composition. This calcium silicate phase has a structure similar to those of Alite and Belite, hence, a very reactive phase capable of producing C-S-H (through hydration) is present in tuff-2. However, it is not known that how this phase stays stable when exposed to water in absence of Calcium hydroxide. An interesting finding in this study was the observation of various degrees of cross-linking in the aluminosilicate structure of hydration products.

Replacement of 50% of WPC by NPs was found to increase the MCL in the C-S-H phase. Tuff-1 showed the most significant MCL increase (>100% MCL increase) while perlite (\approx 59% increase) and tuff-2 (<59% increase) took the second and third places. It could be claimed from the NMR results that Aluminum more likely substituted Silicon (within C-S-H) in bridging Q^2 sites. However, the possibility of incorporation of Aluminum in non-bridging sites, in smaller quantities, is still sustained. The Aluminum species primarily consumed during hydration were tetra-coordinated Aluminum species. Penta-coordinated Aluminum was also consumed in the hydration of WPC-tuff-1 and WPC-tuff-2 pastes. While, on the contrary, the hydration of WPC-perlite pastes resulted in the formation of small amounts of penta-coordinated Aluminum. The principal Aluminum species formed in the hydration products was Octa-coordinated Aluminum.

The carbonation of PC was found to impose a considerable effect on the nature of the hydration products as well as the anhydrous PC. Occurrence of Carbonation in the WPC was proved by XRD, TGA and NMR results through detection of Calcite and Calcium carboaluminate phases in the anhydrous WPC. The carbonation of the anhydrous WPC triggered higher polymerization of Q^0 species which resulted in the production of Q^3 and Q^4 species within the hydration products. Regarding the results of the XRD analyses, these highly polymerized (alumino)silicate species are believed to constitute a separate Calcium carboaluminate (Calcium mono-carboaluminate) phase in the hydration products,

and thus, no or very negligible quantities of these species are introduced into the C-S-H structure.

4.2 Recommendations for future work

The field of natural pozzolans is so broad that a vast variety of research can be conducted by using these materials. Here some important gaps encountered in this research are presented for consideration of the scholars who intend to do further research on this subject:

- The Calcium-to-silicate atomic ratio of the C-S-H phase play a crucial role in determination of the nano structure of C-S-H and any model of C-S-H nanostructure should account for this factor. The Ca/Si atomic ratio cannot be precisely determined by means of NMR and SEM techniques. Transmission electron microscopy (TEM) is one of the most efficient and precise techniques for this purpose the application which for determination of Ca/Si ratio in C-S-H can be recommended for future studies.
- It has been reported that the SCM-blended cement pastes experienced an increase in the mean (Alumino) Silicate chain length as they grew older, whereas in neat cement pastes it remained constant with age after a few months. On the other hand, it was assumed by other researchers that the mean silicate chain length in neat cement paste increases with age. Nevertheless, there is no evidence of the validity of any of these reports and assumptions in case of natural pozzolans.
- The role of Ca-OH bonds in the structure of the resulting C-S-H phase in the presence of NPs still remains questionable. It should be investigated whether or not $\text{Ca}(\text{OH})_2$ is present in the interlayer.
- Investigation of the effect of the ion-exchange property of zeolites on the pozzolanic reactivity and the involved mechanisms.
- Alkali-activation of natural pozzolans have been studied and reported in the existing literature. However, since not all alkaline materials are effective on a particular pozzolan, the suitable alkali solution (composition and dosage) for activation of the studied NPs remain to be studied. However, in case of perlite there are sufficient publications which discuss the appropriate alkaline solutions

for activation of perlite powder. Mechanisms of the formation of geopolymers in alkali-activated NPs can be traced by NMR techniques.

- Performing the techniques used in this study, in a regular manner, with appropriate intervals over a long-term period (for example one year) can give an insightful knowledge about the nature of the pozzolanic reaction and C-S-H formation mechanisms.
- The morphology and Ca/Si ratio are different between inner and outer product C-S-H. This can be investigated by means of SEM and TEM techniques as well as electron microprobe analysis.
- Modeling the structure of hydration products by means of molecular dynamics would be very useful for understanding the structure and performance of pozzolan-containing cementitious systems.

REFERENCES

- Alietti A, Passaglia E, Scaini G. 1967. "A New Occurrence of Ferrierite." *American Mineralogist* 52: 1562–63.
- Andersen, Morten Daugaard, Hans J Jakobsen, and Jørgen Skibsted. 2003. "Incorporation of Aluminum in the Calcium Silicate Hydrate (C-S-H) of Hydrated Portland Cements: a High-Field ^{27}Al and ^{29}Si MAS NMR Investigation." *Inorganic chemistry* 42(7): 2280–87.
- Andersen, Morten Daugaard, Hans J. Jakobsen, and Jørgen Skibsted. 2004. "Characterization of White Portland Cement Hydration and the C-S-H Structure in the Presence of Sodium Aluminate by ^{27}Al and ^{29}Si MAS NMR Spectroscopy." *Cement and Concrete Research* 34(5): 857–68.
- Barjasteh, Arash. 2010. "Seismic Vulnerability of Historic Hydraulic Structures of Shushtar City, Southwestern Iran." In *The 1 st International Applied Geological Congress*, Mashad, Iran, 26–28.
- Battocchio, Francesco, Paulo J.M. Monteiro, and Hans-Rudolf Wenk. 2012. "Rietveld Refinement of the Structures of 1.0 C-S-H and 1.5 C-S-H." *Cement and Concrete Research* 42(11): 1534–48.
- Beaudoin, James J., Laila Raki, and Rouhollah Alizadeh. 2009. "A ^{29}Si MAS NMR Study of Modified C–S–H Nanostructures." *Cement and Concrete Composites* 31(8): 585–90.
- Bektas, F., L. Turanli, and P.J.M. Monteiro. 2005. "Use of Perlite Powder to Suppress the Alkali–silica Reaction." *Cement and Concrete Research* 35(10): 2014–17.
- Bish D.L., Ming D.W., ed. 2001. 45 Reviews in mineralogy and ... *Natural Zeolites: Occurance, Properties, Applications*. mineralogical society of America.
- Black, Leon, Krassimir Garbev, Günter Beuchle, Peter Stemmermann, and Dieter Schild. 2006. "X-Ray Photoelectron Spectroscopic Investigation of Nanocrystalline Calcium Silicate Hydrates Synthesised by Reactive Milling." *Cement and Concrete Research* 36(6): 1023–31.
- Bondar, Dali, C.J. Lynsdale, Neil B. Milestone, N. Hassani, and Ali Akbar Ramezani-pour. 2011. "Effect of Type, Form, and Dosage of Activators on

- Strength of Alkali-Activated Natural Pozzolans.” *Cement and Concrete Composites* 33(2): 251–60.
- Brough, AR, CM Dobson, Ian G Richardson, and Geoffrey W Groves. 1994. “Application of Selective ²⁹Si Isotopic Enrichment to Studies of the Structure of Calcium Silicate Hydrate (C-S-H) Gels.” *Journal of the American Ceramic Society* 77(2): 593–96.
- Brunet, F., T. Charpentier, C.N. Chao, H. Peycelon, and a. Nonat. 2010. “Characterization by Solid-State NMR and Selective Dissolution Techniques of Anhydrous and Hydrated CEM V Cement Pastes.” *Cement and Concrete Research* 40(2): 208–19.
- Celik, K., M.D. Jackson, M. Mancio, Cagla Meral, A.H. Emwas, P.K. Mehta, and Paulo J.M. Monteiro. 2014. “High-Volume Natural Volcanic Pozzolan and Limestone Powder as Partial Replacements for Portland Cement in Self-Compacting and Sustainable Concrete.” *Cement and Concrete Composites* 45: 136–47.
- Celik, Kemal, Cagla Meral, and Mauricio Mancio. 2013. “A Comparative Study of Self-Consolidating Concretes Incorporating High-Volume Natural Pozzolan or High-Volume Fly Ash.” *Construction and Building Materials and Building Materials*.
- Celik, Kemal, Cagla Meral, Mauricio Mancio, P. Kumar Mehta, and Paulo J.M. Monteiro. 2013. “A Comparative Study of Self-Consolidating Concretes Incorporating High-Volume Natural Pozzolan or High-Volume Fly Ash.” *Construction and Building Materials*.
- Cement and Concrete Terminology, ACI 116R-00*. 1985. Michigan.
- Chen, Jeffrey J., Jeffrey J. Thomas, Hal F.W. Taylor, and Hamlin M. Jennings. 2004. “Solubility and Structure of Calcium Silicate Hydrate.” *Cement and Concrete Research* 34(9): 1499–1519.
- Cho, M., S. Maruyama, and J. G. Liou. 1987. “An Experimental Investigation of Heulandite-Laumontite Equilibrium at 1000 to 2000 Bar P Fluid.” *Contributions to Mineralogy and Petrology* 97(1): 43–50.
- Davidovits, Joseph, Ed. 2005. *Green Chemistry and Sustainable Development Solutions: Proceedings of the World Congress Geopolymer*. ed. J. Davidovits. Geopolymer Institute,.
- Demir, Ismail, and M. Serhat Baspinar. 2008. “Effect of Silica Fume and Expanded Perlite Addition on the Technical Properties of the Fly Ash–lime–gypsum Mixture.” *Construction and Building Materials* 22(6): 1299–1304.
- Erdem, T.K., Cagla Meral, M Tokyay, and T.Y. Erdogan. 2007. “Effect of Ground Perlite Incorporation on the Performance of Blended Cements.” In *Proc. Int. Conf: Sustainable construction materials and technologies*, eds. Y.M. Chun, P.

- Claisse, T.R. Naik, and E. Ganjian. 11-13 June 2007 Coventry: Taylor and Francis, London, ISBN 13: 978-0-415-44689-1, 279–85.
- Erdem, T.K., Cagla Meral, M Tokyay, and TY Erdoğan. 2007. “Use of Perlite as a Pozzolanic Addition in Producing Blended Cements” eds. Y.M. Chun, P. Claisse, T.R. Naik, and E. Ganjian. *Cement and Concrete Composites* 29(1): 13–21.
- Eser, Hasan. 2014. “High Performance Estructural Lightweight Concrete Utilizing Natural Perlite Aggregate and Perlite Powder.” middle east technical university.
- “ESRL, NOAA. ‘Earth System Research Laboratory.’ Trends in Atmospheric Carbon Dioxide [online].” < http://www.esrl.noaa.gov/gmd/ccgg/trends/co2_data_mlo.html> (May 10, 2013).
- Faucon, P, A Delagrave, J C Petit, C Richet, J M Marchand, H Zanni, and V La. 1999. “Aluminum Incorporation in Calcium Silicate Hydrates (CSH) Depending on Their Ca/Si Ratio.” *The Journal of Physical Chemistry* 103: 7796–7802.
- Fernandez, Rodrigo, Fernando Martirena, and Karen L. Scrivener. 2011. “The Origin of the Pozzolanic Activity of Calcined Clay Minerals: A Comparison Between Kaolinite, Illite and Montmorillonite.” *Cement and Concrete Research* 41(1): 113–22.
- Girao, a. V., I. G. Richardson, C. B. Porteneuve, and R. M. D. Brydson. 2007. “Morphology and Nanostructure C–S–H in White Portland Cement–fly Ash Hydrated at 85°C.” *Advances in Applied Ceramics* 106(6): 283–93.
- Girao, A.V. 2007. “THE NANOSTRUCTURE AND DEGRADATION OF C-S-H IN PORTLAND AND BLENDED CEMENTS.” The University of Leeds.
- Girão, A.V., I.G. Richardson, C.B. Porteneuve, and R.M.D. Brydson. 2007. “Composition, Morphology and Nanostructure of C–S–H in White Portland Cement Pastes Hydrated at 55 °C.” *Cement and Concrete Research* 37(12): 1571–82.
- Girão, A.V., I.G. Richardson, R. Taylor, and R.M.D. Brydson. 2010. “Composition, Morphology and Nanostructure of C–S–H in 70% White Portland Cement–30% Fly Ash Blends Hydrated at 55°C.” *Cement and Concrete Research* 40(9): 1350–59.
- Godelitsas, Ath., and Th. Armbruster. 2003. “HEU-Type Zeolites Modified by Transition Elements and Lead.” *Microporous and Mesoporous Materials* 61(1-3): 3–24.
- Grutzeck, Michael, Alan Benesi, and Barry Fanning. 1989. “Silicon-29 Magic Angle Spinning Nuclear Magnetic Resonance Study of Calcium Silicate Hydrates.” *Journal of the American Ceramic Society* 68(4): 665–68.

- Gürsel, A Petek, and Çağla Meral. 2012. “Türkiye’de Çimento Üretimini Karşılaştırmalı Yaşam Döngüsü Analizi.” In *2. Proje ve Yapım Yönetimi Kongresi, İzmir Yüksek Teknoloji Enstitüsü, Urla-İzmir*, 1–13.
- Gursel, Petek, Cagla Meral, Arpad Horvath, and Paulo J.M. Monteiro. 2013. “Comparative Analysis of Life-Cycle Global Warming Potential (GWP) of Mortar Mixes Using the GreenConcrete LCA Tool.” In *2013 International Concrete Sustainability Conference, May 6-8, San Francisco*.
- Helvacı, C, and O Alaca. 1991. “Geology and Mineralogy of the Bigadiç Borate Deposits and Vicinity.” *Mineral Res. Expl. Bull* 113: 31–63.
- Hewlett, P. c. 2004. *Lea’s Chemistry of Cement and Concrete*. 4th ed. ed. P. c. Hewlett. Elsevier.
- Ipavec, Andrej, Roman Gabrovšek, Tomaž Vuk, Venčeslav Kaučič, Jadran Maček, and Anton Meden. 2011. “Carboaluminate Phases Formation During the Hydration of Calcite-Containing Portland Cement.” *Journal of the American Ceramic Society* 94(4): 1238–42.
- “JCPDS PDF-2 Database.” 2004.
- Jennings, HM. 2000. “A Model for the Microstructure of Calcium Silicate Hydrate in Cement Paste.” *Cement and Concrete Research* 30(May 1999): 101–16.
- John W. Anthony, Richard A. Bideaux, Kenneth W. Bladh, and Monte C. Nichols, Eds. 2003. *Handbook of Mineralogy, Mineralogical Society of America*. Chantilly, VA 20151-1110, USA.
- Justnes, H, and I Meland. 1990. “A 29 Si MAS NMR Study of the Pozzolanic Activity of Condensed Silica Fume and the Hydration of Di-and Tricalcium Silicates.” *Advances in Cement ...* 3(11): 111 –116.
- Keller, w.D., Picket, E.E. 1954. “Hydroxyl and Water in Perlite from Superior Arizona.” *American Journal of Science* 252(February): 87–98.
- Korkuna, O., R. Leboda, J. Skubiszewska-Zieba, T. Vrublevs’ka, V.M. Gun’ko, and J. Ryzkowski. 2006. “Structural and Physicochemical Properties of Natural Zeolites: Clinoptilolite and Mordenite.” *Microporous and Mesoporous Materials* 87(3): 243–54.
- Liebig, E, and E Althaus. 1998. “Pozzolanic Activity of Volcanic Tuff and Suevite: Effects of Calcination.” *Cement and concrete research* 28(4): 567–75.
- Lippmaa, E, and M Mägi. 1981. “Investigation of the Structure of Zeolites by Solid-State High-Resolution Silicon-29 NMR Spectroscopy.” *Journal of the American Chemical Society* 103(17): 4992–96.
- Lothenbach, Barbara, Karen Scrivener, and R.D. Hooton. 2011. “Supplementary Cementitious Materials.” *Cement and Concrete Research* 41(3): 217–29.

- Love, C.a., I.G. Richardson, and a.R. Brough. 2007. "Composition and Structure of C–S–H in White Portland Cement–20% Metakaolin Pastes Hydrated at 25 °C." *Cement and Concrete Research* 37(2): 109–17.
- Lu, P, and JF Young. 1993. "Slag–Portland Cement Based DSP Paste." *Journal of the American Ceramic Society* 76(5): 1329–34.
- Maeshima, Takayuki, Hiroaki Noma, Masato Sakiyama, and Takeshi Mitsuda. 2003. "Natural 1.1 and 1.4 Nm Tobermorites from Fuka, Okayama, Japan." *Cement and Concrete Research* 33(10): 1515–23.
- Magi, M., E. Lippmaa, A. Samoson, G. Engelhardt, and A. R. Grimmer. 1984. "Solid-State High-Resolution Silicon-29 Chemical Shifts in Silicates." *The Journal of Physical Chemistry* 88(8): 1518–22.
- Malinowski, R., Garfinkel, Y. 1991. "Prehistory of Concrete." *Concrete International* 13(3).
- Martinezramirez, S, M Blancovarela, I Erena, and M Gener. 2006. "Pozzolanic Reactivity of Zeolitic Rocks from Two Different Cuban Deposits: Characterization of Reaction Products." *Applied Clay Science* 32(1-2): 40–52.
- Massazza F. 1993. "Pozzolanic Cements." *Cement and concrete composites* 15: 185–214,.
- Méducin, Fabienne, Bruno Bresson, Nicolas Lequeux, Marie-Noëlle De Noirfontaine, and Hélène Zanni. 2007. "Calcium Silicate Hydrates Investigated by Solid-state High Resolution ¹H and ²⁹Si Nuclear Magnetic Resonance." *Cement and Concrete Research* 37(5): 631–38.
- Mehta, P. K., and Paulo J.M. Monteiro. 2006. *Concrete: Microstructure, Properties, and Materials*.
- Mehta, PK, and Paulo JM. Monteiro. 2006. *Concrete:Microstructure, Properties, and Materials*. Berkeley:McGraw-Hill.
- Mielenz, R. C., Greene K. T., Schieltz N. C. 1951. "Natural Pozzolans for Concrete." *economic geology* 46: 311–28.
- Ming, DW, and JB Dixon. 1986. "Clinoptilolite in South Texas Soils." *Soil Science Society of America ...* 72: 1618–22.
- Mohan, K, H F W Taylor, A E Moore, C D Lawrence, E E Lachowski, Between Analytical, Electron Microscopy, Electron Probe Microanalysis, D L Kantro, Portland Cement, Cement Pastes, P L Pratt, J A Dalziel, W A Gutteridge, D D Double, G W Groves, W A Guttridge, H Hornain, Cement Paste, A J Majumdar, Portland Cement Pastes, J M Illston, Derivative Thermogravimetry, I J Smalley, D C Killoh, H M Jennings, and L Scrivener. 1985. "Analytical Study of Pure and Extended Portland Cement Pastes : 11 ," *Journal of American Ceramic Society* 68(December): 685–90.

- Moon, Juhuk, Jae Eun Oh, Magdalena Balonis, Fredrik P. Glasser, Simon M. Clark, and Paulo J.M. Monteiro. 2012. "High Pressure Study of Low Compressibility Tetracalcium Aluminum Carbonate Hydrates $3\text{CaO}\cdot\text{Al}_2\text{O}_3\cdot\text{CaCO}_3\cdot 11\text{H}_2\text{O}$." *Cement and Concrete Research* 42(1): 105–10.
- Mozgawa, W, Z Fojud, M Handke, and S Jurga. 2002. "MAS NMR and FTIR Spectra of Framework Aluminosilicates." *Journal of Molecular Structure* 614(1-3): 281–87.
- Mumpton, F. 1960. "Clinoptilolite Redefined." *American Mineralogist* 45: 351–69.
- Naiqian, Feng, and Hao Tingyu. 1998. "Mechanism of Natural Zeolite Powder in Preventing Alkali—silica Reaction in Concrete." *Advances in Cement Research* 10(3): 101–8.
- Noh, JH. 1998. "Geochemistry and Paragenesis of Heulandite Cements in a Miocene Marine Fan-Delta System of the Pohang Basin, Republic of Korea." *Clays and clay minerals* 46(2): 204–14.
- Nonat, André. 2004. "The Structure and Stoichiometry of C-S-H." *Cement and Concrete Research* 34(9): 1521–28.
- P. Faucon, T. Charpentier, D. Bertrandie, A. Nonat, J. Virlet, J.C. Petit. 1998. "Characterization of Calcium Aluminate Hydrates of Cement Pastes by ^{27}Al MQ-MAS NMR." *inorganic chemistry journal* 37(15): 3726–33.
- Page, C.L., Page, M.M., ed. 2007. *Durability of Concrete and Cement Composites*. Boca Raton, Fla.: Cambridge, Eng. : Woodhead Publishing Ltd.,.
- Pane, Ivindra, and Will Hansen. 2005. "Investigation of Blended Cement Hydration by Isothermal Calorimetry and Thermal Analysis." *Cement and Concrete Research* 35(6): 1155–64.
- Pardal, Xiaolin, Francine Brunet, and Thibault Charpentier. 2012. " ^{27}Al and ^{29}Si Solid-State NMR Characterization of Calcium-Aluminosilicate-Hydrate." *Inorganic chemistry* 51: 1827–36.
- Pellenq, Roland J-M, Akihiro Kushima, Rouzbeh Shahsavari, Krystyn J Van Vliet, Markus J Buehler, Sidney Yip, and Franz-Josef Ulm. 2009. "A Realistic Molecular Model of Cement Hydrates." *Proceedings of the National Academy of Sciences of the United States of America* 106(38): 16102–7.
- Perraki, Th., and a. Orfanoudaki. 2004. "Mineralogical Study of Zeolites from Pentelofos Area, Thrace, Greece." *Applied Clay Science* 25(1-2): 9–16.
- Petrini, R. 2001. "Influence of Magma Dynamics on Melt Structure: Spectroscopic Studies on Volcanic Glasses from the Cretatio Tephra of Ischia (Italy)." *Contributions to Mineralogy and Petrology* 140(5): 532–42.

- Petrini, R., C. Forte, G. Contin, C. Pinzino, and G. Orsi. 1999. "Structure of Volcanic Glasses from the NMR-EPR Perspective: a Preliminary Application to the Neapolitan Yellow Tuff." *Bulletin of Volcanology* 60(6): 425–31.
- Quanlin, Niu, and Feng Naiqian. 2005. "Effect of Modified Zeolite on the Expansion of Alkaline Silica Reaction." *Cement and Concrete Research* 35(9): 1784–88.
- Ragnarsdóttir, KV. 1993. "Dissolution Kinetics of Heulandite at pH 2–12 and 25 C." *Geochimica et cosmochimica acta* 57: 2439–49.
- Raki, Laila, James Beaudoin, Rouhollah Alizadeh, Jon Makar, and Taijiro Sato. 2010. "Cement and Concrete Nanoscience and Nanotechnology." *Materials* 3(2): 918–42.
- Ramachandran, Vangi S. 2001. "Thermal Analysis." In *HANDBOOK OF ANALYTICAL TECHNIQUES IN CONCRETE SCIENCE AND TECHNOLOGY Principles, Techniques, and Applications*, ed. James J. Ramachandran, V.S., Beaudoin. Elsevier, 127–73.
- Ramdas, Subramaniam, and Jacek Klinowski. 1984. "A Simple Correlation Between Isotropic ^{29}Si -NMR Chemical Shifts and T-O-T Angles in Zeolite Frameworks." *Nature* 308: 521–23.
- Rawal, Aditya, and BJ Smith. 2010. "Molecular Silicate and Aluminate Species in Anhydrous and Hydrated Cements." *Journal of the ...* 132(21): 7321–37.
- Rejmak, P, and JS Dolado. 2012. " ^{29}Si NMR in Cement: A Theoretical Study on Calcium Silicate Hydrates." *The Journal of Physical chemistry* 116(17): 9755–61.
- Richardson, I.G. 2004. "Tobermorite/jennite- and Tobermorite/calcium Hydroxide-Based Models for the Structure of C-S-H: Applicability to Hardened Pastes of Tricalcium Silicate, β -Dicalcium Silicate, Portland Cement, and Blends of Portland Cement with Blast-Furnace Slag, Metakaol." *Cement and Concrete Research* 34(9): 1733–77.
- . 2008. "The Calcium Silicate Hydrates." *Cement and Concrete Research* 38(2): 137–58.
- Richardson, Ian G, Adrian R Brough, Rik Brydson, Geoffrey W Groves, and Christopher M Dobsont. 1993. "Location of Aluminum in Substituted Calcium Silicate Hydrate (C-S-H) Gels as Determined by ^{29}Si and ^{27}Al NMR and EELS." *Journal of amc* 76(9): 2285–88.
- Richardson, IG. 1999. "The Nature of C-S-H in Hardened Cements." *Cement and Concrete Research* 29(8): 1131–47.
- Rodger, SA, and GW Groves. 1988. "Hydration of Tricalcium Silicate Followed by ^{29}Si NMR with Cross-polarization." *Journal of the ...* 71(2): 91–96.

- Saglik, AÜ, and ST Erdogan. 2010. "Chemical and Thermal Activation of Perlite-Containing Cementitious Mixtures." In *Proceedings of the Second International Conference on Sustainable Construction Materials and Technologies*, eds. J. Zachar, P. Claisse, T.R. Naik, and E. Ganjian. Ancona, Italy.
- Le Saoût, Gwenn, Mohsen Ben Haha, Frank Winnefeld, and Barbara Lothenbach. 2011. "Hydration Degree of Alkali-Activated Slags: A ^{29}Si NMR Study" ed. C. Jantzen. *Journal of the American Ceramic Society* 94(12): 4541–47.
- Shtepenکو, Olga, Colin Hills, Adrian Brough, and Mike Thomas. 2006. "The Effect of Carbon Dioxide on β -Dicalcium Silicate and Portland Cement." *Chemical Engineering Journal* 118(1-2): 107–18.
- Skibsted J., Jakobsen H.J., Hall C. 1994. "Direct Observation of Aluminium Guest Ions in the Silicate Phases of Cement Minerals by ^{27}Al MAS NMR Spectroscopy." *J. Chem. Soc. faraday trans.* 14: 2095–98.
- Skibsted, Jrgen, HJ Jakobsen, and Christopher Hall. 1995. "Quantification of Calcium Silicate Phases in Portland Cements by ^{29}Si MAS NMR Spectroscopy." *Journal of the Chemical Society, ...* 91(24): 4423–30.
- ŠKVÁRA, FRANTIŠEK, P Svoboda, and JOSEF DOLEŽAL. 2008. "Geopolymer Concrete-an Ancient Material Too?" *Ceramics – Silikáty* 52(4): 296–98.
- Smith, Benjamin J, Aditya Rawal, Gary P Funkhouser, Lawrence R Roberts, Vijay Gupta, Jacob N Israelachvili, and Bradley F Chmelka. 2011. "Origins of Saccharide-Dependent Hydration at Aluminate, Silicate, and Aluminosilicate Surfaces." *Proceedings of the National Academy of Sciences of the United States of America* 108(22): 8949–54.
- Sun, Guokuang, AR Brough, and JF Young. 1999. "Si NMR Study of the Hydration of Ca_3SiO_5 and $\beta\text{-Ca}_2\text{SiO}_4$ in the Presence of Silica Fume." *Journal of the American ...* 82(11): 3225–30.
- Taylor, H.F.W. 1997. *Cement Chemistry*. London: Academic Press.
- Taylor, HFW. 1986. "Proposed Structure for Calcium Silicate Hydrate Gel." *Journal of the American Ceramic Society* 67: 464–67.
- . 1993. "Nanostructure of C-S-H: Current Status." *Adv. Cem. Based Mater* 1: 38–46.
- Taylor, HFW Harry F.W. 1986. "Proposed Structure for Calcium Silicate Hydrate Gel." *Journal of American Ceramic Society* 69(6): 464–67.
- Taylor, R., I.G. Richardson, and R.M.D. Brydson. 2010. "Composition and Microstructure of 20-Year-Old Ordinary Portland Cement–ground Granulated Blast-Furnace Slag Blends Containing 0 to 100% Slag." *Cement and Concrete Research* 40(7): 971–83.

- Treacy, M M J. 2001. *Collection of Simulated XRD Powder Patterns for Zeolites*. fourth. elsvier.
- Use of Raw or Processed Natural Pozzolans in Concrete, ACI 232.1R-00*. 2000.
- Uzal, B., L. Turanlı, H. Yücel, M.C. Göncüoğlu, and a. Çulfaz. 2010. “Pozzolanic Activity of Clinoptilolite: A Comparative Study with Silica Fume, Fly Ash and a Non-Zeolitic Natural Pozzolan.” *Cement and Concrete Research* 40(3): 398–404.
- Uzal, Burak. 2007. “Properties and Hydration of Cementitious Systems Containing Low, Moderate and High Amounts of Natural Zeolites.” Middle East Technical University.
- Wenk H.-R., Bulakh A. 2005. *Minerals: Their Constitution and Origin*. Cambridge, United Kingdom: press syndicate of the university of cambridge.
- World Business Council for Sustainable Development. 2009. *The Cement Sustainability Initiative, Cement Industry Energy and CO2 Performance: “Getting the Numbers Right.”*ed. World Business Council for Sustainable Development. Washington DC.
- Xiu, Tongping, Jiacheng Wang, and Qian Liu. 2011. “Ordered Bimodal Mesoporous Boria–alumina Composite: One-Step Synthesis, Structural Characterization, Active Catalysis for Methanol Dehydration.” *Microporous and Mesoporous Materials* 143(2-3): 362–67.
- Young, J Francis. 1988. “Investigations of Calcium Silicate Hydrate Structure Using Silicon-29 Nuclear Magnetic Resonance Spectroscopy.” *Journal of the American Ceramic Society* 120(March): 118–20.
- Young, JF, and Guokuang Sun. 1999a. “Silicate Polymerization Analysis.” In *Handbook of Analytical Techniques in Concrete ...*, eds. V. S. Ramachandran and James J. Beaudoin. Park Ridge, New Jersey, U.S.A.: WILLIAM ANDREW PUBLISHING, LLC.
- . 1999b. “Silicate Polymerization Analysis.” In *Handbook of Analytical Techniques in Concrete ...*, eds. V. S. Ramachandran and James J. Beaudoin. Park Ridge, New Jersey, U.S.A.: WILLIAM ANDREW PUBLISHING, LLC.